UNIVERSITÄT PADERBORN
Die Universität der Informationsgesellschaft

Fakultät für Naturwissenschaften - Department Physik

COHERENT PROPERTIES OF SINGLE QUANTUM DOT TRANSITIONS AND SINGLE PHOTON EMISSION

Vom Department Physik der Universität Paderborn zur Erlangung des akademischen Grades eines Doktors der Naturwissenschaften genehmigte

DISSERTATION

von Dipl. Phys. PATRICK ESTER

Gutachter: Prof. Dr. ARTUR ZRENNER
Zweitgutachter: Prof. Dr. KLAUS LISCHKA

Abgabe der Dissertation: 17. März 2008
Datum der mündlichen Prüfung: 23. April 2008

Contents

1 Preface 3

2 Quantum dot basics 7
- 2.1 Quantum dot properties . . . 7
- 2.2 Growth . . . 8
- 2.3 Energy levels of self-organized quantum dots . . . 9
- 2.4 Quantum dot occupations and transitions . . . 11
- 2.5 Quantum dot spectroscopy . . . 12

3 Theoretical basics 15
- 3.1 Two level systems . . . 15
  - 3.1.1 Interaction operator . . . 15
  - 3.1.2 SCHRÖDINGER-equation . . . 16
  - 3.1.3 Solution with the *rotating-wave-approximation* . . . 17
  - 3.1.4 Density matrix . . . 17
  - 3.1.5 Optical-BLOCH-equation and BLOCH-vector . . . 18
  - 3.1.6 BLOCH-sphere . . . 19
- 3.2 Pulsed excitation . . . 20
  - 3.2.1 RABI oscillations . . . 20
  - 3.2.2 RABI-solution for the case of exact resonance . . . 21
  - 3.2.3 RABI-solution in real systems . . . 22
  - 3.2.4 RABI-solution in the case of detuning . . . 22
- 3.3 Dephasing . . . 23
- 3.4 Double pulse excitation and RAMSEY fringes . . . 25
- 3.5 Continuous Excitation . . . 27
  - 3.5.1 Saturation . . . 27
  - 3.5.2 Power broadening . . . 29

4 Experimental setup 33
- 4.1 Excitation . . . 35
  - 4.1.1 HeNe-Laser . . . 35
  - 4.1.2 Ti:Sa-Laser . . . 35
  - 4.1.3 Optical Setup . . . 37
  - 4.1.4 Power control . . . 38
  - 4.1.5 MICHELSON interferometer . . . 39
  - 4.1.6 Low temperature microscope . . . 40
- 4.2 Quantum dot photodiodes . . . 41
  - 4.2.1 Sample structure . . . 41

4.2.2 Diode design . . . 42
4.2.3 Near field shadow masks . . . 43
4.3 Detection . . . 45
4.3.1 Photocurrent technique . . . 45
4.3.2 Photoluminescence technique . . . 47
4.3.3 Photoluminescence excitation technique . . . 48
4.3.4 HANBURY-BROWN and TWISS setup . . . 48

5 Characterization of a single quantum dot 51
5.1 Optical properties . . . 51
5.2 Quantum confined STARK effect . . . 53
5.3 Photoluminescence excitation spectroscopy . . . 55

6 Single exciton ground state 57
6.1 High resolution absorption spectroscopy . . . 57
6.2 Ground state properties at continuous excitation . . . 59
6.2.1 Fine structure splitting . . . 59
6.2.2 ZEEMAN splitting . . . 60
6.2.3 Photocurrent saturation of a single quantum system . . . 62
6.2.4 Power broadening . . . 64
6.3 Coherent properties . . . 66
6.3.1 RABI-oscillations . . . 66
6.3.2 Damping of the RABI-oscillations . . . 69
6.3.3 Detuning . . . 71
6.4 Quantum interference . . . 73
6.4.1 Double $\pi/2$ pulse excitation . . . 73
6.4.2 RAMSEY fringes . . . 77

7 First excited state 81
7.1 Voltage dependent photoluminescence for p-shell excitation . . . 81
7.2 Excitation polarization dependence of the p-shell . . . 83
7.3 p-shell saturation . . . 85
7.4 p-shell RABI-flopping . . . 86
7.5 Dephasing of the p-state polarization . . . 88

8 LO-phonon assisted absorption 91
8.1 Voltage depending photoluminescence . . . 92
8.2 Polarization analysis of the LO-phonon absorption . . . 93
8.3 Saturation of the LO-phonon assisted transition . . . 93
8.4 Pulsed excitation . . . 95
8.5 Dephasing of the LO-phonon assisted transition . . . 96

9 Biexciton generation 101
9.1 Photoluminescence excitation of the biexciton . . . 101
9.2 s-shell luminescence for biexciton excitation in the p-shell . . . 102

10 Single photon emission 105
10.1 First and second order correlation function 105
10.2 Correlation functions of laser, classic light, and quantum-mechanical light 106
10.3 Correlation function of a single photon emitter 107
10.4 Sequential absorption-emission events within one excitation pulse 109
10.5 Continuous non-resonant interband excitation 110
10.6 Single photon emission after coherent (p-)state preparation 112
10.7 Single photon emission after GaAs LO-phonon assisted absorption 113
10.8 Single photon emission devices 114

11 Conclusion and outlook 117

Symbols and abbreviations 119

Bibliography 123

List of publications 129

Danksagung 131

Abstract

After the discovery of the self organized generation of quantum dots (QDs), a new field in the area of semiconductor physics was initiated. Physicists worldwide have been inspired by the new possibilities which arise due to this discovery. The creation of self assembled QDs takes place almost defect free. Thus, these quantum dots exhibit a very high optical quality. Due to an over-growth with a higher band gap semiconductor, a confinement potential for excitons can be created. The energy levels of a confined exciton are quantized, and therefore similar to an atom. However, this quantum system is fixed in space. Hence, it is fairly easily possible to study the properties of a single quantum system.

In this work, the properties and the different dephasing mechanisms of single QD transitions are analyzed. In addition, some applications are presented which arise due to the properties of the confined exciton. The isolation of a single QD out of the ensemble is achieved via near field shadow masks, which restricts excitation and QD luminescence to a single QD. The integration of a QD-layer into a diode structure allows for an analysis of various dephasing mechanisms of a confined electron hole pair. The single QD is characterized regarding the energy of nearly all possible transitions, e.g. the ground state, excited states, charged states, multiple occupations, and phonon assisted absorptions. A very important issue in this content is the voltage dependence of the transition energy and thereby the ability of tunneling processes of charge carriers in and out of the QD.

The QD-states, which are subject of investigation here, are the single exciton ground state, the first excited state (p-shell), and the (GaAs-) LO (longitudinal optical) phonon assisted absorption. By applying a suitable voltage, the resonantly excited ground state exciton is able to decay by a tunneling process, which reflects the transition energy in the photocurrent spectra. The p-shell transition decays by a relaxation process into the ground state, followed by an optical recombination process. The phonon assisted absorption differs from the p-shell transition. The resonant excitation energy fits to the exciton ground state energy plus the energy of a GaAs LO phonon. In this case, the single exciton (ground state) is generated as well as a GaAs LO phonon.

These three states are investigated in different respects, such as different applied voltages, excitation polarizations, excitation intensities, and coherent properties. It is only possible to treat a QD state as a quantum mechanical two level system if it exhibits specific coherent and incoherent characteristics, such as occupation saturation (with increasing excitation intensity). In particular, a coherent excitation must be possible. This is demonstrated for the single exciton ground state by photocurrent experiments and for the p-shell transition by photoluminescence experiments. The LO-assisted absorption shows also a saturation behavior, but here coherent state preparation seems not possible with the available excitation conditions. The comparably long dephasing time of the single exciton ground state easily allows for two time separated interactions of laser pulses

with the QD. The exciton in the QD is able to interfere with the second laser pulse due to the storage of the phase information of the first laser pulse. The relative phase of the QDs exciton can be controlled externally via the bias voltage. This effect is the basis for the observation of RAMSEY-fringes, which are presented in this work.

The coherent manipulation of the *p*-shell is the basis for a novel excitation scheme for single photon emission. In this work it is shown that the first excited state can be coherently manipulated, similar to the ground state. Due to this defined excitation of a single exciton in the *p*-shell, the resulting single photon emission (after the relaxation and recombination process) appears remarkably clean, as demonstrated by HANBURY-BROWN and TWISS experiments.

1 Preface

The continuous advancement in the field of semiconductor technology leads to more and more powerful and smaller devices. The progress in reducing the structure sizes has been frequently predicted an end. A physical end of the classic design of semiconductor devices is nowadays predicted due to quantum effects in strongly reduced structure sizes. The quantum properties of low dimensional semiconductor structures are thereby the basis for future semiconductor technologies.

The current (computer-) technology is based exclusively on classical physics, where all currents can be regarded as a continuous charge distribution. The fact that single charge carriers exhibit wave properties and are furthermore able to perform tunneling processes through small potential barriers is widely neglected. With further reduction of the structure sizes, these quantum effects are becoming more and more important. For the classic design of semiconductor structures, these quantum effects are usually seen as a handicap [Lun03]. The challenge for future developments is a combination of the quantum effects and the classic design.

The reduction of the structure sizes in one or more dimensions leads to a quantization of the exciton states. Every degree of a confinement has its own physics and properties. A confinement in one dimension is called a quantum well, in two dimensions, quantum wire. A confinement in all three directions of space is called a quantum dot (QD). The technical realization of these low dimensional systems takes place by structuring-methods like photo- or electron-beam lithography or by modern epitaxy methods like molecular beam epitaxy (MBE). The samples used in this work are grown by MBE, which allow a precise and controlled deposition of semiconductor materials on a substrate with an atomic resolution in growth direction. A deposition of a semiconductor material on a semiconductor substrate (different lattice constants) generates strain energy in the coherently strained wetting layer. At a critical layer thickness, the strain is removed by the formation of coherently strained islands. Due to the island overgrowth, the confinement of the QD arises. The generation of these QDs takes place almost defect free, which is very important for optical applications. The QDs samples can be annealed in order to shift their transition energy via diffusion processes.

There are various improvements in device-properties possible, comparing low dimensional systems to a bulk semiconductor device. Due to reduction of the dimensions, the overlap of electron- and hole-wave function is strongly enhanced, which is a big advantage for optical applications. In the case of one dimensional confinement, the quantum well structures developed fast to home-used devices. Today, quantum well lasers can be found in units like CD-players or laser printers. Furthermore low dimensional systems are very interesting for fundamental research. The quantization in all three directions of space leads to discrete energy levels, similar to an atom. Hence it is possible to investigate the properties of an atomic-like single quantum system.

These properties are analyzed by means of a coupling or an interaction of the QD with light, free charge carriers, phonons, electric and magnetic fields, etc. The achievements of the research in this field are versatile. A QD can be integrated in a diode structure to analyze tunnel effects, the STARK-effect, and occupation properties. Furthermore they can be used for optoelectronic devices such as single photon emitters, which is viable for quantum cryptography. Furthermore, it has been tried to build lasers with QDs [KLG+94, PY99, LLU+00]. Another interesting feature in the field of QD-devices is the possibility of a coherent state manipulation. Here, the energy quantization is as important as the phase of the quantum system. QDs also provide the possibility of an implementation in quantum gate devices. The utilization of the coherent properties of such low dimensional systems for quantum information technology is of course subject of intensive investigation.

A very interesting item in the field of quantum information processing is quantum cryptography. With this technique, a completely safe transfer of information can be guaranteed. The problem of safe communication is reduced to a safe transfer of the encoding key. In this case, the data communication is done via single photons, where the information is stored in the polarization. The main point here is that it is not possible to exactly copy single quantum states, which is expressed in the *no-cloning-theorem*. An eavesdropping attack can thereby be identified by strongly enhanced error rates. Meanwhile commercial devices for quantum cryptography are available. Usually the single photons for the information transfer are generated by an attenuated laser. The data transmission could be improved by using quantum emitters, which are principally not able to emit two photons at the same time. One proposal for such a single photon emitter is presented in this work.

Another very interesting issue in this context is quantum computation, which is based on quantum mechanical effects like entanglement and superposition. For a wide class of problems, the efficiency in solving problems can be significantly improved compared to classical information technology. For classic data information processing, a bit can take two values: zero and one. In the case of a quantum mechanical two level system, a quantum bit (qubit) can take both states in a coherent superposition. These qubits are the basic building blocks of a quantum computer. There is an advantage for the quantum algorithms compared to the classical computation algorithm due to the parallel processing of the coherent state superposition. The theoretical concept is quite promising, but the technical realization of a quantum computer is extremely complex and challenging. First success was reported in the year 2001, when the SHOR-algorithm was demonstrated in a nuclear magnetic resonance based quantum system with seven qubits [VSB+01]. An expansion of this approximation up to hundred or thousand qubits appears to be hardly possible. A very good overview about the quantum information processing can be found in [ABH+01] and [BEZ00].

In this thesis the properties of a single quantum dot are analyzed, regarding the single exciton ground state transition, the *p*-shell transition, and the LO-assisted absorption. The different quantum dot states exhibit different dephasing mechanisms and time scales, whereby only the ground state dephasing can be effected by an external parameter. In the case of controllable dephasing, the QD system can be used as a very sensitive sensor. Here one would like to have a very long dephasing time. The dephasing of the

excited state is mainly determined by the relaxation process into the ground state. This process cannot be controlled by an external parameter. However, for an application such as a single photon emitter, a fast relaxation process after excitation is preferable.

This work is divided into the following chapters:

Chapter *two* introduces the self organized STRANSKI-KRASTANOW quantum dots. The basic properties of these quantum dots are discussed, regarding growth methods, ensemble measurements, and single dot isolation.

Chapter *three* explains the theoretical concept of a quantum mechanical two-level system, including the interaction operator, the SCHRÖDINGER equation, the density matrix, and the optical BLOCH equations. Afterwards, the coherent and incoherent properties, and the dephasing time constants are discussed. Furthermore, the theoretical basis for the RAMSEY-fringes is presented.

Chapter *four* discusses the experimental realization. At the beginning, the excitation setup is presented. The sample design is a very important item for the photocurrent spectroscopy. After the sample design, the two different detection techniques for photocurrent, photoluminescence, and photon correlations are discussed.

Chapter *five* shows the sample characterization. The spectral position of the ground state and the excited states are analyzed. The state identification is done by voltage dependent photocurrent and photoluminescence experiments.

Chapter *six* is dealing with the single exciton ground state. The advantage of the absorption technique is discussed, followed by the analysis of fine structure splitting of the ground state. This fine structure splitting is analyzed by polarization dependent excitation and magnetic field measurements. Then the incoherent experiments of power broadening and saturation are shown. Afterwards, coherent measurements like RABI-oscillations, dephasing, and RAMSEY-fringes are discussed.

Chapter *seven* describes the properties of the first excited state. After the resonant excitation process of the *p*-shell, the exciton relaxes into the ground state and subsequently decays by optical recombination. The *p*-shell transition is analyzed regarding the incoherent and coherent properties. Finally, the dephasing of the *p*-shell transition is shown by double pulse experiments.

Chapter *eight* is similar to chapter *seven*, but here the behavior of the LO-phonon assisted absorption state is discussed and compared to the normal *p*-state transition. With the excitation of LO-phonon assisted absorption it is also possible to generate the biexciton state. This is shown in a photoluminescence excitation experiment in chapter *nine*.

Chapter *ten* shows how the coherent manipulation of the *p*-state can be used for a very clean single photon emission. Furthermore the LO-assisted absorptions can also be used for single photon emission. Both excitation schemes are analyzed in a HANBURY-BROWN and TWISS experiment.

Chapter *eleven* gives a summarize of this thesis.

2 Quantum dot basics

Not only a single atom can have quantum properties, also a cluster of many more than one atom ($> 10^4$ atoms) is able to show quantum effects. Due to the semiconductor band diagram, it is possible to design a confinement potential for charge carriers with two different materials. Thereby the complete field of quantum physics in semiconductors develops. Semiconductor structures, which provide a three dimensional confinement, are called quantum dots (QDs). The one dimensional confinement is called quantum well, and a confinement in two dimensions is called quantum wire. In order to define the kind of confinement, two different (semiconductor-) materials must be combined, which exhibit different band gaps.

2.1 Quantum dot properties

Every three dimensional confinement potential for charge carriers, which is small enough to exhibit quantum effects, can be called quantum dot. One kind of QD is a two dimensional electron gas with suitable gate structures (e.g. see reference [HvBV$^+$05]). Another kind of QD is a fluctuation in a quantum well structure. Here the excitons are located in regions of the quantum well, which are coincidentally thicker than their environment. This leads to QDs with a relatively large lateral expansion and weak confinement potential. The weak confinement potential leads to a large exciton diameter and a low overlap of the wave functions. Therefore, excitons with a low diameter are more suitable for optical applications. But the most common system is based on self organized semiconductor QDs. Figure 2.1 c) shows AFM picture of a layer of self organized QDs. These QDs exhibit a very high optical quality, whereby a spectroscopic analysis becomes possible. Figure 2.1 a) shows a schematic sketch of the lateral confinement of an exciton in such a QD. These semiconductors QDs could be easily integrated into a diode structure and therefore it is possible to build a device. A defined positioning of a single QD would be a great step for fundamental physics and for all possible applications. Of course this is subject of intensive research. First successes were achieved by the groups of REUTER and SCHMIDT (reference [MRM$^+$07] and [KRS05]). They recently processed areas on the substrate where the QD arrangement is controlled. The next step for the single QD spectroscopy is the integration of these QDs into a diode structure where the active region is reduced to a single QD. The single dot spectroscopy in this work uses samples where QD isolation is done via shadow masks.

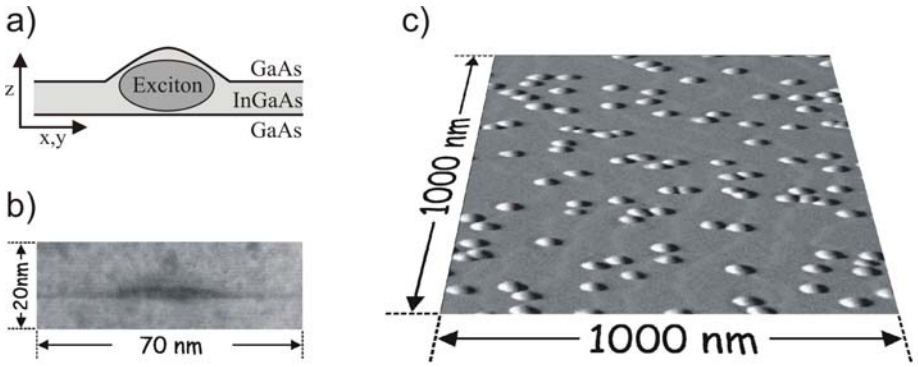

Figure 2.1: Quantum dot sample: a) schematical illustration of an confined exciton in a QD b) TEM-picture c) AFM-surface picture with quantum dots

2.2 Growth

For the fabrication of self organized semiconductor QDs, materials with different lattice constants are needed. The island material must have a larger lattice constant than the substrate material. For a three dimensional confinement for charge carriers, the island material should have a smaller band gap than the substrate material. The most common material system for self organized QD growth is InAs and/or InGaAs.

A key technique for the epitaxial growth of semiconductor QDs is the molecular beam epitaxy (MBE). The self organized island formation takes place in the STRANSKI-KRASTANOW growth mode, which can be characterized in the following way: During the deposition of (for example) InAs on GaAs, the growth starts in two dimensions (wetting layer). Thereby the strain energy increases during the deposition of InAs. With this kind of growth, the epitaxially deposited material has the lateral lattice constant of the substrate. With MBE, it is possible to add material in growth direction with an atomic resolution. Further deposition generates more strain energy in the coherently strained wetting layer. At a critical layer thickness, the transition from layer growth to three-dimensional island growth takes place. At this layer thickness, the strain is removed by the formation of coherently strained InAs islands, as shown in figure 2.1 c). An increase of the surface energy is connected to the island formation. The total energy of the system remains smaller due to the strongly reduced strain energy in the islands, compared to a further two-dimensional growth, see reference [SK]. The island formation results in an almost defect-free island growth and a high optical quality of the QDs (see reference [EC90]). Due to the island overgrowth, the confinement of the QD arises, as illustrated in figure 2.1 a). The smaller energy gap of InAs compared to the GaAs substrate generates a trap for free charge carriers. Due to the (small) size of the QD, the energy levels of a trapped charge carrier are quantized.

After the growth process, it is possible to tune the QD transition energy by thermal annealing. Due to the thermal energy, Ga atoms from the substrate are able to diffuse into the QD and replace In atoms. After a while, the QD consists of an enlarged $In_{(1-x)}Ga_xAs$ island in a GaAs environment. After this diffusion process, the transition energy of a con-

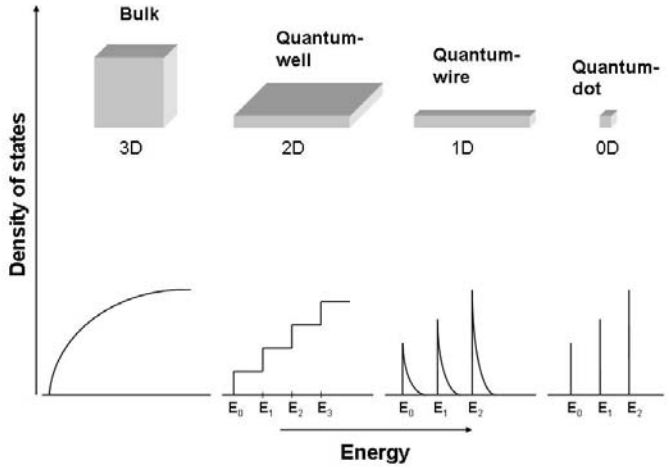

Figure 2.2: Comparison of the density of states of a bulk semiconductor and low dimensional systems. Due to the decrease of the dimensions, the density of states changes to an atomic-like behavior for a three dimensional confinement.

fined exciton is determined by the ratio of In to Ga in the QD and the geometry (shape and size) of the QD. It is also possible to grow InGaAs QD directly with the MBE-equipment, but the thermally induced diffusion allows post growth tuning the transition energy to the desired spectral range.

2.3 Energy levels of self-organized quantum dots

Figure 2.2 shows the change of the density of states from the bulk semiconductor to the QD. Due to the reduction in the degree of freedom, the density of states results in δ-functions (similar to an atom) for a zero dimensional system (QD). In the bulk GaAs semiconductor, the electron hole interaction leads to the formation of the exciton and to the renormalization energy of about 4.2 meV compared to the band gap energy. The three-dimensional confinement of electron and hole in a QD leads to a decrease of the exciton diameter as compared to the three dimensional case. The exciton binding energy is increased compared to the bulk semiconductor. For example, excitons in InGaAs/GaAs QDs exhibit a characteristic COULOMB energy of approximately 25 meV, as reported by WOJS et al. [WHFJ96]. For the computation of the energy levels of a QD, which is occupied with several charge carriers, many particle interactions must be considered. The influence of many particle effects on the energy levels of a QD results in different renormalization energies for different charge configurations. In the examined sample, the renormalization energy for a simply negatively charged exciton X^- amounts to 5 meV, and the biexciton binding energy amounts here to 2.7 meV.

An important fundamental characteristic of the semiconductors GaAs and InAs is that the conduction band minimum as well as the valence band maximum are located in the Γ- point of the BRILLOUIN zone. That means that both material systems are direct semiconductors. In an atom, the parity of wave functions of the staring state and the ending state must be different for an optical transition. Here the envelope functions of the conduction band and the valence band have the same parity. Due to the BLOCH function, the optical transition is allowed for the lowest energy levels. The conduction band is *s*-shaped, and the valence band behaves *p*-shaped. Exactly this feature makes the In(Ga)As QDs very interesting for opto-electronics.

For an accurate quantum-mechanical simulation of the electronic structure of a QD, its geometry and potential must be known. The microscopic characteristics of an individual QD can only be determined experimentally. That's why an accurate calculation of the energy levels of a specific QD is almost impossible. Experimentally, the QD ground state energy level can be determined fairly easy by using photoluminescence (PL) spectroscopy (see chapter 4.3.2). For the description of the QDs energy levels, one starts with a separation of electron and hole, and simulate single particle states. The optical selection rules result in allowed optical transitions (observed in the experiment). The transition energy will be corrected afterwards, considering the COULOMB-interaction. The single particle states for electrons and holes in a QD can be simulated with different potentials and QD-geometries. Many of the models lead to complicated energy spectra. Examples for models are cylinder, cone [VFSB01], ball [OAM99] or lens shaped [WHFJ96] quantum boxes of constant potential [DGE+98] up to pyramids with certain crystal faces, considering the piezo-potentials [SGB99], arising due to the strain.

A fairly simple assumption provides very useful results. The basis of this model is a two dimensional harmonic oscillator. Detailed computations show that the parabolic lateral confinement leads to a QD energy scheme similar to a lens-shaped QD. Therefore this model is a very good approximation [WHFJ96]. In this model, the confinement of the charge carriers in growth direction can be neglected. The QD can be regarded as a quasi-two-dimensional system. The strong quantum-mechanical confinement in growth direction permits the negligence of excited QD levels in this direction. Contrary to the conduction band, the valence band is degenerated due to its *p*-character. This results in heavy and light holes. But only the heavy holes are relevant for the lowest energy levels of a QD. Due to the restriction to two dimensions, all QD levels consist of a combination of the vertical initial level and the lateral EIGEN-states of the harmonic oscillator. For the description of the lateral confinement, a radial symmetric parabolic potential $V = 1/2 m^*_{e/h} \omega^2_{e/h} r^2_{e/h}$ [JHW98] is used. The effective masses are labeled with $m^*_{e/h}$, and the lateral positions with $r^2_{e/h}$ for electron (e) and hole (h). The parameter $\omega^2_{e/h}$ describes the strength of the confinement for electron and hole. The energy levels for electrons and holes correspond to the two-dimensional harmonic oscillator with the two quantum numbers n and m. The energy EIGEN-values of electron and hole are given by $E_{n,m} = \hbar\omega_{e/h}(n + m + 1)$. The two quantum numbers are used for the index of the energy levels, whereby, in analogy to the assignment of the electron shells in atomic physics, the assignment $l = s, p, d, ...$ for $m - n = 0, 1, ...$ is introduced. The combined main quantum number N results from the sum of the quantum numbers ($N = n + m$) and defines

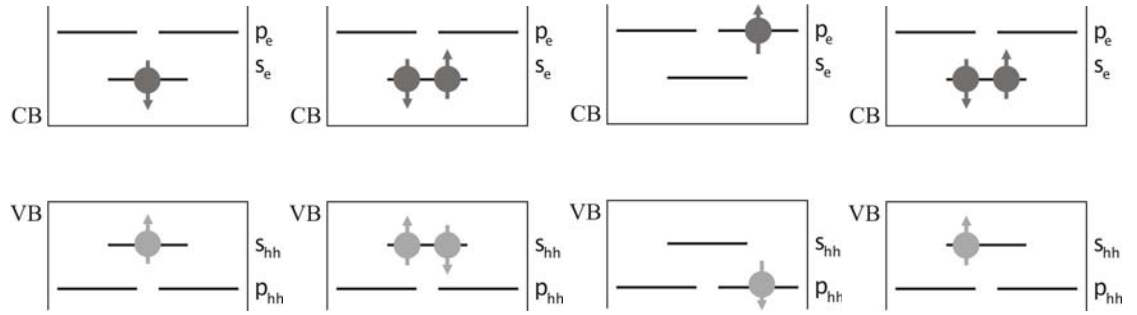

(a) Exciton (X) (b) Biexciton ($2X$) (c) Exciton in the p-shell (X_p) (d) Single charged exciton (X^-)

Figure 2.3: Schematic illustration of different QD occupations

the degeneracy of the energy levels to $2(N+1)$. The factor 2 results from the spin degeneracy. The energy levels $E_{n,m}$ are equidistant for electrons and holes, separated by $\hbar\omega_e$ and $\hbar\omega_h$. Deviations from the cylinder symmetry would lead to different behavior. With an asymmetric potential, for example, optical transitions between levels with different quantum numbers can occur or the degeneracy of the energy levels can be partly removed, as reported by TSIPER et. al. in [TWM+97].

2.4 Quantum dot occupations and transitions

In QD optics, the most basic occupancy is an uncharged exciton. This is illustrated in figure 2.3 a) by an electron in the conduction band and a hole in the valence band (X). With the confinement of a further charge carrier in the QD, the exciton is singly charged (X^-), as shown in Figure 2.3 d). Due to the interaction of the additional electron with the existing electron-hole pair, the transition energy shifts. The second electron can take the second s-state in the QD, with opposite spin. For a further occupation of the QD, the exciton is either more highly charged (X^{-2},X^{-3},...) or developed to a multi-excitonic state ($2X$,$3X$,...). Figure 2.3 b) shows the QD occupation of the QD with two electrons and two holes. This is called a biexciton $2X$.

In(Ga)As-QDs are attributed to the so-called Type I QDs, which represent a potential minimum for electrons *and* holes. Therefore electrons and holes can be described in the single particle picture. The well-known selection rule $\Delta l = \pm 1$ for optical transitions is already fulfilled for $s_e \rightarrow s_{hh}$ because of the s-character of the BLOCH-waves in the conduction band and the p-character of the valence band. Interband transitions are therefore only allowed between QD levels having the same angular momentum, which results in the selection rule of $\Delta m = \Delta n = 0$. In addition, the spin must also be considered by all these transitions. Regarding only the lowest level of a QD, the two possible spin settings are for the electron $S_z = \pm 1/2$ and for the heavy hole $J_z = \pm 3/2$. J designates the total angular momentum, which results from the coupling of spin and angular momentum. Altogether one receives the four transitions explained in figure 2.4. An electron in the valence band has a spin of $\pm 3/2$. An excitation of the electron into the conduction band leads to the spin value of $\pm 1/2$. The residual hole in the valence band has the opposite

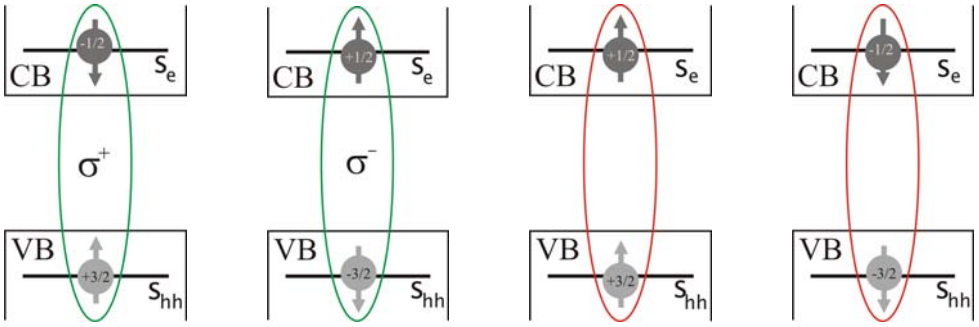

(a) m=+1; allowed (b) m=-1; allowed (c) m=+2; forbidden (d) m=-2; forbidden

Figure 2.4: Spin-adjustments of possible QD excitations of the lowest level of a single QD. Only a) and b) (green) are optically allowed. In high magnetic fields, the forbidden states (red) can become allowed.

spin $\mp 3/2$ (of the electron). The combined spin of an electron and a hole $\pm 3/2 \rightarrow \mp 1/2$ results in a total spin of ± 1, which can be carried by a $\sigma^{\pm}$ circular polarized photon, see figure 2.4. The states of $\pm 3/2$ and $\pm 1/2$ result in a total spin of ± 2 and thereby no optically transitions are allowed. Therefore these levels are also called *dark* excitons.

A QD can be resonantly excited as well as non-resonantly. When the QD is non-resonantly excited (interband), the generated excitons can be confined in the QD after relaxation process into the lowest unoccupied level. An empty QD can (resonantly) absorb a photon of the energy E_{1X} and produce an exciton as shown in figure 2.3 a). An optical transitions can then take place by a recombination process with the energy E_{1X}. If the QD is already occupied with an exciton, the QD can not absorb a further photon of the energy E_{1X}, however one of the energy $E_{2X} - E_{1X}$ and thus generate the biexciton ($2X$) state, see figure 2.3 b). The biexciton state can decay into a photon and a single exciton, which subsequently decays into a photon with the energy E_{1X}. The electrons and the holes of the biexciton exhibit opposite spin. A nonlinear two photon absorption process can also produce a biexciton. The two absorbed photons (complementary circular polarized) each having the energy of $(E_{1X} + E_{2X})/2$ (see [SME+06]). With high (interband) excitation intensity, the generation of a third exciton ($3X$) is possible. Two excitons occupy the s state, and the third exciton is in the p-state. In the case of a resonant excitation, it is possible to directly excite an exciton in the p-shell. This is illustrated in figure 2.3 c). This state will relax into the ground state, typically on a ps time scale.

2.5 Quantum dot spectroscopy

A commonly used method for characterizing semiconductors and semiconductor QDs is photoluminescence (PL) spectroscopy. This technique provides access to the optical quality and electronic characteristics of the QDs. Due to the discrete energy structure of single QDs, discrete optical transition energies are expected. By measuring the PL, it turns out that the sharp spectral characteristics of discrete transitions are only visible in the single QD limit. Due to self organization of the growth, every QD has an individual size and

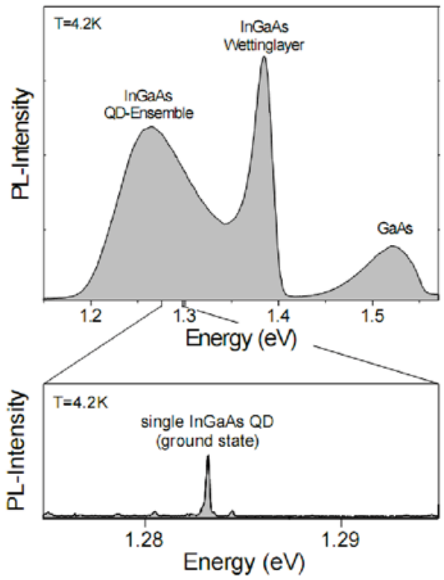

Figure 2.5: Comparing the luminescence of a QD ensemble and a single QD (from [Beh03]). Due to the statistic fluctuations of the self organized growth the ensemble luminescence is inhomogeneous broadened. The discrete spectra is only visible by view on a single QD.

therefore an individual transition energy. The distribution of shape and size follows a statistic process. On a QD ensemble measurement, every QD contributes with its own EIGEN-energies. This results in an inhomogeneous broadening of the optical transition energies. Therefore always relatively broad spectral lines are observed for QD ensembles. The spectral width of the PL-signal can be used as a measure of the homogeneity of the manufactured QDs. Typically, the FWHM (full width half maximum) of a InGaAs QD ensemble is approximately 100 meV, which is relatively large as compared to InAs QDs with typically 20-50 meV. Since the size of the QD is directly connected to the transition energy of the exciton, the spectral position of the radiative recombination will vary from QD to QD. Therefore each sample will be characterized using PL spectroscopy. The emission signal will not exhibit discrete spectra, due to the statistic fluctuation of the exciton energy. This is only the case after the isolation of an individual QD. Figure 2.5 shows the difference in the spectrum between a single QD and an ensemble of QDs. The isolation of an individual QD is achieved by an aluminum shadow mask with holes having a size of some 100 nm diameter, see chapter 4.2.1. Ideally only one individual QD should be located under a single hole. Therefore the QD density must be sufficiently low. It is possible to investigate an individual QD, when excitation and detection are limited to a single hole. The luminescence of an excited state of a single QD cannot directly be detected due to the fast relaxation process into the ground state. For example, the direct luminescence of the p-shell could only be observed, if the QD is occupied with a $3X$. The higher energy levels of a single exciton can be analyzed using the photoluminescence excitation spectroscopy, discussed in chapter 4.3.3.

3 Theoretical basics

3.1 Two level systems

Two level systems represent simple but nontrivial quantum mechanical systems. They are the basis of theoretic and experimental research. The interaction between light and the two level systems is treated in numerous textbooks, e.g. see reference [AE75]. This chapter gives an overview of the relevant results of the theoretical description of a two level system. It is irrelevant which material system is taken into account, e.g. an exciton in a QD, single atomic transitions, single spins,... It is not important (in a first approximation) weather the system consists in fact of more than two levels. Important is the limitation of the excitation to a single quantum transition. This is the case if the transition is resonantly excited and the next transition is clearly separated.

In this work, the two level system is represented by the transition from the empty QD to (i) a single exciton in ground state, (ii) the first excited state and (iii) the LO-phonon assisted absorption. It is also possible to describe the transition from the empty QD to the biexciton state $2X$ as a two level system, which is shown in reference [SME+06].

3.1.1 Interaction operator

The basis for the interaction of an incident laser is the existence or the change of an electrical dipole moment. Due to the fixed position of the QD, the dependence of an electrical field from the space coordinate could be neglected.

$$E(\vec{r}, t) = \vec{E}(t) \tag{3.1}$$

This approximation is called *optical dipole approximation*. The oscillating electrical field of the laser radiation at the QD is described as:

$$\vec{E}(t) = \vec{\epsilon} E_0 \cos(\omega_L t) \tag{3.2}$$

The interaction operator can therefore be written as:

$$V = -\vec{d} \cdot \vec{E}(t) \tag{3.3}$$

with the electrical dipole operator $\vec{d} = -e\vec{r}$. The polarization vector corresponds to $\vec{\epsilon}$ and ω_L to the frequency. E_0 is the electrical field amplitude.

3.1.2 SCHRÖDINGER-equation

The aim of this section is the prediction of the time evolution of a two level system under the influence of light. The time evolution of a state is described by the time dependent SCHRÖDINGER-equation:

$$\mathrm{i}\hbar\frac{\partial}{\partial \mathrm{t}}\psi(r,t) = H\psi(r,t) = (H_{QD} + V)\psi(r,t) \tag{3.4}$$

The basis for the description of the interaction between light and the QD is the HAMILTON-operator. The HAMILTON-operator is composed of the HAMILTON operator of the undisturbed state H_{QD} and the interaction part V. The approximation for the wave function is generally:

$$\psi(r,t) = c_1(t)\mathrm{e}^{-\mathrm{i}\omega_1 t}u_1(\vec{r}) + c_2(t)\mathrm{e}^{-\mathrm{i}\omega_2 t}u_2(\vec{r}) \tag{3.5}$$

$$\psi(r,t) = c_1(t)\,|1\rangle + c_2(t)\,|2\rangle \tag{3.6}$$

Here $c_1(t)$ and $c_2(t)$ correspond to the time dependent amplitudes of the two stationary EIGEN-functions $u_1(\vec{r})$ and $u_2(\vec{r})$. If formula 3.6 is used in formula 3.4, this result in:

$$\frac{\partial}{\partial t}\psi = \dot{c}_1(t)\,|1\rangle + \dot{c}_2(t)\,|2\rangle + c_1(t)(-i\omega_1)\,|1\rangle + c_2(t)(-i\omega_2)\,|2\rangle \tag{3.7a}$$

$$H_{QD}\psi = c_1E_1\,|1\rangle + c_2E_2\,|2\rangle \tag{3.7b}$$

$$V\psi = -\vec{d}\vec{\varepsilon}E_0\cos(\omega_L t)(c_1\,|1\rangle + c_2\,|2\rangle) \tag{3.7c}$$

The three equations 3.7 are added in 3.4 and multiplied scalar with $\langle 2|$ (and afterward with $\langle 1|$) from the left.

$$\mathrm{i}\hbar\dot{c}_2 + c_2\underbrace{\hbar\omega_2}_{=E_2} = c_2E_2 - E_0\cos(\omega_L t)c_1 < 2|\vec{d}|1 > \vec{\varepsilon}$$

with: $\langle 1|2\rangle = \langle 2|1\rangle = 0$ and $\langle 1|1\rangle = \langle 2|2\rangle = 1$. This results in two differential equations for the time dependent coefficients:

$$\dot{c}_1 = \frac{\mathrm{i}}{\hbar}d_{21}^{\varepsilon}E_0\mathrm{e}^{-\mathrm{i}\omega_{21}t}\cos(\omega_L t)c_2 \tag{3.8a}$$

$$\dot{c}_2 = \frac{\mathrm{i}}{\hbar}d_{21}^{\varepsilon}E_0\mathrm{e}^{\mathrm{i}\omega_{21}t}\cos(\omega_L t)c_1 \tag{3.8b}$$

where $d_{21}^{\varepsilon}\mathrm{e}^{-\mathrm{i}\omega_{21}t} = \langle 2|\vec{d}|1\rangle\vec{\epsilon}$ is the projection of the dipole matrix element on the polarization vector. The dipole matrix element indicates the coupling strength of the transition. If the dipole matrix element vanishes, the transition is forbidden. The differential equations describe the time evolution in the ideal case.

3.1.3 Solution with the *rotating-wave-approximation*

In the following, the dipole matrix d_{21}^{ε} is written as d ($d = d_{21}^{\varepsilon}$), and the RABI-frequency is introduced.

$$\Omega_0 = \frac{dE_0}{\hbar} \tag{3.9}$$

Equation 3.8 is rewritten with the EULER-formula to:

$$\dot{c}_1(t) = \mathrm{i}\frac{\Omega_0}{2}(\mathrm{e}^{\mathrm{i}(\omega_L-\omega_{21})t} + \underbrace{\mathrm{e}^{-\mathrm{i}(\omega_L+\omega_{21})t}}_{\to 0})c_2(t) \tag{3.10a}$$

$$\dot{c}_2(t) = \mathrm{i}\frac{\Omega_0}{2}(\mathrm{e}^{-\mathrm{i}(\omega_L-\omega_{21})t} + \underbrace{\mathrm{e}^{\mathrm{i}(\omega_L+\omega_{21})t}}_{\to 0})c_1(t) \tag{3.10b}$$

Within the approximation of a near resonant light-QD coupling the relation $\omega_{21} \approx \omega_L$ becomes valid. The terms with $\omega_{21} + \omega_L$ oscillate very quickly and do not contribute to the coupling of the two level system. Therefore they are neglected in the following. This approximation is called **rotating-wave-approximation**. The detuning of the laser energy with respect to the transition is defined as:

$$\delta = \omega_L - \omega_{21} \tag{3.11}$$

Therefore, equation 3.10 can be written as:

$$\dot{c}_1(t) = \mathrm{i}\frac{\Omega_0}{2}\mathrm{e}^{\mathrm{i}\delta t}c_2(t) \tag{3.12a}$$

$$\dot{c}_2(t) = \mathrm{i}\frac{\Omega_0}{2}\mathrm{e}^{-\mathrm{i}\delta t}c_1(t) \tag{3.12b}$$

The time dependent constants directly correspond to the occupation of the system. The solution of the time evolution is shown later in this chapter.

3.1.4 Density matrix

Up to now, the effects of finite lifetime on the time evolution of a two level system have not been included. The decay of the excited state into the ground state under the emission of a photon is called spontaneous emission. Such spontaneous emission processes cannot correctly be described by the SCHROEDINGER equation, because this equation can only characterize *pure* states. But it is experimentally not guaranteed that only pure states are prepared, and no emission processes lead to a superposition of two states. Therefore the density matrix is very important. It is possible to describe coherent as well as incoherent superposition of states with the density matrix. The density matrix is defined:

$$\rho = \begin{pmatrix} \rho_{11} & \rho_{12} \\ \rho_{21} & \rho_{22} \end{pmatrix} = \begin{pmatrix} c_1c_1^* & c_1c_2^* \\ c_2c_1^* & c_2c_2^* \end{pmatrix} \tag{3.13}$$

The non diagonal elements are called the *coherences* of the system. They only result for coherent state superpositions. If the system is, with the statistical probability p_k, in the quantum state ψ_k, then the density operator is

$$\hat{\rho} = \sum p_k \left|\psi_k\right\rangle \left\langle\psi_k\right| \tag{3.14}$$

The corresponding density matrix elements ρ_{ij} are:

$$\rho_{ij} = \left\langle i\right| \hat{\rho} \left|j\right\rangle \tag{3.15}$$

The matrix elements ρ_{11} and ρ_{22} describe the occupation of the states. That means they give directly the probability to find the system in the state $|1\rangle$ or $|2\rangle$. The matrix elements ρ_{12} and ρ_{21} correspond to the coherence. If they vanish, the phase between $|1\rangle$ and $|2\rangle$ is totally undefined.

3.1.5 Optical-BLOCH-equation and BLOCH-vector

Important is the time evolution of the density matrix. It is obvious that a two-level system must be in the second state if it is not in the first state. Therefore it is possible to show:

$$\frac{d}{dt}\rho_{11} = -\frac{d}{dt}\rho_{22} \Rightarrow \rho_{11} + \rho_{22} = \text{constant} = 1 \tag{3.16}$$

and

$$\rho_{12} = \rho_{21}^{*} \tag{3.17}$$

Therefore the four components of the density matrix are no longer independent. One can now define the components of the BLOCH-vector as:

$$u = 2\mathrm{Re}(\rho_{12}\mathrm{e}^{-\mathrm{i}\delta t}) \tag{3.18a}$$

$$v = 2\mathrm{Im}(\rho_{12}\mathrm{e}^{-\mathrm{i}\delta t}) \tag{3.18b}$$

$$w = \rho_{22} - \rho_{11} \tag{3.18c}$$

u is the dispersive component of the BLOCH-vector, v is the absorptive component of the BLOCH-vector and w corresponds to the *inversion*. w directly describes the occupation of the system because $\rho_{22} - \rho_{11}$ is the probability of the energetic higher state minus the probability of the energetic lower state. The equations 3.18 are called *optical*-BLOCH-*equations* (OBE), which were developed from FELIX BLOCH (Nobel prize laureate) for nuclear spin resonance effects. The OBE can be written more simply with the help of the BLOCH-vector (here in the case without damping):

$$\frac{d}{dt}\begin{pmatrix} u \\ v \\ w \end{pmatrix} = -\begin{pmatrix} \Omega_0 \\ 0 \\ \delta \end{pmatrix} \times \begin{pmatrix} u \\ v \\ w \end{pmatrix} \tag{3.19}$$

For the case without damping, it can be shown that the BLOCH-vector always moves on the surface of a sphere with the radius of one:

$$u^2 + v^2 + w^2 = 1. \tag{3.20}$$

3.1.6 BLOCH-sphere

The states of a single two-level system can be represented as points on the surface of a sphere. The BLOCH sphere is in some kind analogous to the probability interval [0,1] for the classical bit. The lowest and the highest point of the sphere (the poles) correspond to the states where exact states can be measured. Figure 3.1 shows the BLOCH sphere. The upper pole corresponds to an occupation of 100% and the lower pole to 0%. These states are called the *pure* states (in quantum mechanics); for the case of a spin 1/2 particle e.g. spin down (spin up). This is valid for all two level systems. The points which are not on the surface, but inside $u^2 + v^2 + w^2 < 1$, can be interpreted too. There is no complete information about these states. These states are called the *mixed* states. The point in the middle of the sphere corresponds to the state without any information. Every measurement of a state on the BLOCH sphere corresponds to a projection of the state to the w-axis. Then the measurement correlates directly to the occupation probability of the state. There is no access to the phase with a simple measurement of the occupation probability.

The BLOCH-vector formalism can be applied to the optical resonance of two-level systems. This approach delivers a picture of the coherent processes in the quantum system, which is described by the motion of a vector in the three dimensional space. Therefore the BLOCH-vector is defined by the components which contain the dipole moment and the inversion, as well as the coherent properties of the state. As mentioned before, the time evolution is given by the time dependent SCHRÖDINGER-equation. With a practical approximation[1], it is possible to create a set of equations of motion, which are known as the optical BLOCH equations (OBE) 3.21.

$$\dot{u} = -\delta \cdot v \tag{3.21a}$$
$$\dot{v} = \delta \cdot u + \mu \cdot E \cdot w \tag{3.21b}$$
$$\dot{w} = -\mu \cdot E \cdot v \tag{3.21c}$$

Figure 3.1 shows the BLOCH-sphere. The states 1 and 0 correspond to the poles of the sphere. The component w represents the occupation probability of the two level system. u and v refer to the components of the complex transition matrix element, where u correspond to the dispersive and v to the absorptive component. v is called the absorptive component because the occupation probability w can be changed due to absorption of electromagnetic radiation, see 3.21c. δ is the energy detuning (between the transition frequency ω_0 and the frequency of the incident light ω_L). E corresponds to the envelope

[1] Half classical theory of light matter interaction without quantization of the beam field and the use of the *rotating wave approximation*

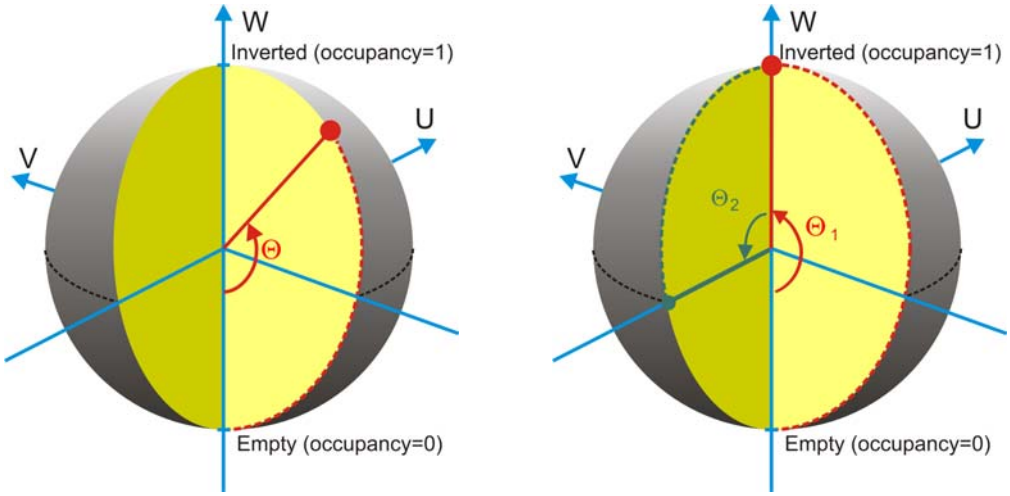

(a) A laser pulse rotates the BLOCH-vector with an angle of Θ.

(b) Excitation of the two level system with π-pulse followed by a $\pi/2$-pulse with phase shift of 90°.

Figure 3.1: BLOCH-vector shown on the BLOCH sphere.

of the electrical field amplitude. Figure 3.1 a) shows the BLOCH vector on the BLOCH sphere. With the rotating frame approximation, the components u and v define the phase of the system. As shown in equations 3.21a and 3.21b, a detuning δ directly affects the components u and v and thus the phase of the system.

The electromagnetic field is $\mathbf{E}(t) = E(t) \cdot [e^{i\omega t} + c.c.]$. The variable μ is directly proportional to the dipole transition matrix $d \equiv \hbar \cdot \mu/2$ of the regarded optical transition. Analytic solutions of the OBE can only be obtained with further approximations. The incident electromagnetic field is supposed to be perfectly monochromatic and resonant to the two level system. With the approximation of a constant electrical field $E(t) = E_0$, the components u, v and w show an oscillation behavior. This case is known as the RABI solution of the optical BLOCH equations. It is called RABI oscillation, analogous to the first evidence of an occupation oscillation in magnetic resonance phenomena.

3.2 Pulsed excitation

3.2.1 RABI oscillations

As mentioned before, an electromagnetic wave of a laser is able to excite a quantum mechanical two level system, with two discrete energy levels ($|0>$ and $|1>$), if the incident laser frequency is resonant to the transition frequency. If the system is already excited, further excitation results in stimulated emission. Absorption and stimulated emission follow up periodically. The oscillation takes place with the RABI-frequency, which is proportional to the laser field strength. Spontaneous emission leads to a damping of the RABI-oscillation. The spontaneous emission is not taken into account, up to now. The damping can be neglected if the laser field is so intense that the RABI frequency is much

higher than the decay rate caused by spontaneous emission. These oscillations were observed for the first time by RABI in the year 1936 in his works on spin systems.

3.2.2 RABI-solution for the case of exact resonance

The simplest solution of the OBE is obtained for the case of resonant excitation. The detuning $\delta = \omega_L - \omega_0$ is zero in this case.

$$\dot{u} = 0 \tag{3.22a}$$
$$\dot{v} = \mu \cdot E \cdot w \tag{3.22b}$$
$$\dot{w} = -\mu \cdot E \cdot v \tag{3.22c}$$

The dispersive component u of the BLOCH vector is therefore constant in time. The solution of equations 3.22b and 3.22c results in oscillations for v and w. From:

$$\ddot{w} = -\mu E \dot{v}$$

we obtain:

$$\ddot{w} = -\mu^2 E^2 w.$$

With the ansatz $w = A \cdot e^{i\omega t}$ we further obtain:

$$\omega = \pm\mu E = \pm\Omega_0.$$

with the already introduced RABI-frequency Ω_0. As solution one gets:

$$\rightarrow w = A(e^{i\Omega_0 t} + e^{-\Omega_0 t}) = 2A\cos(\Omega_0 t).$$

with the boundary condition $w(t = 0) = -1$ (occupation of the upper level is zero at the time zero) A is determined to:

$$\rightarrow A = -\frac{1}{2}.$$

Using the addition theorem $\sin^2 \frac{\omega t}{2} = \frac{1}{2}(1 - \cos \omega t)$ the solution results in:

$$w = 2\sin^2 \frac{\Omega_0 t}{2} - 1$$

The frequency of this oscillation corresponds to the RABI-frequency. It is directly proportional to the transition probability and to the electric field strength. For the case of an exciton two level system, the occupation probability of the $|1X\rangle$ state is given by

$$P_{|1X\rangle} = \frac{w+1}{2}$$

which results to:

$$P_{|1X\rangle} = \sin^2 \frac{\Omega_0 t}{2} = \sin^2 \frac{\Phi}{2} \tag{3.23}$$

μ describes the component of the dipole matrix element parallel to **E**. **E** corresponds to the envelope peak amplitude of the electromagnetic field.

$\Phi = \Omega_0 t$ is called the *pulse area*. For a time dependent field E (e.g. pulsed excitation), this results is given by:

$$\Phi(t) = \mu \int_0^t E(t')dt'. \tag{3.24}$$

For this case, w performs a RABI-oscillation with varying RABI-frequency. For the description of the final state of the two level system after an incident laser pulse with the length t_p, the pulse area is nevertheless given by $\Phi = \Omega_0 t_p$. Because the field amplitude is time dependent at a GAUSS-shaped pulse ($E(t) = E_0 \exp(-(t-t_0)^2/2\sigma^2)$), Ω_0 and t_p are taken as adequate averages. For this case, the relevant relations $\Phi \propto E$ and $\Phi \propto t_p$ are also valid in the integral description. If a two level system is resonantly excited, the BLOCH-vector rotates around the u-axis with the RABI-frequency Ω_0. The rotating angle of the BLOCH-vector after the pulse is given at the time t with $\Omega_0 t$. Figure 3.1 a) illustrates the motion of the BLOCH-vector after the interaction of a laser pulse. The oscillating occupancy probability is a function of the laser field strength (fixed pulse length). With a defined laser pulse, it is possible to excite the system with the probability of 1. The pulse area for a single inversion is called π-pulse. This is shown with the green function in figure 3.2 at $\Phi = \pi$.

3.2.3 RABI-solution in real systems

In reality, genuine two-level systems do not exist. There is always a certain interaction with other states and charge carriers. Even if the transition probability into other states could be neglected, this could lead to a dephasing of the system. This means that the coherence with the applied periodical excitation is lost. This leads to a damping of the RABI-oscillations, depending on the incident pulse area. At high excitation intensities, the same occupation probability arises for both states (see figure 3.2 (black curve)). On the BLOCH-sphere this corresponds to $w = 0$. If one takes the damping into account, the relation for the occupation probability (3.23) must be phenomenologically adapted to:

$$P_{|1X\rangle} = e^{-\gamma\Omega_0 t}\left(\sin^2\left(\frac{\Omega_0 t}{2}\right) - \frac{1}{2}\right) + \frac{1}{2} \tag{3.25}$$

γ corresponds to the damping parameter. The modification with the two factors $\frac{1}{2}$ gives the same occupancy probability for both states at high excitation intensities. Therefore the occupation probability function $P_{|1X>}$ will approximate $1/2$ at high pulse areas.

3.2.4 RABI-solution in the case of detuning

Due to the fast time evolution of the system, the laser energy must not exactly fit to the energy difference of the two energy levels ($\delta \neq 0$) [2]. The exact energy conservation is only correct here in the limit for long pule width. A detuning of the resonance in relation to the

[2] Consequence of the uncertain principle

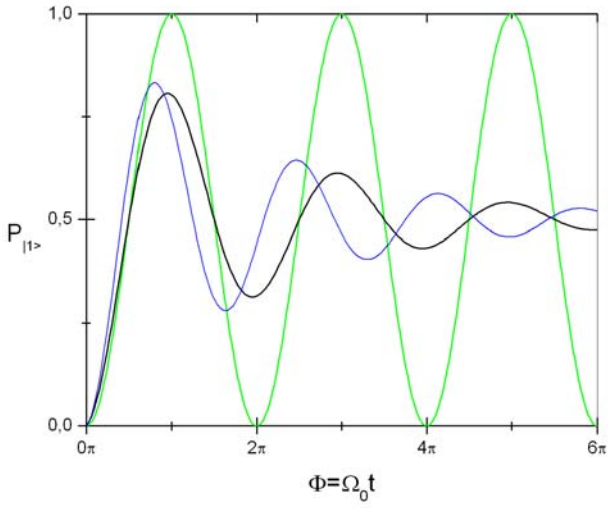

Figure 3.2: green: RABI-oscillations without dephasing and detuning; black: RABI-oscillations with damping and without detuning; blue: RABI-oscillations with dephasing and *slight* detuning

laser frequency leads, in this case, to a modification of the frequency and the amplitude of the RABI-oscillation.

$$P_{|1X\rangle} = \frac{\Omega_0^2}{\Omega^2} \sin^2\left(\frac{\Omega t}{2}\right) \quad \text{with} \quad \Omega = \sqrt{\Omega_0^2 + \delta^2} \tag{3.26}$$

where $P_{|1X\rangle}$ is assumed to be $P_{|1X>}(t = 0) = 0$. $\Omega_0 = \mu E$ is still valid in this case. Ω corresponds to a generalized RABI frequency where the detuning δ is factored in. Figure 3.2 shows the modifications of the RABI-frequency when a detuning is taken into account. In principle, the formula 3.26 is only correct for a constant RABI frequency Ω_0, e.g. for an excitation with a rectangular laser pulse in time. Due to the factor of Ω_0^2/Ω^2, the approximation of Ω_0 as an effective mean frequency is not generally correct. Additionally, the approximation of a perfect monochromatic pulsed laser is not realistic for a real experiment, where pulsed excitation with a spectral broadening is applied. A simulation of this situation, taking both effects into account, is non-trivial and not discussed here.

3.3 Dephasing

In reality, the coherent occupation oscillation of a two level system is disturbed more or less due to additional interactions with other states or charge carriers or due to a decay process. This leads to a loss of coherence, which results in a damping of the RABI oscillation. The OBEs (formulas 3.18) describe the two level system under coherent excitation. If a π-pulse excites the two level system to a occupation probability of 1, the system would

stay in this state forever if no dephasing process takes place. Therefore the optical recombination time sets an upper time limit for which coherent manipulations are possible. The analysis of the dephasing processes of a single quantum system is very interesting and also required in order to build a complete theoretical model. As a first approximation for the description of the damping in a quantum system, decay terms with empirical time constants are inducted into the OBE.

$$\dot{u} = -\delta \cdot v - \frac{u}{T_2} \tag{3.27a}$$

$$\dot{v} = \delta \cdot u + \mu \cdot E \cdot w - \frac{v}{T_2} \tag{3.27b}$$

$$\dot{w} = -\mu \cdot E \cdot v - \frac{\delta}{T_1} \tag{3.27c}$$

The decay time T_1 corresponds to the occupation component of the BLOCH sphere w (inversion) which is called *longitudinal* lifetime. This describes all inelastic interactions with the quantum system. A second decay time for the components u and v is introduced which is called the *transversal* lifetime T_2. In addition to the inversion, an elastic interaction can also lead to loss of coherence. For example, a phonon scattering process can lead to a loss of coherence but the occupation of the system can be retained. In this case, the oscillation would exhibit strong damping and a reduced transversal lifetime.

The transversal decay time T_2 implies a loss of the phase of the induced dipole moment. Here all processes which can lead to a loss of the phase relation between the incident electromagnetic field and the exciton dipole moment have to be regarded. A damping of the RABI oscillation can origin from T_1 and T_2 processes as well as from *pure-dephasing*. Both decay times are linked by:

$$\frac{1}{T_2} = \frac{1}{2T_1} + \sum_i \frac{1}{T_i^*} \tag{3.28}$$

The time constant T_i^* refers to all processes which will lead to a loss of the phase coherence but not to a change of the occupation. In the case without *pure-dephasing*:

$$\sum_i \frac{1}{T_i^*} \approx 0. \tag{3.29}$$

Under this condition the relation

$$\frac{1}{T_2} = \frac{1}{2T_1} \tag{3.30}$$

is valid. The in this work analyzed QD-states are able to decay by different processes, which exhibit different decay times. The ground state exciton is able to decay by a (bias voltage dependent) tunneling process (t_{esc}) or by an optical recombination (t_r). An excited exciton state can relax into the lowest energetic level (t_{rel}) or also decay by an optical recombination. Thereby, the occupation life time T_1 is mainly determined by the fastest decay process. In the case of the coherent manipulation of the ground state, no relaxation

processes can take place ($t_{rel} = \infty$). The occupation life time is determined by:

$$\frac{1}{T_1} = \frac{1}{\tau_r} + \frac{1}{\tau_{esc}} + \frac{1}{t_{rel}} \tag{3.31}$$

Where τ_r is constant, $\tau_\mathrm{esc} = \tau_\mathrm{esc}(V)$ is a function of the applied voltage, and $1/t_{rel}$ is zero. Then the dephasing of the single exciton ground state is given by:

$$\frac{1}{T_2} = \frac{1}{2}\left(\frac{1}{\tau_r + \tau_{esc}(V)}\right) \tag{3.32}$$

If the tunneling time τ_{exc} reaches values shorter than the optical recombination time τ_r, then the dephasing time T_2 is mainly determined by tunneling processes. The dephasing time of the QD state gives a lower limit for the homogeneous line width Γ_{hom} [Wog97]:

$$\Gamma_{hom} = \frac{2\hbar}{T_2} \tag{3.33}$$

For a typical lifetime of T = 300 ps of the exciton in a QD, the linewidth is very small $\Gamma_{hom} = 4,4\ \mu eV$. Experimentally, the homogeneous linewidth can only be determined if the detection setup has a higher energy resolution than the transition linewidth. When the ground state of one QD is resonantly excited, the absorbed and emitted photons have the same energy. Therefore, it is impossible in experiments with resonant excitation to separate the luminescence from the scattered light. In this work, the photocurrent technique is used for high resolution spectroscopy. Here, the QD system is resonantly excited by a narrow laser; the detection takes place in the photocurrent (tunneling processes).

3.4 Double pulse excitation and RAMSEY fringes

Another possibility for a manipulation of the BLOCH-vector is a double pulse excitation. Under the condition of the initial state $|0\rangle$, the phase of the system is defined by the first pulse. If the second pulse is in phase to the first one, the rotation of the BLOCH vector will continue with the same rotation direction as before. This means a further rotation around the u-axis, or in the case of a slight detuning, a slight inclined rotation axis. But if the phase of the second pulse is shifted with the angle of φ with respect to the first, the rotation axis of the second manipulation is also shifted with the angle of φ in the u-v-plane. With an excitation of a π-pulse followed by a $\pi/2$-pulse with a phase shift of 90°, one would be observed (a rotation on the BLOCH-sphere from $w = -1$ to $w = 1$) followed by a rotation from $w = 1$ to $u = -1$, see figure 3.1 b).

Up to now, a detuning of the system has not been considered. The case of a *small* detuning in a double pulse experiment is discussed in the following. Thereby the detuning is much less than the spectral width of the excitation pulses: $\delta/\tau_{pulse} \ll 1$. The detuning is so small that the pulses can be regarded as almost resonant to the transition, which means the first manipulation basically takes place around the u-axis. The first pulse defines again the phase of the two level system. The BLOCH-vector rotates in the *rotating-frame*-approximation around the w axis with the angular velocity $\dot{\varphi}$. At the arrival of the

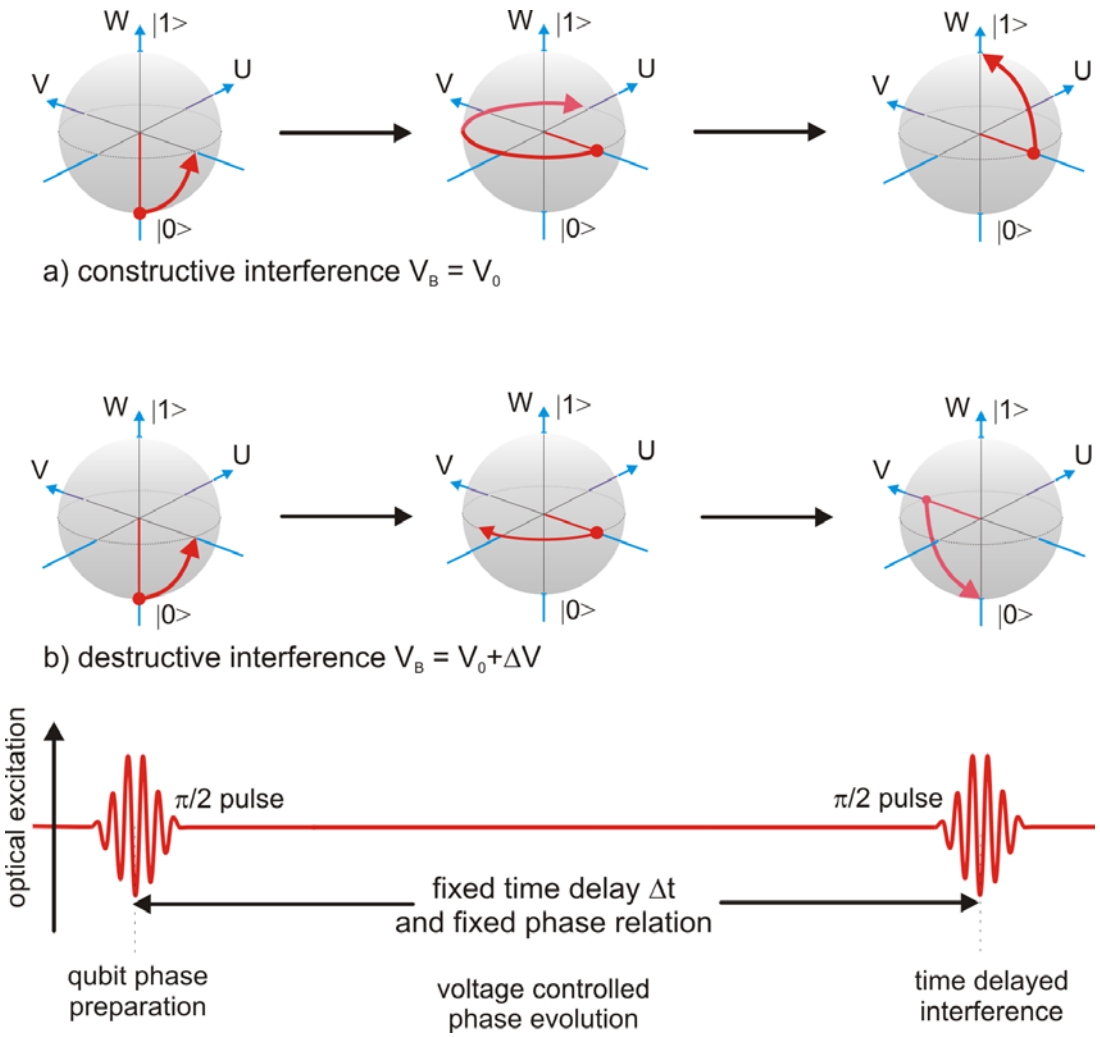

Figure 3.3: Origin of the RAMSEY-fringes. Comparing the cases of constructive (a) and destructive (b) interference.

second pulse (with the time τ_{delay}) the BLOCH-vector is turned in the u-v-layer with the angle: $\varphi = \dot{\varphi} \cdot \tau_{delay}$.

It is now considered that both pulses have the same pulse area of $\pi/2$ and the same phase. The first pulse rotates the BLOCH-vector from $w = -1$ to $v = -1$ (counterclockwise around the u-axis). For a detuning condition which results in the same phase at the arrival of the second pulse as for the first, $\dot{\varphi} = 2\pi n/\tau_{delay}$, the rotation will be continued to the point $w = 1$, see figure 3.3 a). For a detuning of $\dot{\varphi} = (2n+1)\pi/\tau_{delay}$, the BLOCH-vector is located at $v = 1$ at the arrival of the second pulse. Therefore the second manipulation will transfer the BLOCH-vector into the initial state. For the cases $\dot{\varphi} = (n+1/2)\pi/\tau_{delay}$, the BLOCH-vector is located at the point $u = \pm 1$. At this point on the BLOCH sphere, no further manipulation can take place. The occupation probability after the double pulse manipulation oscillates therefore depending on $\dot{\varphi}$ and the time

delay between the two pulses τ_{delay}:

$$P_{|1\rangle} \approx \cos^2(\dot{\varphi}\tau_{delay}/2) \tag{3.34}$$

These oscillations are known as RAMSEY-interferences [Ram90]. The main advantage of the double pulse setup is the high sensitivity of the system on a small detuning δ in particular at long time delays. It is thereby irrelevant whether the detuning is done by changing the excitation energy or by variation of the transition energy of the two level system. In this work, the possibility to tune the transition energy with the quantum confined STARK effect (QCSE) is used. As a matter of fact, the time delayed interference in this double pulse interference becomes possible, because the phase information of the first pulse is stored within the dephasing time in the quantum system.

Figure 3.3 illustrates the origin of the RAMSEY fringes using the picture of the BLOCH-sphere. Here the two extreme cases of constructive and destructive interference are displayed. In both cases, the first laser pulse excites the QD with a $\pi/2$ pulse. This interaction rotates the BLOCH vector to the equator. The difference between the two cases is a slight detuning, which is done in the used material system by an additional applied voltage ΔV. In the case of constructive interference (a), the BLOCH vector arrives at the initial point on the equator ($v = -1$) at the time when the second interaction takes place. Then a constructive interference is possible, which leads to a fully excited QD state. In the other case (destructive interference (b)), a slight different voltage (respectively detuning) is applied to the QD. The phase evolution results at the end of the time delay in the opposite state ($v = 1$) as before. The second $\pi/2$ interaction transfers this state back to zero. With a continuous variation of the detuning, the final state oscillates between the states $|0\rangle$ and one $|1\rangle$. As mentioned before, the tunneling process corresponds to a projection of the BLOCH vector on the w-axis. Thereby a detection of the final state is possible in the PC experiment, where the state $|1\rangle$ corresponds to a current of 12.8 pA.

3.5 Continuous Excitation

3.5.1 Saturation

In the case of continuous excitation, the statistical occupation of a two level can be described using rate equations. There are four different transitions possible, where each can be specified with different coefficients (called EINSTEIN-coefficients). The normal absorption is written with the EINSTEIN-coefficient B_{01}, the stimulated emission by B_{10} and the spontaneous emission with A_{10}. The indices refer to the initial and the final states. The initial (lower) state is called "0" and the final (upper) state "1". In the case of photocurrent measurements, a fourth transition can take place. The tunneling can be described by the tunneling rate proportional to $1/\tau_{tunnel}$. In the case of p-shell excitation, the decay of the excited state takes place by a relaxation and a recombination process. The decay rate here is proportional to $1/(\tau_{rel} + \tau_r)$. In order to describe both cases, τ_{decay} is introduced, which represents τ_{tunnel} in the first case or $\tau_{relax} + \tau_{recom}$ in the second case. For the transition

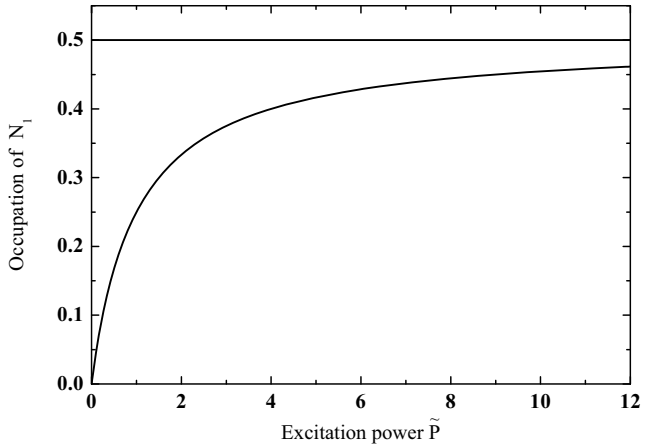

Figure 3.4: Occupation probability of the upper level depending on the normalized excitation intensity $\widetilde{P}$. For high excitation intensities the occupation approximates the value 1/2.

from the upper level into the lower level one obtains the following rate equation:

$$\frac{dN_1}{dt} = -A_{10}N_1 + B_{10}N_1\rho + B_{01}N_2\rho + \frac{N_1}{\tau_{decay}} \tag{3.35}$$

where ρ refers to the energy density to the incident field. In the two level system the following relations also apply: $N_0 + N_1 = 1$ and for the EINSTEIN-coefficients $B_{01} = B_{10}$. In the stationary case considered here, also the following relation holds:

$$\frac{dN_1}{dt} = \frac{dN_2}{dt} = 0. \tag{3.36}$$

Only the absorption and the stimulated emission depend on the intensity of the incident laser field. In the limit of high excitation intensities, this results in the same occupation probabilities for both states. Therefore one gets for the occupation probability of the level N_1, depending on the excitation intensity:

$$N_1 = \frac{1}{2}\,\frac{\widetilde{P}}{\widetilde{P}+1} \tag{3.37}$$

where $\widetilde{P}$ corresponds to a normalized (dimensionless) excitation intensity. This parameter is a basic property of the two level system, which can be also derived from the RABI-frequency Ω_0 (see next chapter: $\widetilde{P} = \Omega_0^2 T_1 T_2$).

3.5.2 Power broadening

As a direct result of the saturation of the transition of the two level system is the so called *power-broadening*. This effect describes the power induced linewidth broadening of the resonance. The derivation of the broadening effect takes place as follows (taken from reference [AE75] and adapted to an exciton):

It is simple to show that the following equation can be derived from the optical BLOCH equations, see formula 3.27. If T_2 is very short, then u and v will quickly reach the quasi-steady-state values:

$$u = -\mu E T_2 \frac{\delta T_2}{1 + (\delta T_2)^2} w \tag{3.38}$$

and

$$v = \mu E T_2 \frac{\delta T_2}{1 + (\delta T_2)^2} w. \tag{3.39}$$

Under these conditions, the inversion obeys the simple equation:

$$\dot{w} = -\frac{\xi \widetilde{P} w}{T_1} - \frac{\delta}{T1} \tag{3.40}$$

where ξ is the LORENZIAN factor

$$\xi = \frac{1}{1 + (\delta T_2)^2}. \tag{3.41}$$

and $\widetilde{P}$ is defined as the dimensionless intensity $\widetilde{P} = (\mu E)^2 T_1 T_2$. The steady state values (taken by u, v, and w) are of particular interest after all of their temporal oscillations have been damped out. The steady value for the inversion in the long time limit is:

$$w = \frac{w_{\text{eq}}}{1 + \xi \widetilde{P}} \tag{3.42}$$

In absence of any incoherent input of w_{eq} is equal to -1. For such a two level system the steady-state inversion has the line shape:

$$w = -\frac{1 + (\delta T_2)^2}{1 + (\delta T_2)^2 + \widetilde{P}}, \tag{3.43}$$

where δ corresponds to the detuning and $\widetilde{P}$ to the dimensionless intensity. This expression shows how the energy stored in the system depends on the intensity of the incident field. For a given detuning, the steady-state inversion becomes increasingly less negative as $\widetilde{P}$ increases. The maximum occupation (w_{max}) is then given by:

$$w_{max} = -\frac{1}{1 + \widetilde{P}}, \tag{3.44}$$

which is always negative for an incoherent field. In order to derive an analytic expression

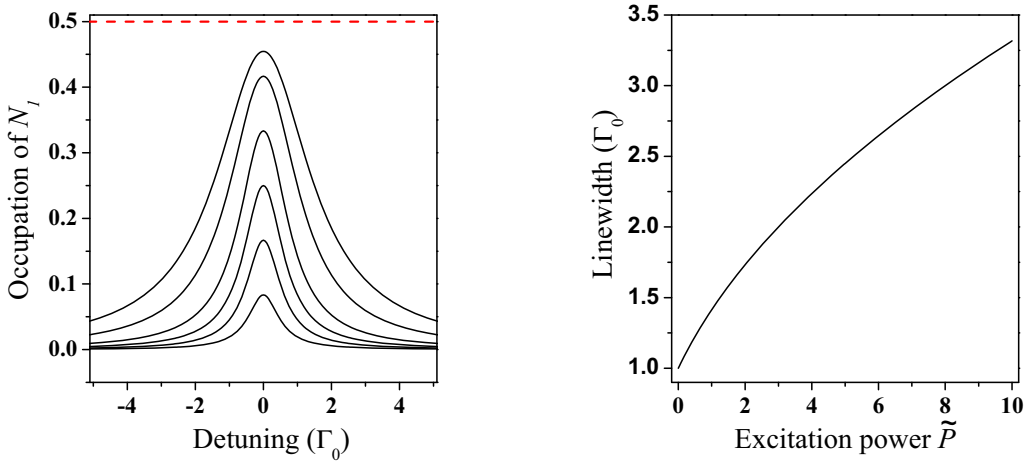

Figure 3.5: left: occupation probability N_1 depending on the detuning between the laser and the resonance, displayed for different excitation intensities $\widetilde{P} = 0,2;\ 0,5;\ 1;\ 2;\ 5;\ 10$. right: linewidth dependence from $\widetilde{P}$. The broadening of the linewidth is a direct result of the power dependent saturation. This effect is known as *power-broadening*.

for the width of w depending on the incident intensity, one has to solve formula 3.43. The half height of w_{max} is in this case not $1/2 \times w_{max}$ because w_{min} is -1 and not zero. Thus, $w_{1/2}$ is:

$$w_{1/2} = \frac{1}{2}\left(w_{max} - \frac{1}{2}\right). \tag{3.45}$$

The equation 3.43 must be solved for the case of formula 3.45.

$$\frac{1}{2}\left(w_{max} - \frac{1}{2}\right) = -\frac{1 + (\delta T_2)^2}{1 + (\delta T_2)^2 + \widetilde{P}}, \tag{3.46}$$

The detuning δ (at $w_{1/2}$) corresponds to the linewidth (FWHM) of w, which is then called $\Gamma(w_{1/2})$. The conversion of formula 3.46 leads (after some algebra) to the expression:

$$\Gamma(w_{1/2}) = \frac{1}{T_2}\sqrt{1 + \widetilde{P}} = \frac{1}{T_2}\sqrt{1 + T_1 T_2 (\mu E_0)^2}, \tag{3.47}$$

The width at half height $\Gamma(w_{1/2})$ of the profile of w is a function of the incident intensity. With increasing intensity the linewidth of the profile of w increases, which is called *power broadening*.

Finally, it should be mentioned that w is negative for all values of E_0. An incoherent saturating field can never produce a positive inversion. An important implication of formula 3.43 for the steady state inversion is that a system near to the resonance is no pure absorber, since it has been stimulated by E_0 partially out of their ground state.

Phenomenological one can say that at low excitation intensity the occupation probability of the upper level increases proportional to the excitation power. The shape of the linewidth only slightly changes in this region. But for higher excitation intensities the amplitude of the resonance will not increase proportional to the excitation power, because the system gets close to its saturation. The middle of the resonance reaches the saturation value (occupation: 1/2) earlier than the sides by increasing excitation intensity. It is possible that the middle of the resonance has nearly reached the maximum, but the sides of the resonance are still able to increase. This will result in a broadening of the absorption line. The *power broadened* absorption line is again LORENZ- shaped, but with a larger linewidth of Γ.

Figure 3.5 shows the occupation intensity depending on the detuning between the laser and the transition of the two level system displayed for different values of $\widetilde{P}$. The saturation value increases the linewidth of the resonance independent from all dephasing processes. For all analysis of the measurements, one has to take the limit of the linewidth for vanishing excitation power in order to use the correct basic linewidth.

4 Experimental setup

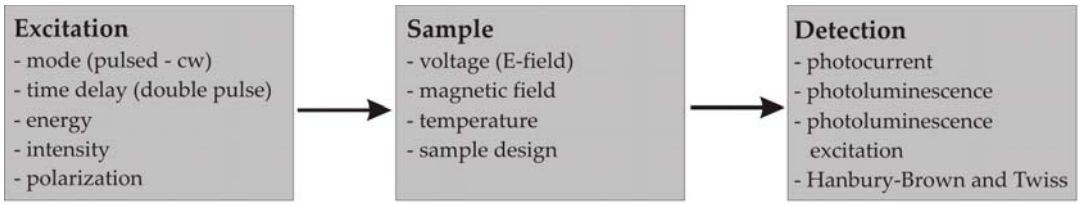

Figure 4.1: Pattern of the experimental setup.

Figure 4.1 shows the scheme of the experimental setup, beginning at the excitation parameters, followed by sample parameters, and finally the detection options. There are different possibilities for laser excitation. A HeNe laser can be used for basic characterization (voltage dependent PL at interband excitation see figure 5.1) of the QDs. The tunable Titan:Sapphire (TiSa) laser can be used for high resolution photocurrent spectroscopy of the QD ground state or for resonant excitations of higher QD states. If the TiSa laser system works in the pulsed mode, the QD state occupation can be coherently excited (and tested for possible coherent state manipulations). By integrating a MICHELSON interferometer into the excitation beam, a single pulse can be split into two pulses. By adjusting the time delay between the two pulses, the dephasing of the QD state can be analyzed. The intensity of the incident laser beam allows for power dependent investigations. Furthermore, the polarization of the laser beam can be adjusted in continuous wave as well as in the pulsed mode in order to analyze the absorption properties of the QD-state.

At the sample, several parameters can be adjusted. If the sample is integrated in a diode structure, an external voltage can be applied. This results in an internal electric field (additional to the build-in voltage) at the sample. This electric field affects the QD states via the STARK effect. Similar to the electrical field, the sample can be exposed to an external magnetic field. The magnetic field leads to a ZEEMANN splitting of the QD states. Apart from electric and magnetic fields, the temperature of the sample can be adjusted. The change of temperature is controlled by a heating resistor, attached below the sample carrier. Increasing temperature will lead to a line broadening and energy shift.

For detection, several methods are available. A simple, reliable and frequently used experimental method is photoluminescence (PL) spectroscopy. With interband excitation (HeNe laser - above the GaAs band gap), charge carriers are generated in the region of the QD. These are able to relax into the QD states. There they can recombine and show characteristic spectra in the luminescence. Another kind of PL method uses a resonant excitation of higher QD-states. This is called the photoluminescence excitation (PLE) spectroscopy. The excitation wavelength is thereby tuned continuously. When the laser energy fits to a higher state, the QD can be occupied with an exciton. After a relaxation

process, the recombination can be detected in the ground state PL.

If the QD is embedded in a diode structure, generated charge carriers can tunnel out of the QD. This is possible with a suitably applied voltage. In this region, all QD states which decay by tunneling processes can be investigated. Due to the STARK effect (voltage), it is possible to shift the QD state with respect to the laser energy. If the laser energy has an spectral overlap with the QD state, an exciton can be generated. Then the exciton can tunnel out of the QD and produce a photocurrent. As a consequence of the STARK effect, the *I*-*V*-characteristics reflects the energy spectra. Therefore, this method is called photocurrent (PC) spectroscopy. It is also possible to perform this kind of spectroscopy at excited QD states, which is then called photocurrent excitation (PCE).

Apart from the lifetime, a QD system exhibits different timescales for different properties, e.g. optical recombination time, lifetime of an excited state, tunneling times, dephasing times and so on. Furthermore, there are different timescales of the experimental setup which have to fit to the QD system, e.g. the laser repetition time, pulse length, pulse width, and time delay at double pulse excitation. Some of these timescales can be controlled from outside, whereas others are fixed. The longest time period is the laser pulse repetition time of 12.5 ns. The fastest process is the dephasing of the LO-phonon assisted absorption, which is in the range of the laser pulse length (1.7 ps). All processes in this work are taking place within these four orders of magnitude on the timescale. All experimental (time-) parameters which are important for this spectroscopy are discussed in the experimental sections.

This chapter is arranged as shown in figure 4.1. In the first section the excitation setup is discussed. Then the sample design is explained, followed by the discussion of the different detection methods.

4.1 Excitation

For the first characterization of a QD sample, a HeNe laser is used for photoluminescence measurements. The HeNe laser can be coupled to an optical fiber, or also directed as a free beam to the sample. The beam intensity is adjusted by an attenuator cascade, which is installed before the fiber coupler. For resonant excitation, the HeNe laser is replaced by the TiSa laser. The upper part of figure 4.2 shows the schematic view of the TiSa laser system. The TiSa laser is pumped by the Verdi V6. A part of the TiSa laser light is coupled out by a beam splitter and supplied to an auto-correlator for pulse analysis. Another part is checked in the spectrometer for the correct excitation wavelength.

4.1.1 HeNe-Laser

For the non-resonant (to a QD state) excitation over the band gap of the bulk semiconductor (GaAs), a HeNe laser with an emission wavelength of 632,8 nm (1,96 eV) is used. This laser radiation generates electrons and holes all over the semiconductor bulk. The charge carriers can then recombine from the GaAs, from the wetting layer and from the QD. Each of those recombination processes has its own characteristic luminescence, which is always helpful for setup adjustment. An interference filter is mounted behind the laser, which lets only the actual laser line pass through.

4.1.2 Ti:Sa-Laser

For resonant investigations of an QD state, a commercial titanium sapphire (TiSa) laser system is used (type: Mira 900 from `coherent`). Since the titanium sapphire crystal possesses a very large amplification range, the emission wavelength of such a laser system is tunable in a range from 700 nm to 980 nm, which covers the area of the InGaAs QD states. The TiSa can work in two different modes, pulsed and continuous wave. The laser system used here can be (quasi-) continuously tuned by a birefringence filter (LYOT filter). In order to control the wavelength also computer based, the originally installed micrometer for filter adjustment was replaced by a motorized unit. The laser system provides pulses in the range from 1 to 3 ps. The pulse length is not directly tunable, but varies slightly with adjustment. The resonator length is optimized for a laser pulse frequency of 80 MHz. The maximum average optical output power is approximately 1 W. The pumping laser is a diode-pumped, frequency-doubled Nd:$YV0_4$-ring-laser (Coherent Verdi V6), which provides a high stability of power output and outstanding beam quality due to single longitudinal mode emission. The maximum optical power output is 6.5 W at a fixed wavelength of $\lambda = 532$ nm. The appropriate adjustment is done automatically with the integrated β-lock system, so that the wavelength of the (modelocked) laser can be varied within a certain range without interruption.

Pulse analysis

By means of a beam splitter, a part of the laser beam is directed into an auto-correlator (model "mini" of the company APE) for pulse analysis. In the auto-correlator, the laser beam is divided into two parts in an interferometer arrangement, whereby one arm of the

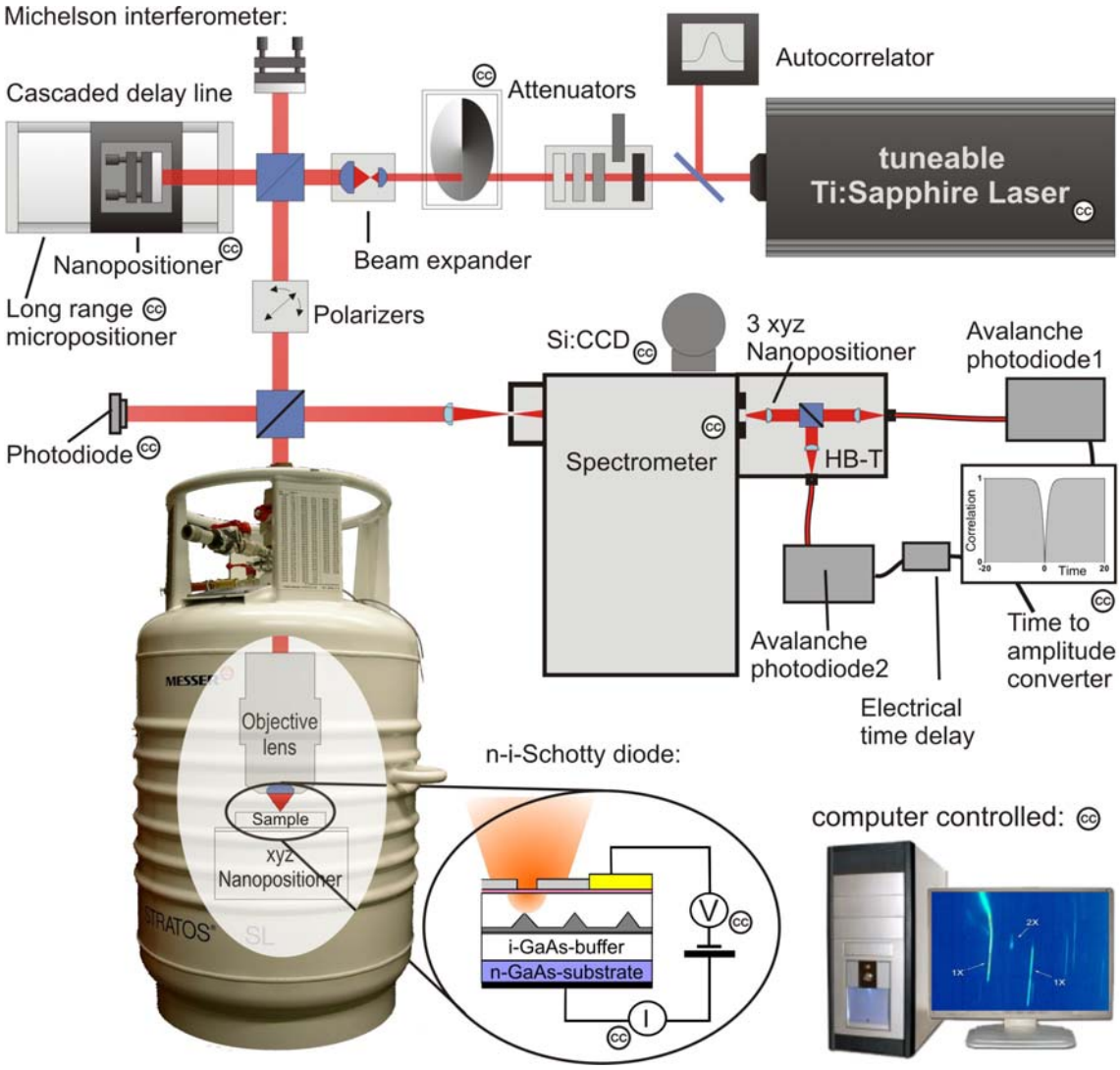

Figure 4.2: Scheme of the experimental setup. All devices which are controlled by the computer are signed. See text for a detailed description.

pulse shape	I(t)	$\Delta t_P/\Delta t_{AK}$	$\Delta t_P \Delta \nu$
rectangular	$I(t) = 1; \quad \lvert t\rvert \leq t_P/2$ $I(t) = 0; \quad \lvert t\rvert > t_P/2$	1	1
GAUSS-shaped	$I(t) = \exp(-\frac{4\ln 2 \cdot t^2}{\Delta t_P^2})$	0,707	0,441
hyperbolic secant	$I(t) = \mathrm{sech}^2 \frac{1,76t}{\Delta t_P}$	0,648	0,315
LORENTZ-shaped	$I(t) = \frac{1}{1+4t^2/\Delta t_P^2}$	0,5	0,221

Table 4.1: Autocorrelator product for different pulse shapes. Δt_P corresponds to the full width at half maximum (FWHM) of the intensity envelope of the pulse, Δt_{AK} and $\Delta\nu$ the FWHM of the autocorrelator function respective the pulse spectrum.

interferometer is periodically varied in distance. This length variation can be converted over the speed of light into a temporal variation of a partial pulse with respect to the other. Thus, the time measurement in the picoseconds range is transferred to a substantially simpler linear measurement in the 0,1 mm range. The detection of the interferometer signal is done by a nonlinear crystal, in which a frequency-doubled signal is produced only at overlapping partial pulses. The resulting signal is a result of a convolution of the laser pulse with itself: $I_{2\omega}(\tau) \propto \int I_\omega(t) \cdot I_\omega(t+\tau)dt$. This is generally broader than the original signal and must therefore be multiplied by an appropriate factor to receive the actual half width of the laser pulse, see table 4.1. Figure 4.3 shows the spectrum of a laser pulse in the picosecond mode (crosses). The appropriate sech^2-fitcurve (line) shows a very good agreement with the experimental data. In theoretical publications, GAUSS pulses are frequently assumed. These do not differ substantially from sech^2-pulses, but the sech^2-pulses exhibit here a slight better agreement. The sech^2 shape refers to the intensity distribution. The physically important, but directly not accessible amplitude of the electrical field vector (sech-envelope) has to be calculated. The pulse form in the time domain can be obtained directly from the FOURIER transformation of the frequency spectrum. A comparison of measured time range with the indicated values in table 4.1 shows that the used laser pulses are basically FOURIER transform limited. Both for the time and for the spectral distribution of the laser pulses, a hyperbolic secant form is assumed.

4.1.3 Optical Setup

Figure 4.2 shows the general experimental setup. The excitation intensity can be adjusted with the help of different neutral density filters (coarse) and a computer controlled filter wheel (fine). The back of the filter wheel is not sufficiently anti-reflection coated, at least in the close-infrared spectral region. This causes unwanted interferences. Therefore the filter wheel is placed diagonally to the incident beam. Because of the slow adjustment speed of the filter wheel, an additional power control unit was developed (see chapter 4.1.4). The power control suppresses strong intensity jumps which arise by tuning the laser energy. After the power control unit, the beam can be directed into a MICHELSON interferometer in order to generate double pulses, shown in the upper left side of figure 4.2 (for description see chapter 4.1.5). The free space setup easily makes a polar-

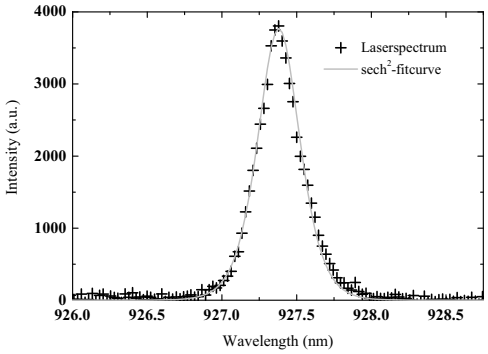

Figure 4.3: Spectrum of the Ti:Sapphire laser in the picosecond mode (crosses) and a sech^2-fitcurve (line).

ization control of the excitation beam possible (linear: $\lambda/2$ and circular $\lambda/4$). The beam is steered towards the sample holder with the help of different mirrors. At the top of the sample holder, the laser beam is split in two parts by a pellicle beam splitter (92 % transmission) or beam splitter cube (50 % transmission). The transmitted part is directed onto a photodiode in order to measure the relative intensity of the laser beam. Figure 4.2 shows the experimental setup schematically. In the real setup, the laser beam is directed onto the sample holder from the side. The reflected part is directed into the dewar towards the low temperature microscope (see 4.1.6). The luminescence from the sample passes the beam splitter again. The transmitted part is directed towards a CCD camera to check the laser focus geometry via a flip mirror. Otherwise the luminescence is coupled into the spectrometer via free beam or fiber optics. At the sample holder itself, an inspection unit is mounted. An IR-LED can illuminate the sample via a flip mirror. The reflected light can be displayed on a CCD camera in order to position the sample in the middle of the objective. All measurements are controlled by a single computer.

4.1.4 Power control

As already mentioned, the laser energy does not remain constant by tuning the wavelength. In PLE measurements, intensity variations of the excitation generate noise or ghost peaks along the energy axis. In order to compensate intensity variations, a power control unit was developed. The laser beam (0,8 mm in diameter) is focused by an aspheric lens onto a pinhole. The focus size depends on the beam diameter and the focal length of the lens: $D = \frac{\lambda f}{r}$. Here, f corresponds to the focal length, r to the input beam diameter ($1/e^2$) and λ to the wavelength. For the parameters here, a focus size of 10 μm (1/e decay) results. The pinhole diameter is selected slightly smaller than this focus size, here: 5 ± 1 μm. The aspheric lens can be pre-positioned in three directions in space. In addition, the distance pinhole-lens (Δx in figure 4.4) can be controlled with a closed loop nano-positioner (80 μm walk). If the distance is changed from the focal condition, the

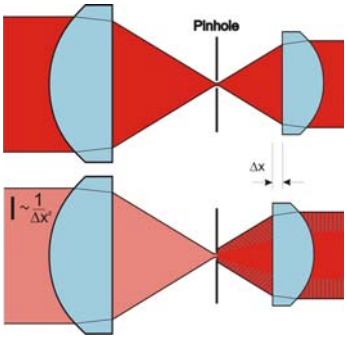

Figure 4.4: Power control unit and beam expansion. The output intensity is a function of the distance between the first lens and the pinhole. A reduced distance leads to reduced laser intensity.

transmitted intensity is inversely-proportional to the square of the distance $I \propto 1/(\Delta x)^2$. The laser beam is collimated by a second lens (achromatic) after the pinhole. On the sample holder, a photodiode is mounted where the laser intensity can be measured and hence stabilized. Due to the high intensities, a high power pinhole must be used. In addition, the laser intensity must still be reduced with a neutral density filter before the power control, in order to avoid damage to the pinhole. By proper choice of the focal length of the output lens, the beam expansion can be controlled. The output lens is fixed with respect to the pinhole. A beam expansion is necessary to guarantee optimum illumination of the objective at the sample holder.

4.1.5 MICHELSON interferometer

For the measurement of the dephasing time, two equal and successive laser pulses with precise and adjustable timing are needed. This is realized by an interferometer, which is positioned behind the filter wheel (see figure 4.2). One interferometer mirror is attached on a controllable one dimensional positioner. For the dephasing measurements, two different regime of changes of distance must be examined. The desired change of distance within the μm range is controlled by the closed loop nano-positioner. In order to measure the decrease of the interference ability depending on the time delay between the two pulses, larger time delays have to be provided. Therefore the interferometer mirror is adjusted with the help of a long range positioner, where the position can be controlled within the range of $\approx$0.1 m. The MICHELSON interferometer is used for the analysis of the QD state dephasing. The QD-state is excited with two time delayed $\pi/2$-pulses. A small change of the distance of one interferometer mirror within the range of 0 and 100 μm with an accuracy of 25 nm affects the phase of the second pulse in relation to the first pulse. This corresponds to 1/40 wavelength and a time resolution of 0.17 fs. The variation of the relative phase (piezo positioner) leads to an interferogram. The change of the amplitude of this interferogram over a longer time scale is detected by a point to point change of the long range positioner.

4.1.6 Low temperature microscope

All measurements presented here are performed in a liquid helium (He) dewar at 4.2 K. The beam, which is directed into the He dewar, is focused by an objective. In order to position the sample under the laser focus, a three dimensional piezo positioner is used (see figure 4.2). The z-dimension controls the focus length, and the x and y axis, the lateral position of the sample. The objective and the piezo positioner form the low temperature microscope, which is inserted in an outer tube. This tube must be evacuated to avoid the condensation of humidity when cooling down the sample holder. After the evacuation the tube is filled with a small quantity of gaseous helium. This is done for a better thermal exchange between the low temperature microscope and the liquid helium in the dewar. The LT-microscope is mounted on an inner tube. The electrical connections from the sample to the ADC and the DAC are integrated in the inner tube with two coaxial cables. A very important item here is the choice of the best compromise for the objective. In order to get high PL intensities, the objective should have a high numerical aperture (NA). But on the other hand, objectives with a high NA have a very low working distance. This can be a problem, if the objective makes contact with the bond wires. Another problem can be an insufficient color correction of the objective. A bad color correction results in different focus length for excitation and luminescence, which cannot be optimized at the same time. One has to make a compromise between good excitation and good luminescence output. Here a ZEISS objective (100x; 0.75 NA) is used with a comparatively good color correction and a working distance of about 0.3 mm.

4.2 Quantum dot photodiodes

This chapter gives a general introduction into the structure and the optical characteristics of the investigated sample. The presented measurements refer to the particular QD, which is examined in the further chapters. The sample was developed in 1999 at the WALTER SCHOTTKY institute in Garching, in particular for photocurrent spectroscopy. In the following, the requirements for PC spectroscopy on a single QD are described, followed by remarks on the band-diagram, the diode design, and the near field shadow mask.

4.2.1 Sample structure

For PC spectroscopy on single QDs, the samples must fulfill some principle conditions. These concern both the layer sequence of the samples and the characteristics of the QDs themselves. Additionally, strict requirements also apply to the crystal quality, the spectral position, and the QD-density. Since electrical tuning is necessary for the PC measurement, the QDs are integrated into a diode structure. The QDs are embedded in a layer of intrinsic bulk material, see figure 4.5 b). The electric tunability is one of the most important elements of this work. By means of the STARK effect, the transition energy of the QD can be controlled extremely precisely. This is the basis for the high resolution spectroscopy method, which is discussed in chapter 6.1. For the photocurrent measurements, two contacts are necessary, above and below the QD-layer. This can be provided by doped regions on both sides of the QD layer (*p*-*i*-*n* diodes or *n*-*i*-*p* diodes). With *n*-*i* or *p*-*i* diodes on the other hand, it is possible to use an doped substrate as a back contact, and a metal-semiconductor contact (SCHOTTKY contact) as front contact. The photo diodes should exhibit a high blocking ability, so that the PC signal is not accompanied by too high dark-current. Furthermore, the blocking behavior of the diodes must be sufficient for the field strengths required for the PC measurement. The required field strengths depend on the tunneling probability of the charge carriers. The electric field for PC amounts to approximately 30 kV/cm at the examined InGaAs/GaAs QDs sample. The tunneling probability depends on the barrier height and distance. A short distance leads to a short lifetime in the QD and therefore to strong broadened resonances in the photocurrent signal. Thus, a large distance between QD layer and back contact leads to longer lifetimes. The breakdown field strengths of the used *n*-*i*-photodiodes are clearly higher than 150 kV/cm (see reference [Fin01] and [Beh03]). A detailed description of the individual processing steps and sample parameters can be found in [Fin01] (sample 120799.2). For PC measurements of the QD-ground states, the sample structure should be designed in such a way that no charge carriers are permanently in the QD. With the examined *n*-*i*-diodes, a durable charging of the QDs with charge carriers can be prevented by a suitable reverse voltage.

The layer sequence of the examined *n*-*i*-photodiode is shown in figure 4.5 a). The distance between QD-layer and back contact is 40 nm. Other samples with other distances were examined in [Fin01] and [Beh03]. The sample consists of the following layers: On a doped n^+-GaAs-substrate a buffer layer of 3000 Å *n*-doped GaAs is grown, followed by an AlAs/GaAs super-lattice and further *n*-doped GaAs layers. Subsequently, intrinsic

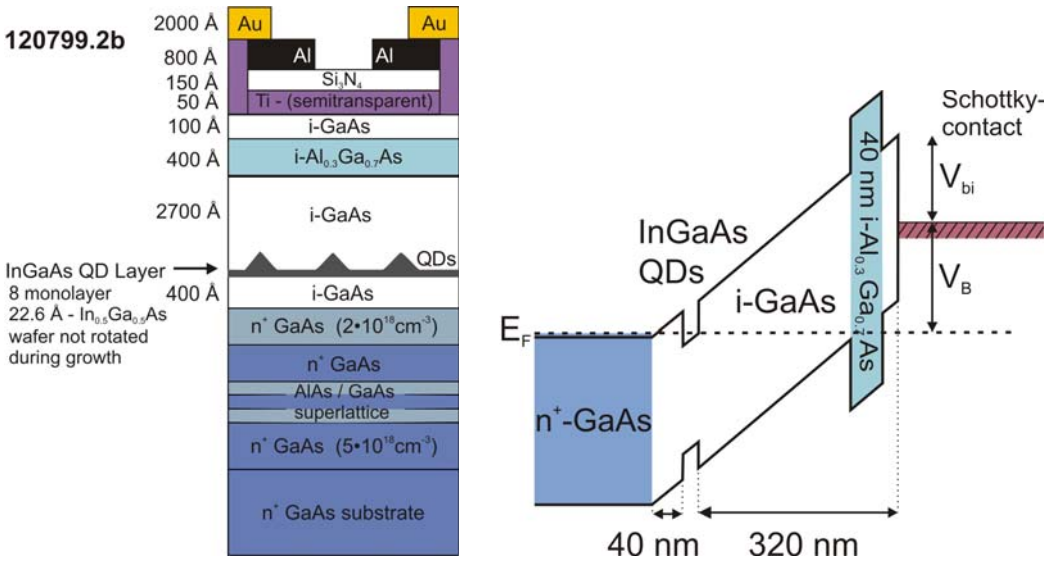

(a) Layer sequence of the *n-i*-photodiode. (b) Band structure at applied reverse bias voltage.

Figure 4.5: Sample design

GaAs with a thickness of 400 Å and a 22.6 Å undoped $In_{0.5}Ga_{0.5}As$ were deposited (formation of self organized QDs). After 2700 Å of intrinsic GaAs, a 400 Å thick $Al_{0.3}Ga_{0.7}As$-layer and a 100 Å surface layer (*i*-GaAs) follow. Figure 4.5 b) shows the band-diagram under reverse bias of the photodiode. The electric field strength within the intrinsic region of the diode results from the built-in voltage V_{bi} and the applied voltage V_B. For the connection between electrical field strength F and the voltage V_B applied between the SCHOTTKY-contact and the doped back contact, one gets the following relation:

$$|\vec{F}| \cong (V_B + V_{bi}) \cdot 27.78 \cdot 10^3 \frac{1}{\text{cm}}.$$

Here V_B corresponds to the applied bias voltage which is added to the built-in voltage ($V_{bi} \approx 0.8$ V). In the following, the properties of the charge carriers are discussed on the basis of this band diagram. These are, for example, the tunneling of charge carriers from the QDs of high electric field strengths and the charging of the QDs from the n-doped back contact.

4.2.2 Diode design

For a good design of the *n-i*-photodiodes, some parameters must be suitably selected. Special attention applies to the location of the QDs and the thickness of the intrinsic region. A change in the total thickness of the *i*-layer affects, as already mentioned, the resonance width in the PC spectroscopy and determines the voltages needed for the PC measurements. The voltage range of a diode follows directly from the electrical field strengths. With too large *i*-layer thickness, the dark current can increase and limit the

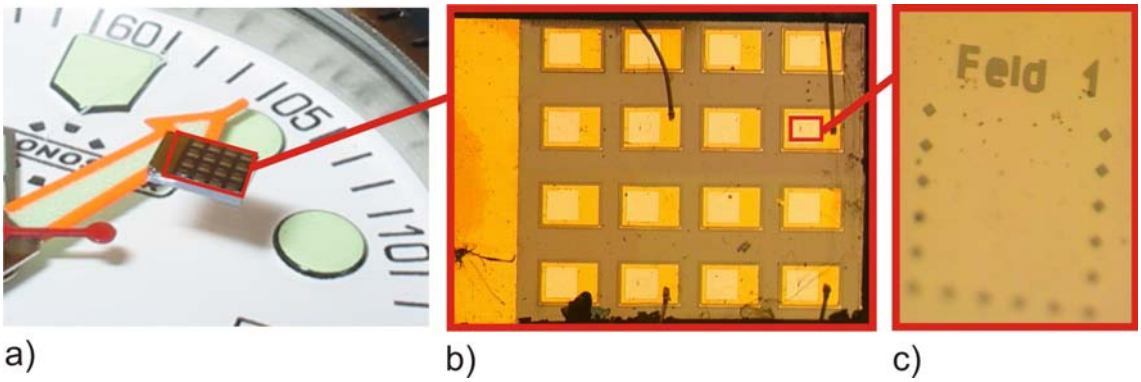

Figure 4.6: Sample pictures. a) sample on a watch. b) (Au-)bonded sample with a view from the top. A single field has a size of 300·400 μm^2. c): Al-shadow mask and boundary marks.

field strength range usable for PC measurement. The distance between the n-doping and the QDs, as well as the electric field strength, controlls the occupation of the QDs with electrons. The influence of the spacer layer thickness was examined by voltage-dependent PL-measurements of individual QDs in [Fin01]. There it was shown that for low field strengths the QDs are occupied on average with additional electrons from the n-area. With doubling of the spacer layer thickness from 20 nm to 40 nm, this threshold of, for instance F=57 kV/cm, is reduced to F=30 kV/cm. This reduction can be explained by the relative energetic level of the electron ground state in the QD and the FERMI-energy in the n-area. This spacer thickness determines the electron occupation of the QDs. Up to this point, the QDs are occupied with additional electrons (single electron charging). Beyond this threshold, the QDs are no longer occupied with electrons.

4.2.3 Near field shadow masks

In order to realize PC spectroscopy for individual QDs, an optical isolation of a single QDs is necessary. The sample used in this work exhibits near field apertures to address individual QDs by selective optical excitation. On the surface of the photodiode, a semi-transparent top gate is applied (5 nm Ti), followed by 80 nm of Al, see figure 4.5 a). Subsequently, small holes are opened in the Al-layer, which allow for local optical access to the semiconductor. The size of the holes is in the sub μm range. For light in the close infrared spectral region, these holes are nano-apertures with low optical transmission, since the wavelength in this case exceeds the aperture size. Propagation of the excitation light can take place only in the near-field optical limit. The 100 to 500 nm big holes work therefore as near field apertures for the excitation laser light. Therefore, the QD layer should be located near to the shadow mask. The sample, introduced here, uses QDs which are 320 nm under the surface. Together with the layers lying between shadow mask and semiconductor (20 nm), this near field condition is therefore well fulfilled. For the production of the shadow mask, an 80 nm thick aluminum layer was used. The near field apertures were defined by means of electron beam lithography and reactive ion etching.

For protection of the semiconductor from etching damages, a 15 nm thick Si_3N_4 stop layer is deposited under the aluminum layer, see figure 4.5 a). For PC measurements on individual QDs, further process steps are necessary, apart from the production of the shadow masks. This concerns the electrical contacts of the photodiode. In order to guarantee a homogeneous electrical field at the QD, a surface metalization of the sample is necessary, around the shadow mask area.

Figure 4.6 b) shows a top view of the sample with four active (bonded) photodiodes ($300{\cdot}400\ \mu m^2$). The bond contact is located on the titanium gold metalization. Within the aluminum metalization, one recognizes the shadow mask field, which contain the near field apertures. Figure 4.6 c) shows a series of 4 μm big markers, which form a U-shape around the apertures. During experiments, these markers turned out to be very helpful, in order to navigate on the sample and perform test measurements of a QD ensemble. Finally, the photo diodes are separated in $300\times400\ \mu m^2$ mesa structures by a further etching step.

The size of the near field apertures is compared with the average QD-distance in order to estimate the degree of the optical selection. With a density of the self organized InGaAs QDs of 100-200 μm^{-2} used, the distance between the QDs amounts, on average, to about 100 nm. Within a 300 nm large aperture, there should be nine QDs. Apart from this purely geometrical selection of the QDs by the shadow mask, the number of the QDs measured at the same time is limited furthermore due to the individual transition energy of each QD. With the help of the spectrally narrow excitation energy, only those QDs are addressed, which can absorb the selected energy. Due to the inhomogeneous ensemble broadening, one receives, for the single QD spectroscopy, sufficient energetic separation of the QD-absorption lines. Contrary to the optically selective excitation of individual QDs, the electrical access to the QDs is not selective. All QDs within the processed photo diode (about 12 million QDs in the $300{\cdot}400\text{-}\mu m^2$ large structure) are electrically contacted in parallel.

4.3 Detection

The detection method depends on the exciton decay mechanism. If the QD state is resonantly excited and the exciton is able to tunnel out of the QD, the detection takes place in the photocurrent. If the decay mechanism is an optical recombination process, the detection takes place in the photoluminescence. In this case, an GaAs-interband excitation is as possible as an excitation of a higher QD-state. The applied bias voltage controlls whether the tunneling process or the optical recombination process is dominant.

4.3.1 Photocurrent technique

In this section, the photocurrent (PC) spectroscopy on individual QDs is presented. The main advantage of this method is the high resolution as well as the direct coupling of the QD-states to electrical signals. Since detection in the PC spectroscopy takes places electrically, the ground state can also be investigated by resonant optical excitation.

The photocurrent mechanism is based on the principle of a resonant excitation of an individual QD. Therefore the isolation of an individual QD with near field a shadow mask (see chapter 4.2.3) is necessary. The single QD-states must be characterized and assigned before by voltage-dependent PL in order to receive the ground state energy. The resonant excitation must be tuned to the energy of the QD state. Then the QD can be excited and occupied with an exciton. After the excitation process, a tunnel process for both charge carriers can take place due to the applied voltage. After that, the QD is unoccupied and can be re-excited again. A measurable current results from this sequence of exciton generation and tunneling processes. The maximum current depends only on the repetition frequency of this sequence. A shorter life time and a faster re-occupation leads to higher currents. An applied voltage changes the tunneling probability of the charge carriers. An increase of the laser intensity leads to a faster re-occupation of the QD. The PC is affected by both parameters. If the QD is already excited, the laser can induce a stimulated emission. In the case of cw excitation, this leads to an equal occupation of the states for high laser intensities and thus to a saturation of the PC.

In case of pulsed excitation, generation and stimulated emission can follow up within one pulse. This leads to the RABI oscillations, as discussed in chapter 6.3. With appropriate electrical field strength, electron and hole are able to tunnel through the potential barrier. The electron and the hole are separated in the electrical field. Here the detectable photocurrent is determined by the repetition frequency of the laser system and the exciton occupation probability after the laser pulse interaction. Thus, the optical generated excitons are electrically detected with the help of simple DC current measurement.

An AlGaAs barrier is arranged in the intrinsic layer between the QDs and the front contact, see layer sequence in figure 4.5 a). In principle, this barrier could affect the transport of the tunneled holes to the front contact. An estimation of the ballistic transportation length of the holes shows, however, that the distance of 270 nm can be easily overcome. With a hole mobility of $\mu_h \propto 2 \cdot 10^4 \mathrm{cm}^2/\mathrm{Vs}$ a ballistic transport length of $\lambda_{bal} \cong 10\ \mu\mathrm{m}$ results at T = 10 K [TMT$^+$85] for heavy holes in the bulk semiconductor GaAs in the case of $F = 30$ kV/cm. This is much more than the distance between the QD layer and the front contact. Therefore a ballistic transport through the AlGaAs barrier should be easily

possible. At a temperature of 4.2 K, the thermionic emission from the QD is negligible. The thermionic influence on the QD state is a very interesting aspect, which is examined also in the group of Prof. ZRENNER.

The charge carriers generated in the QD are subject of investigations, depending on the examined states, outside conditions, and different decay processes, e.g. tunneling, relaxation or recombination. If one regards various absorption events, then the behavior of the charge carriers can be described statistically, with the help of the time constants of these processes. The optical recombination of the single exciton ground state takes place typically on a time scale up to 1 ns [OAO+96, BLH01]. In the case of resonant occupation of a higher excited QD state, a relaxation of the charge carriers takes place into the energetically lower lying state on a time scale in the ps range [OAO+96, HTK+02b]. To understand the PC spectra, these times must be compared to the tunneling time of the charge carriers. Contrary to the recombination and relaxation time, the tunneling time can be easily controlled by V_B. The tunnel barrier depends on the electrical field strength. The tunneling time can take values from less than 1 ps to more than 1 ns, and in principle become infinitely long. Please note that the tunnel time of electron and hole is different at the same electrical field. This is because of different effective masses. For tunneling times of $t \gg 1$ ns, optical recombination takes place before the exciton can tunnel out of the QD, so that the QD-absorption can no longer be detected in the PC measurement.

Photocurrent detection setup

The measurement of the PC signal is done by a time integrating DC measurement. Figure 4.7 shows the corresponding circuit. Between front and back contact of the QD-photodiode, a computer-controlled voltage is applied via a digital to analogue converter (DAC). The current flowing perpendicularly through the sample is measured at the same time by a current-voltage-converter (IVC). The PC signals can be in the range of 1 and 100 pA. The diode current flows into am OP-amp with 100 MΩ feedback-resistor, produces an amplification of 10^8 V/A, see figure 4.7. This signal is fed into an integrating analogue-digital converter (ADC). The resulting dynamic range extends from -5 to +5 nA with a resolution of 0.15 pA (16 bit).

- All components, which are in direct electrical contact with the sample (ADC, DAC, IVC) are implemented in a battery-operated housing with common electric ground.
- Communication with the computer is done via in a digital way fiber optics.
- In the sample holder, coaxial cables are used. All unshielded cables are as short as possible and if necessary twisted.
- Extremely low-noise units are used, the ADC provides an integration time of 50 ms.

Thus a current measurement with a stable ground potential becomes possible, which remains uninfluenced by potential fluctuations of normal net operated devices. The control and data exchange between the measuring computer and the voltage supply and/or the ADC takes place over optical data communication by means of optical fibers (broken

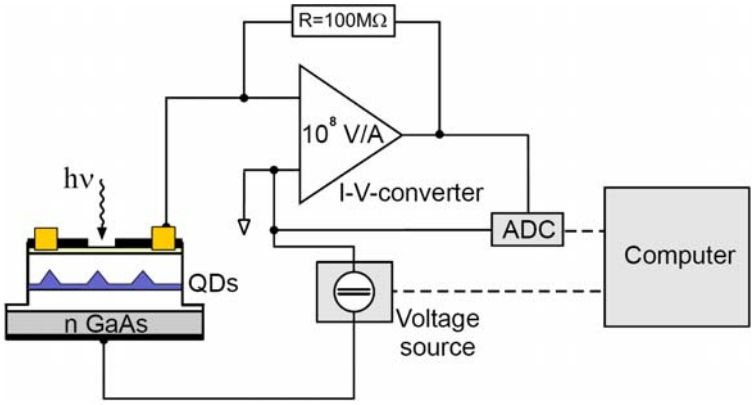

Figure 4.7: Photocurrent measurement setup. The resistance of 100 MΩ leads to a amplification of 10^8 V/A.

lines in figure 4.7). Thus a sensitive current measurement becomes possible at the sub-pA range, in a structure which is well protected from external influences. For the measurement of these very small currents, the IVC contains an operation amplifier, which features extremely low noise and very high input impedance.

The PC signal contains the dark current of the photodiode. The *n-i-* diode used has however a high blocking ability, so that the dark current does not play a large role. With the typical voltages used for the PC measurement, the diode dark current is in the sub pA range.

The ADC used has two similar input ports which are integrated at the same time. The first channel is used, as described, for the measurement of the sample current. The second channel converts a photodiode signal, which is proportional to the laser intensity at the sample holder (see figure 4.2). In intensity dependent measurements, this signal is used for the definition of the x-axis, while the PC of the sample defines the y-value.

4.3.2 Photoluminescence technique

The photoluminescence (PL) spectroscopy is a very sensitive method, in order to examine optical transitions in semiconductors. By excitation with photons of the energy $h\nu > E_{gap}$, electrons are lifted from the conduction band into the valence band. Pairs of electrons and holes are produced. The excited electrons and holes can recombine after a certain time. The resulting energy can thereby be released in different forms, as photons or less likely as phonons or also as AUGER electrons. In the PL spectroscopy, photons are detected which are emitted by a radiative recombination mechanism. Most PL-measurements are performed at low temperatures, in order to prevent thermal ionization and to avoid the broadening of the PL-lines by lattice vibrations (phonons). The luminescence of the InGaAs QDs which can be examined is reached by light excitation.

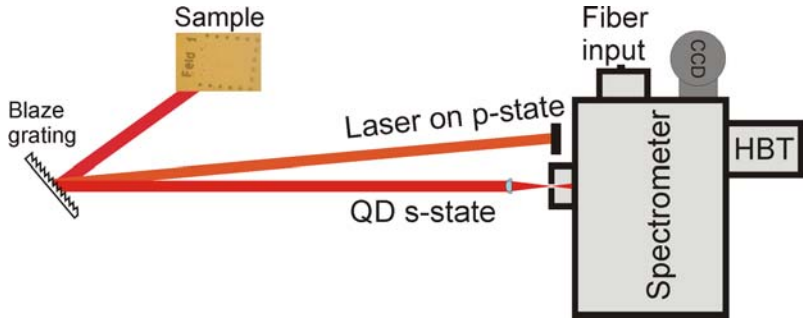

Figure 4.8: Detection setup for luminescence measurements with resonant excitation of higher QD-states. An extra grating is mounted before the spectrometer in order to separate laser and QD luminescence.

4.3.3 Photoluminescence excitation technique

Contrary to the normal PL, the photoluminescence excitation (PLE) method is sensitive to higher shells of the QD. In order to analyze higher QD shell-structure, the excitation energy is tuned continuously above the exciton ground state. If the laser energy matches a higher state of the QD, the exciton is directly generated in this state. After a relaxation process into the ground state, the exciton decays by optical recombination processes. The experimental setup must separate the (comparatively) weak photoluminescence intensity and the strong excitation before the detector. A single monochromator is not sufficient. If the laser gets into the monochromator, too much stray light will be generated. In order to suppress the stray light, an extra grating is mounted before the monochromator (see figure 4.8). Detection can be done with a Si-CCD camera or with the HANBURY-BROWN and TWISS setup at the second exit of the monochromator. The energy range which will be examined is between the single exciton ground state and the energy gap of the surrounding material. Similar to the PL, the PLE can be performed voltage, intensity and polarization dependent.

4.3.4 HANBURY-BROWN and TWISS setup

The proof of a single photon emission is done with the HANBURY-BROWN and TWISS (HBT) setup (figure 4.9). The luminescence of the single photon emitter must be spectrally filtered (suppression of the excitation laser) analogous to the PLE measurements, (see figure 4.8). The QD luminescence is collimated and directed on a 50:50 beam splitter cube. Both parts of the split luminescence are focused into optical fibers and directed on single photon counter units, here two similar avalanche photodiodes (APD). If a single photon is counted, an electrical pulse is generated and send to the TimeHarp 300 (Picoquant). The TimeHarp acts as a time to amplitude converter (TAC) which is able to display a histogram of correlation events with a maximum time resolution of 39 ps.

The histogram of a single photon emission under continuous and pulsed excitation is discussed in chapter 10. The proof of single photon emission can be shortly explained as follows. A single photon can not be transmitted and reflected at the same time in

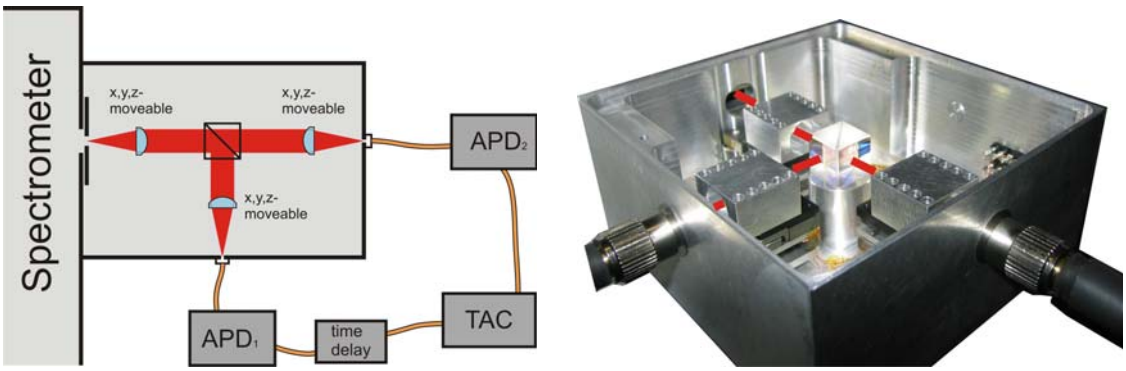

(a) Schematic view of the HBT

(b) Picture of the experimental realization

Figure 4.9: HANBURY-BROWN and TWISS setup for proof of single photon emission. A single incident photon cannot be transmitted and reflected at the same time. Thus, the histogram of the correlation events should show a clear reduction at zero time delay.

a beam splitter. It can only be detected at one APD. Therefore, the two APDs cannot count photons at the same time. If the luminescence only consists of single photons, the histogram of the TAC must show a clear reduction (dip) at zero time delay. In order to reach a symmetrical histogram, one electrical connection has an integrated time delay. This will only shift the measuring window to negative times.

One experimental detail should be discussed here. The APD emits a light flash at each single photon counting event. This effect was analyzed by the group of Prof. WEINFURTER ([KZMW01]). The light flash is called *avalanche breakdown flash*. The wavelength of this light flash overlaps with the range of the QD luminescence. It is therefore possible that the breakdown flash can be sent in backward direction to the sample. The light can be reflected on the sample surface and then be detected like a normal photon. Due to the spectral overlap, the photons from the QD and the photons from the APD cannot be distinguished. This can result in an additional structure in the histogram. The time constant of this structure corresponds to the optical path length from one APD to the sample and back. Another effect of the breakdown flash is the generation of background counts in the histogram. The reflected breakdown photons can initiate a correlation, not only with the photon which triggered the breakdown, but also with the QD photons.

5 Characterization of a single quantum dot

5.1 Optical properties

For sample characterization, PL spectroscopy is performed on every hole of the shadow mask. The PL signal exhibits different information about the sample. By non-resonant interband excitation (HeNe laser), the spectral distribution of the QD emission can be measured. A single QD contributes to the luminescence with more than one spectral line (e.g. charged states). The number of discrete peaks in the PL spectra is proportional to the number of QDs which contribute to the luminescence. The analysis of a single QD spectrum will be discussed in the following. In order to identify the different states of the QD, a voltage dependent PL series is performed.

Figure 5.1 shows a color plot of the voltage dependent PL of the best single QD spectrum of the sample. Here mainly the luminescence of a single QD is visible, but a small contribution of a second QD can be noticed at a slightly higher energy. All other holes of the shadow mask show the luminescence of more than one QD or no PL signal at all. One clearly notices three bright states which correspond to the main states of a QD.

Actually, only the lowest energetic state of the single QD should be visible at one time. But this is clearly not the case. This can be explained by the statistical process of the non-resonant excitation. The excited charge carriers relax into the QD. Additional to the luminescence of the neutral exciton, it is possible that only three charge carriers (one exciton and one further charge carrier) of a non-resonant interband excitation are relaxed into the QD. Then it is possible to observe the statistical luminescence of a charged QD. Therefore both emission peaks can be observed at the same voltage in this time integrated spectrum. Both states will probably not emit photons at the same time. Furthermore, it is possible that an extra electron can tunnel into the QD from the doped back contact at an adequate voltage.

This behavior is illustrated in figure 5.2. In case a), the applied voltage is high enough to lift the ground state over the quasi FERMI-level. Here it is not possible that electrons from the *n*-doped back contact can tunnel into the QD. In this region, only the luminescence of the neutral exciton (X) can be observed. For a slightly lower voltage, as shown in case b), the exciton ground state is equal to the quasi FERMI-energy. Electrons from the doped back contact are able to tunnel into the QD. The occupation of this state with an electron from the doped back contact takes place in the thermodynamic equilibrium. Here the luminescence of X and X^- can be observed. In case c), the applied voltage is low enough so that the ground state can be occupied with two electrons.

The first indicator for the state identification is the exciton-biexciton power dependence. At non-resonant interband excitation, the biexciton ($2X$) state can only contribute to the PL when the QD is occupied by two excitons. This is the case at higher excitation intensities. After the $2X$ recombination process, the charge carriers of the $1X$ state can

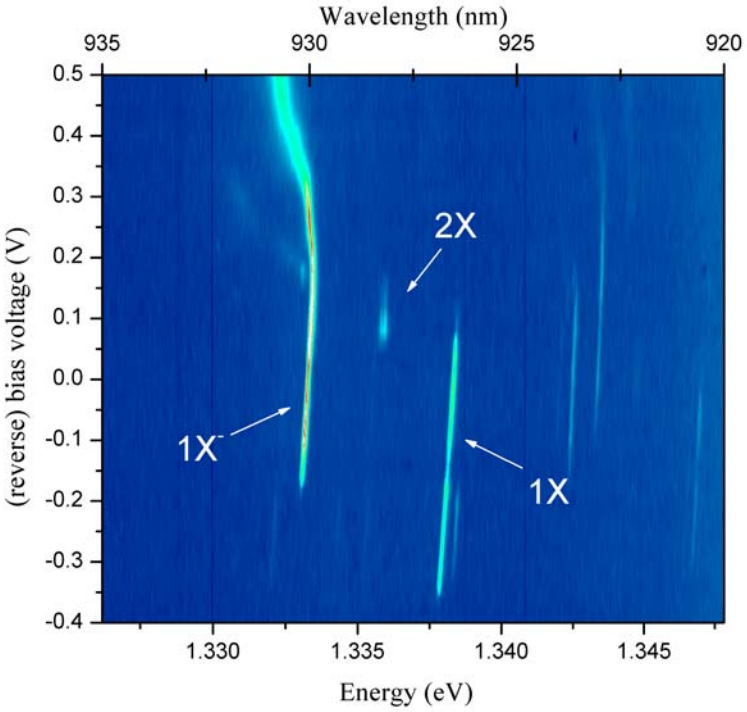

Figure 5.1: Voltage depending photoluminescence at non-resonant interband excitation. Marked are the three brightest states, the single neutral charged exciton X, the single negative charged exciton X^- and the biexciton $2X$.

recombine after a characteristic time (radiative recombination time), or a further absorption process leads again to the occupation of the $2X$ state. For low excitation intensities, only the $1X$ state can contribute to the luminescence. But the PL of the X will saturate with increasing excitation intensity. Simultaneously the PL intensity of the $2X$ state will increase.

Thus, the neutral exciton can be identified. The luminescence of the $1X$ state can be observed in the voltage range of -0.35 V to 0.05 V. Below -0.35 V, the luminescence will vanish due to a higher tunneling probability for the charge carriers. At a voltage of about -0.2 V, the quasi FERMI-levels of the single exciton ground state and the n^+ GaAs back contact line up. At non-resonant excitation, the luminescence of the single negative charged exciton (X^-) can be observed. The slight higher intensity of the X^- state (compared to the $1X$ state) can be explained by the high tunneling probability of electrons from the doped back contact into the QD and the statistical occupation with a charged exciton (explained above). This state is separated by ≈ 5 meV (corresponds to 3.5 nm in wavelength) from the ground state. The strong broadening of the X^- state at a voltage of >0.2 V can be observed in the luminescence. The line broadening and shift in energy is

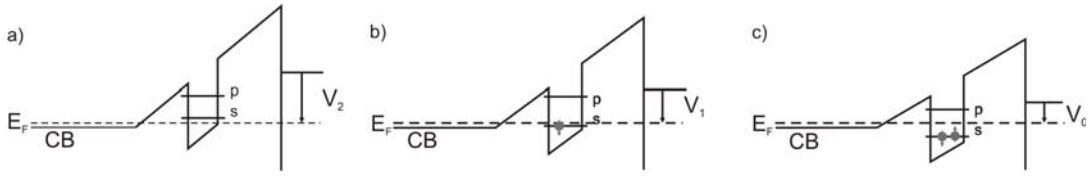

Figure 5.2: Band structure at different applied voltages. a) The applied voltage is high enough to lift the ground state over the FERMI-energy. b) The exciton ground state is in the region of the FERMI-energy. Electrons from the doped back contact are able to tunnel into the QD. c) The applied voltage is low enough that the ground state can be occupied with two electrons.

probably an influence of charged wetting layer states to the QD.

The power- and the voltage dependences are the main indicators for the state identification. The identification of multiexcitonic states is of course more difficult. The weak state (at V < -0.18 V) has a slightly higher energy as the single exciton ground state. This state could be tentatively assigned to the last charged *s*-shell transition, the positive charged exciton X^+. This assignment is supported by the fact that the state vanishes at the same voltage as electrons from the back contact can tunnel into the QD. Due to the fact that holes are not able to tunnel into the QD, this state can be generated by a confinement of an exciton and an extra hole of a non-resonant optical excitation.

But it is also possible that each measured peak of the PL consists of a fine structure which cannot be resolved with this PL-setup. The fine structure splitting and the linewidth of the *X* state can be analyzed with PC spectroscopy (in the voltage region of the PC). The transition energies show a slight red shift with increasing (reverse) bias voltage. This results from the quantum confined STARK effect (QCSE). The QCSE affects the exciton-states in the PL region as well as in the PC region.

5.2 Quantum confined STARK effect

For PC measurements, the excitation setup has to be changed to the tunable TiSa laser system. The laser energy must be tuned to a slightly lower energy (due to the QCSE) than the measured PL energy. The energy of the ground state can be tuned via the bias voltage. If the fixed laser energy fits to the transition energy, an absorption process can take place. The excited charge carriers are able to tunnel out of the QD and generate a current if the applied (reverse) voltage is high enough. Therefore the absorption characteristics appear in the photo- *I*-*V*-characteristics of the *n*-*i*-SCHOTTKY-diode. The behavior of the QD with varying different parameters like excitation intensity, excitation polarization and applied voltage can be investigated. For the basic characterization, the influence of the applied voltage on the transition energy (and the tunneling time) is important.

In this section, the influence of an electrical field (F) in the z- (growth-) direction is discussed. The x and y directions are irrelevant in the first approximation and neglected here. The description takes places analogous to a quantum well. As mentioned before, only the lowest quantized energy state in z-direction is examined. In an electric field, the

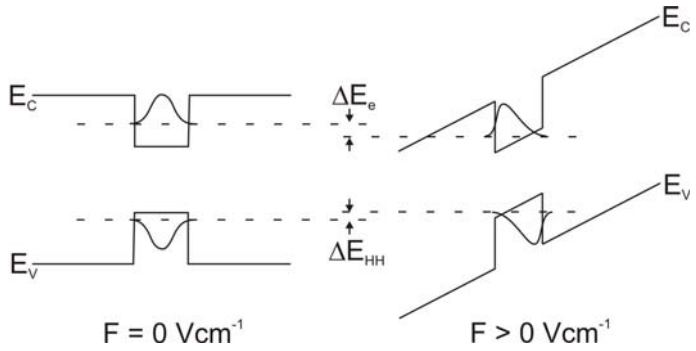

Figure 5.3: Schematic view of the quantum confined STARK effect. left: flat band conditions; right: high applied electric field. (from [BZF+01])

wave functions of electrons and holes in a QD are shifted and slightly deformed. Figure 5.3 shows a schematic sketch of the wave functions with and without an applied electrical field. The deformation results in an induced dipole moment μ which reduces the transition energy in an electric field of $\Delta E = \mu F$. The decrease of the energy is quadratic with increasing electrical field. For high electrical fields, the shift of the dipole moment is limited by the size of the QD. Therefore the energy shift is almost linear for higher electric fields. This is only a coarse approximation, which however correctly reflects the behavior of the quantum confined STARK effect (QCSE). For an exact description, the reduction of the COULOMB-interaction (due to a reduced electron hole distance) and the change of the quantization energy have to be taken into account. The shift of the electron and hole wave functions into different directions reduces the overlap and therefore the transition matrix element. The QSCE allows for a very accurate tuning of the transition energy. The tuning range is relatively small (some meV), but the adjustment fidelity only depends on the stability of the voltage source [HSK+04, SEZB04].

Up to a reverse voltage of about 0.4 V, optical recombination processes are dominating. Here the QCSE can be observed in the PL, see figure 5.4. At higher voltages, the tunneling probability increases. The energy of the X transition can then be measured in the PC. Figure 5.4 shows the QSCE, which continuously covers the whole PL and PC region. An example of a PC resonance is displayed in the inset (upper right) of figure 5.4. The shape of the resonances and the voltage dependence is discussed in chapter 6.2. The PL measurements are performed at non-resonant interband excitation. The PC measurements work with resonant excitation and electrical detection. The insets in the figure show the different processes. The conversion from voltage into energy scales is a result from the fit curve, see figure 5.4:

$$E = 1.33833\,\mathrm{eV} - 0.00121\,\frac{\mathrm{eV}}{\mathrm{V}} \cdot V_B - 5.81615 \cdot 10^{-4}\,\frac{\mathrm{eV}}{\mathrm{V}^2} \cdot V_B^2 \tag{5.1}$$

More important than the absolute energy is the relative energy variation ΔE at the tuning

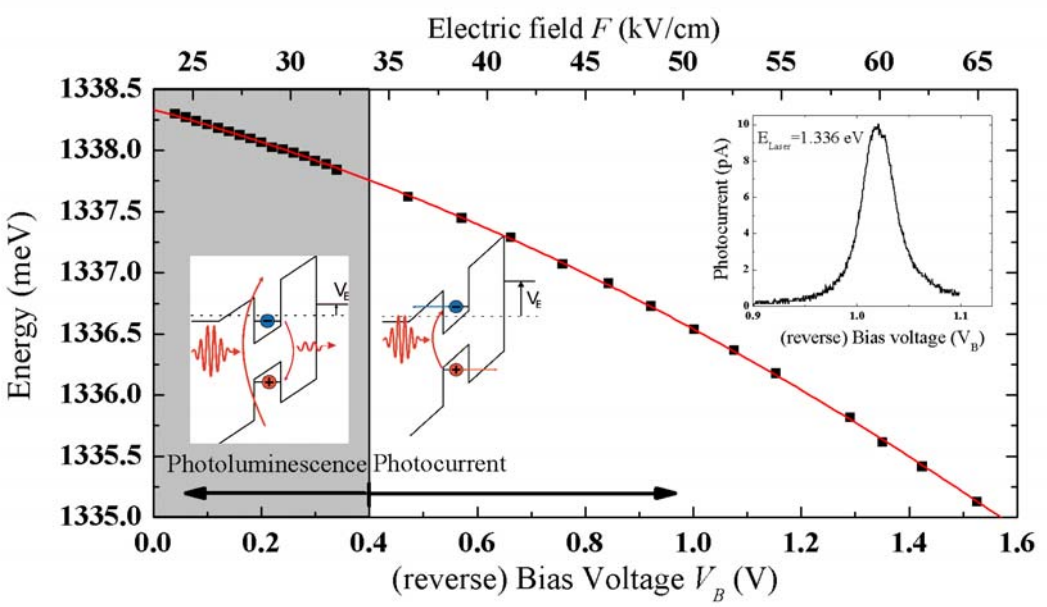

Figure 5.4: Quantum confined STARK shift of the single exciton ground state. The energy shift covers the whole PL (<0.4 V) and PC region (>0.4 V). (published in [SEZ06])

of the QD energy levels via bias voltage. This variation of energy is given in μeV:

$$\Delta E = \left(-1210 \pm 17 \, \frac{\mu\text{eV}}{\text{V}} - 1163 \pm 26 \, \frac{\mu\text{eV}}{\text{V}^2} \cdot V_B \right) \cdot \Delta V_B \tag{5.2}$$

The energy of the QD transition decreases with increasing reverse voltage V_B.

5.3 Photoluminescence excitation spectroscopy

Since the spectral position of higher excited states of the QD are not visible with the normal PL technique, a photoluminescence-excitation (PLE) experiment has to be performed. The spectral position of the *p*-shell has, of course, to be known for all further investigations, e.g. analysis of the relaxation behavior or for coherent manipulations. For excitation a tunable Ti:Sa laser is used, which is tuned here in the region of 10 to 50 meV above the ground state.

Figure 5.5 shows the PLE spectrum of the investigated QD. Of course, the PLE spectrum strongly depends on the applied conditions, such as voltage and excitation intensity. The behavior of a QD under an applied voltage is discussed in chapter 7. Very high excitation intensity could lead to unwanted off resonant excitation of the QD. Therefore, zero applied voltage and an excitation intensity of approximately 4 μW at the sample are chosen. Furthermore, one has to be sure that the excitation intensity is constant over the whole tuning range.

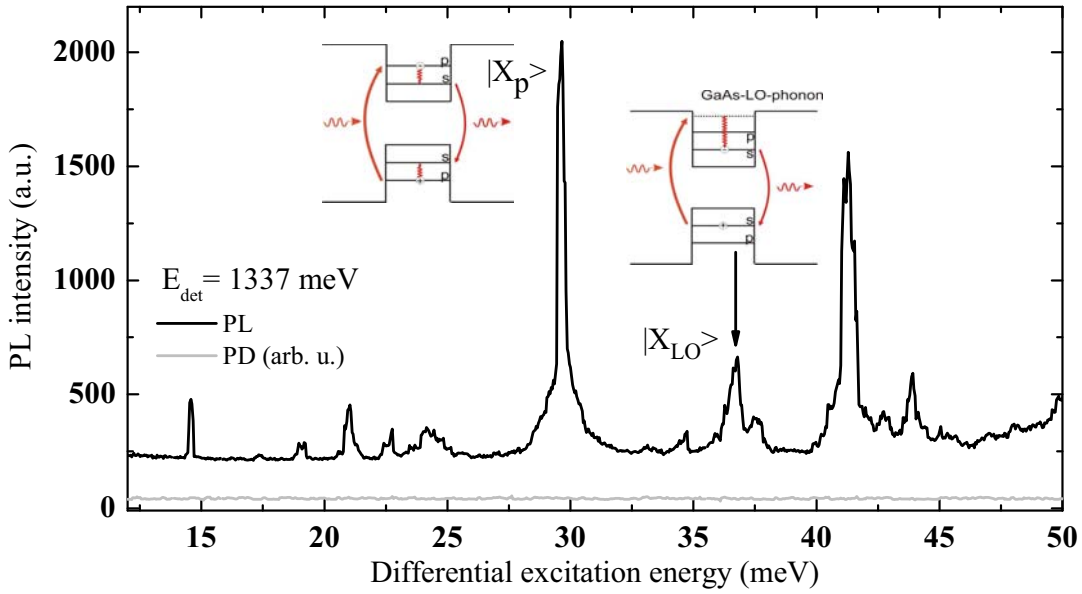

Figure 5.5: PLE-spectrum of the single exciton ground state. The energy is displayed with respect to the QD ground state. The strongest peak at 29 meV is assigned to the p-shell absorption ($|X_p\rangle$) and the resonances around 36.7 meV correspond to (LO) phonon assisted absorption ($|X_{LO}\rangle$). The PD-signal shows stable excitation intensity in the whole range. Inset left: The laser excites the QD in the p-shell. After the relaxation process the exciton recombines in the s-shell. Inset right: LO-phonon assisted absorption. The laser generates the exciton direct in the ground state with a simultaneous generation of GaAs-LO phonons. (published in [ELdV$^+$07b, ELdV$^+$07a])

The spectrum shows two main resonances. The largest peak at 29 meV above the ground state ($E_{GS} = 1.337$ eV) is assigned to the p-state ($|X_p\rangle$) and the second largest peak (42 meV) is found to be the next excited state (probably the d-shell). The small peaks around 36.7 meV are assigned to GaAs phonon-assisted absorptions ($|X_{LO}\rangle$). The phonon assisted absorption matches the GaAs LO phonon energy very well. The results of these PLE measurements are comparable to the results reported in [FZBA00]. The much weaker resonance around 33 meV above the ground state can be tentatively assigned to an InAs phonon mode, which where also observed in ensemble PLE experiments in reference [HVL$^+$97]. The insets in figure 5.5 illustrate the different excitation schemes for p-shell excitation and LO-phonon assisted absorption. In the left case, the excitation energy fits to the p-state. After the absorption process, the exciton relaxes into the ground state, probably by emitting acoustic phonons. After the relaxation process, the exciton decays due to an optical recombination. In the left case, the excitation energy fits to the ground state energy plus the energy of a GaAs-LO phonon. The ground state is thereby generated with the help of an emitted GaAs-LO phonon. The ground state is again able to decay by optical recombination.

6 Single exciton ground state

6.1 High resolution absorption spectroscopy

The linewidth of a QD ground state transition at low temperatures is very small and hardly resolvable with optical techniques. If one analyzes the QD ground state optically, the resolution of the detection setup must be higher than the linewidth of the emission. It is simpler to analyze the absorption properties instead of the emission properties. Therefore, one has to use a very narrow linewidth (laser) for excitation. This is quite easy with the use of a TiSa laser in its continuous wave mode. Due to the integration of the QD into a diode structure, it is possible to shift the QD energy over the laser energy by means of the STARK effect. There are two options for the detection of the ground state resonances. One can analyze the transmitted laser intensity or detect the generated charge carriers in the photocurrent. When the transmitted laser photons are detected, an AC voltage is applied at the QD. The detection intensity is then plotted as a function of the applied voltage in a histogram. The diagram shows a very small dip (only a decrease of 10^{-5}) when a QD ground state absorbs the incident photon. But the resolution is very high because only the laser line width determines the resolution. A disadvantage of these measurements is the comparatively long integration time [SLG+02]. The other option (photocurrent detection) is used here in order to analyze the QD ground state. The use of the STARK effect for the energy tuning sets the lower limit for the resolution of the measurement setup. The use of a 16 Bit DAC results in an increment of 0,3 μeV. Therefore every linewidth larger than approximately one μeV appears not broadened due to the experimental setup. Thus, the increment of the used DAC has no influence on the measured linewidth. The measured linewidth in the photocurrent is a result of a convolution of the incident laser linewidth and the QD ground state. For a very narrow laser linewidth, the resulting signal is mainly determined by the QD-state.

Due to the fact that the measured spectra are not influenced (broadened) by the experimental setup and the detection efficiency in the photocurrent is almost perfect (100%), all measured criteria can be referred back to basic effects of the quantum system. In a closed circuit, no charge carriers (electrons) could be lost. Every charge carrier which is tunneled out of the QD contributes to the photocurrent. Only excitons which recombine optically (after the optical life time) cannot be detected. The detection limit for the current is determined by the PC pre-amplifier and the used ADC, see chapter 4.3.1. The occupation of the upper state of this two level system can be described with a rate equation (see chapter 3.5.1). For tunneling times longer than the radiative lifetime, the decay of the ground state is mainly determined by the optical recombination process. Thus the lower limit for PC measurements is determined by the optical recombination time (approximately 500 ps). The PC pre-amplifier must be selected suitable to detect these low currents. A tunneling time of one ns results in a PC of 1 pA, which can be detected with

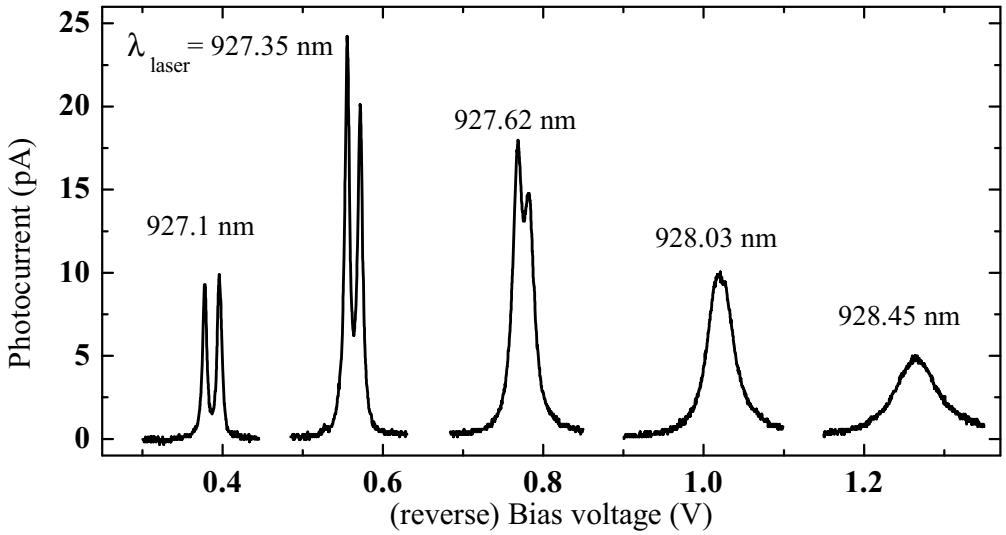

Figure 6.1: Photocurrent resonances of the single exciton ground state transition at different excitation wavelengths. At low voltages, one can observe the fine structure splitting (resulting from the QD asymmetry). At higher voltages, the line width is broadened due to a reduced tunneling times and thus covers up the fine structure slitting. (published in [SEZB04, ESdV+06a, ZSE+06, KSS+05])

the used setup.

Figure 6.1 shows photocurrent resonances of the single exciton ground state transition. Each spectrum is measured at fixed laser energy and a varying bias voltage. If the laser energy is tuned to a slightly lower energy, the resonance is shifted to a higher voltage.

- The resonances become broadened at higher voltages. A higher voltage induces a higher tunneling probability and a shorter life time.

- At low voltages, a double resonance can be clearly observed. This is an effect of the asymmetry of the QD, which is called *fine structure splitting*.

- The integral intensity of the absorption line is constant for voltages higher than 0,4 V.

- The absorption resonance of the ground state cannot be shifted into the region of the photoluminescence. The resonance at 0,4 V is located in the transition region between the photoluminescence and the photocurrent. Therefore the PC amplitude is reduced.

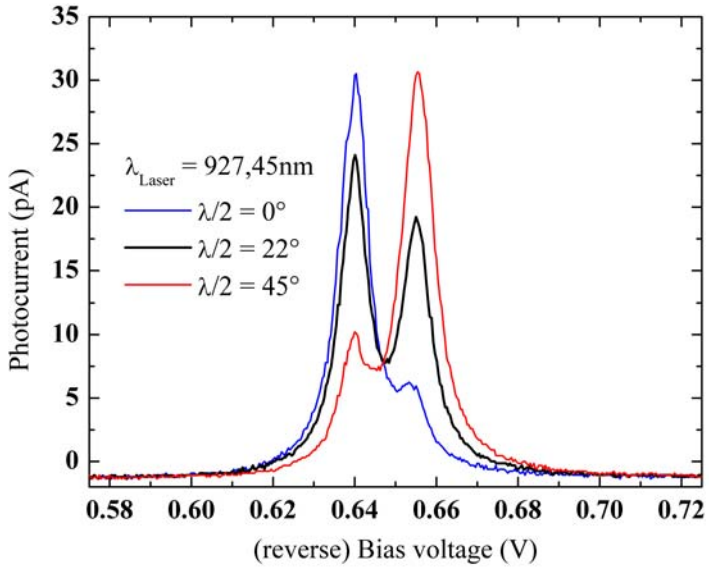

Figure 6.2: Fine structure splitting of the single exciton ground state analyzed by different linear excitation polarization. The fine structure splitting arises due to the asymmetry of the QD. Each line can be clearly suppressed with respect to the other.

6.2 Ground state properties at continuous excitation

6.2.1 Fine structure splitting

In figures 6.1 and 6.2, one can clearly see the fine structure splitting of the single exciton ground state (double absorption line). As mentioned before, the STARK effect allows for a conversion of the voltage into an energy scale. Thereby the fine structure splitting corresponds to an energy splitting of 30 μeV. This is caused by a slight asymmetry of the QD concerning different crystal directions. One can see in figure 6.2 that each absorption line can be clearly suppressed with respect to the other by an excitation with linear polarized laser ([110] or [1$\bar{1}$0] direction). A complete suppression is possible by using a slight elliptical polarized excitation.

The polarization dependence of the resonances also remains by changing the excitation to the pulsed mode. This is shown in double pulse experiments, where the fine structure splitting leads to a quantum beating (see chapter 6.4.1). At low bias voltages, it is possible to address only one single resonance, but for higher voltages the two resonances cannot be fully distinguished. At higher voltages (0.8 V), one always gets a mixing of both states, which always leads to a quantum beat behavior.

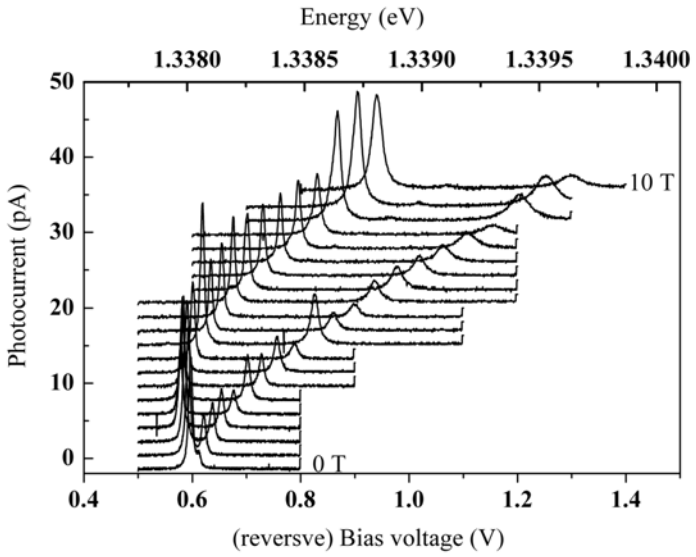

Figure 6.3: ZEEMANN splitting of the single exciton ground state. The fine structure splitting (30 μeV at B = 0 T) increases with increasing magnetic field to a Zeeman splitting of 0.85 meV at B = 10 T).

6.2.2 ZEEMAN splitting

In the previous section, the influence of an applied electric field was discussed. Not only an electrical field, but also an applied magnetic field affects the states of the single QD. Figure 6.3 shows 21 different characteristic curves of the QD measured at different magnetic fields from zero to ten Tesla (0.5 T step width). All measurements are performed at 4.2 K. The laser wavelength was fixed during this measurement. One can clearly see that the splitting of the ground state increases with higher magnetic fields. The tunneling processes of the charge carriers are in first order not affected by the magnetic field. The normal fine structure splitting was determined to 30 μeV without magnetic field. The splitting increases to 0.85 meV at a field of 10 T as a result of the ZEEMAN interaction. The linewidth of the two resonances is normally broadened by the applied voltages and not further affected by the magnetic field. Please note that the variation of peak heights (at different magnetic fields) has no physical origin. The magnetic field slightly moves the sample holder and the laser focus with respect to the QD position. The focus of the objective must be re-adjusted at each magnetic-field setting. Thereby a slightly different adjustment could lead to a different maximum peak height. The spectral position of the two resonances is not affected by the displacement of the sample holder. Due to the high resolution of the photocurrent technique, the energy of the two transitions can be clearly determined with an increasing magnetic field. The magnetic splitting of the ground state measured in the PL was shown before [BKF$^+$99].

Figure 6.4 shows the spectral position of the two resonances depending on the applied magnetic field. One can observe a clear quadratic dependence of the state energy with

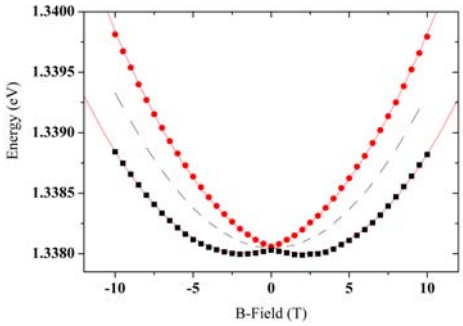

(a) Energy of the fine structure levels with increasing magnetic field. One can see an anticrossing of the levels at 0 T.

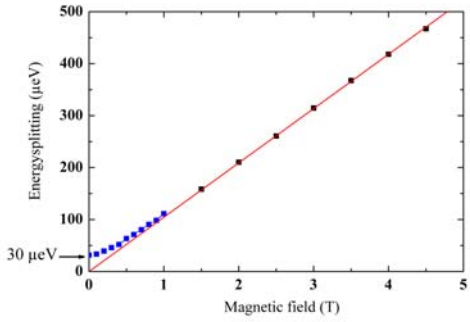

(b) Energy splitting with increasing magnetic field. For low fields the normal fine structure splitting is dominant, but for higher magnetic fields the splitting increases linear.

Figure 6.4: ZEEMANN splitting with increasing magnetic field.

increasing magnetic field. The magnetic field dependence of the transition energy results from the diamagnetic shift of the exciton plus the ZEEMAN energy. The interaction of the exciton spin with B-filed depends on the spin orientation. In strongly confined QDs, the exciton diamagnetic shift is determined by the single particle wave functions and is independent of the exciton spin orientation. The different B dependences of the photocurrent resonances therefore result from their ZEEMAN splitting. Therefore, the behavior can be well described by a square dependence on the magnetic field.

The (heavy hole) exciton is fourfold degenerate at zero magnetic field. The exciton states are characterized by the total angular momentum m along the z direction, $m = S_{e,z} \pm J_{h,z}$ with the electron spin $S_{e,z} = \pm 1/2$ and the hole spin $J_{h,z} = \pm 3/2$. The states with the total angular momentum of $m = \pm 1$ are called bright excitons ($m = \pm 2$ are called dark excitons). In this measurement, one can only observe (even at high magnetic fields) the bright excitons. The luminescence of dark excitons in high magnetic field measurements in a QD ensemble is reported by M. BAYER in [BKF+99]. Here, the dark exciton could be observed at higher excitation intensities and other magnetic field geometries.

The breaking of the quantum dot symmetry by a magnetic field can be tested by tilting the magnetic field out of the [001] direction. The magneto-PL experiments (in the so-called VOIGT configuration) is also discussed by M. BAYER in [BOS+02] for varying magnetic-field strengths. At B = 0 T, a single emission line corresponding to emission from the $|M| = \pm 1$ excitons was observed. On its low-energy side an additional spectral line appears at B = 2 T which originates from the $|M| = \pm 2$ excitons (dark-exciton) at zero field. For higher fields each of the two emission lines splits into a doublet. The energy splitting between them increases with increasing B.

The field dependence of the splitting between the two states is given by

$$\Delta E = \sqrt{(g_e + g_h)^2 \mu_B^2 B^2 + E_{as}^2}$$

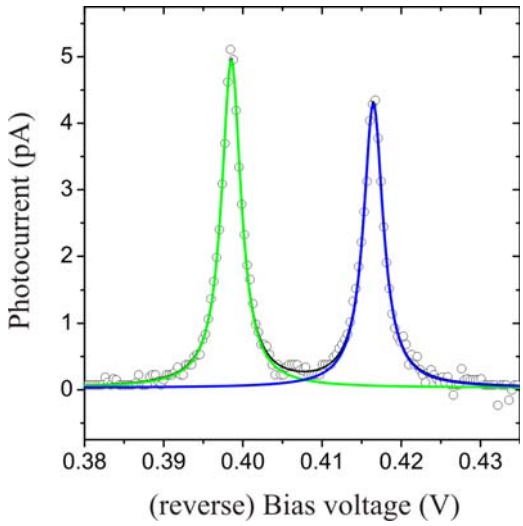

Figure 6.5: Comparison of measured line width (open circles) and lorenzian fit curve.

where g_e and g_h respectively correspond to the electron and hole g factor (formula taken from [BKF+99]). E_{as} refers to the asymmetry (fine structure) splitting. At low magnetic fields, the splitting increases quadratically, and then transforms into a linear dependence (in magnetic field). The crossover occurs at rather small magnetic fields of about 1 T, because the ZEEMAN energy then becomes considerably larger than the asymmetry splitting. This behavior can be clearly seen in figure 6.4 b), where the energy splitting at low magnetic field is only determined by the asymmetry splitting. By analyzing the resonances even at negative magnetic fields, one can see that the two states perform an anticrossing with a minimum energy splitting which corresponds to the asymmetry energy. A fit of the splitting as a function of the magnetic field (in the linear regime) leads to a ZEEMAN splitting of 99.47 μeV/T. Therefore the absolute value of the sum of the electron and hole g-factor is about 1.72 ± 0.01. Here it is not possible to determine the underlying electron and hole g-factors separately. The dashed line in figure 6.4 a) corresponds to the mean value (diamagnetic shift) of both states.

6.2.3 Photocurrent saturation of a single quantum system

In this section, the behavior of the QD for increasing laser excitation is discussed. Figure 6.5 shows a measured fine structure splitting and a LORENZ-fit curve. As it can be seen, the fit curve matches the measured fine structure line shapes very well. For further analysis the linewidth of the fit curve, the peak height and the peak position are taken from those fit curves. Figure 6.6 shows different spectra of the fine structure splitting with increasing excitation intensity. One can clearly see that the resonances are broadened up to higher excitation intensity. For low intensities, both resonances are clearly separated (30 μeV). But for higher intensities, the two peaks have a clear overlap. For the analysis of the saturation, the peak heights of the fit curves are displayed over the excitation intensity. The occupation of the single exciton ground state shows a clear saturation

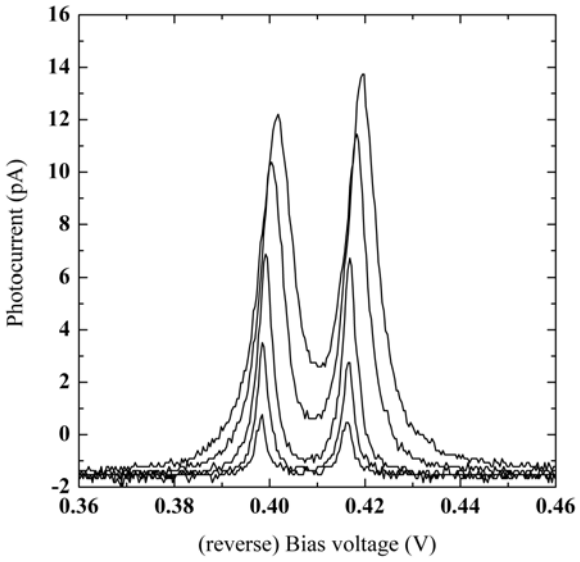

Figure 6.6: Fine structure resonances with increasing excitation intensity. A clear broadening of the resonances can be observed. (published in [SEZB04, ESdV+06a])

behavior.

$$I = N_1 \frac{e}{\tau_{tunnel}}$$

where e is the elementary charge, N_1 is th upper state occupation probability, and τ_{tunnel} is the tunneling time of the state.

The saturation behavior for continuous excitation can be written as:

$$I = I_{Sat} \frac{\widetilde{P}}{\widetilde{P}+1}$$

with

$$I_{Sat} = \frac{e}{2\tau_{tunnel}}.$$

Figure 6.7 shows the comparison between PC peak height and the fit curve. One can observe a very good agreement between measurements and fit curve. Please note that the applied voltage of 0.4 V is in the region between the photoluminescence and the photocurrent. Therefore the tunneling time should be in the region of the optical recombination time. The analysis of the fit parameters results in a tunneling time of 5,3 ns. The normalized excitation intensity $\widetilde{P} = 1$ corresponds to an intensity of only 35 nW at the sample.

The tunneling time of 5.3 ns is not in contrast to the optical recombination time of

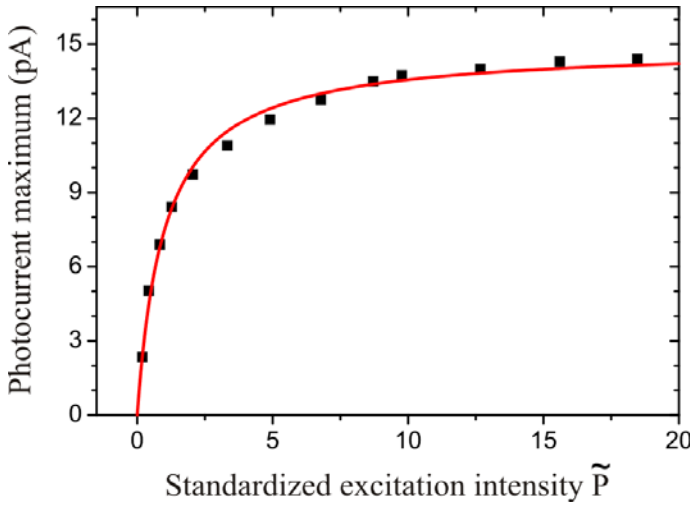

Figure 6.7: Saturation of the single exciton ground state at a bias voltage of 0.4 V. The peak heights of the fit curves (square points) are displayed over normalized excitation intensity. The fit curve is taken from formula 6.2.3. (published in [SEZB04, ESdV+06a, ZSE+06, KSS+05])

about 500 ps. The exciton consists of two charge carriers, the electron and the hole. It is plausible to think that both charge carriers have a different effective masses, different confinement potentials and therefore also different tunneling times. The saturation value is only determined by the tunneling time of the slower charge carrier, which is probably the hole. The initial state (empty dot) is reached when both charge carriers are tunneled out of the dot. Therefore the slower tunneling time determines the saturation value. The energy level of the QD in the presence of an extra hole is separated well enough from the laser energy, so that no further absorption can take place. Thus, further absorption can only take place when the QD is again in the initial state.

The power dependence of the peaks heights corresponds well to the theoretical model. Even at low bias voltages, a saturation can be observed for very low excitation intensities (<100 nW). Other measurements with higher bias voltages lead to the same qualitative behavior. A higher voltage leads to shorter tunneling time for both charge carriers and therefore to higher saturation value (37 pA at 0.5 V and 75 pA at 0.58 V). A good overview of the saturation behavior which includes the theoretical description of the rate equations can be found in [BZF+01].

6.2.4 Power broadening

The effect of the excitation power induced broadening of the absorption linewidth has been known for a long time from atomic optics. The observation of the *power broadening* in a single QD requires a very high resolution of the experimental setup. The technique of the photocurrent spectroscopy allows for a very detailed observation of the power induced line broadening.

As theoretically discussed in chapter 3.5.2, one expects a broadening of the absorption

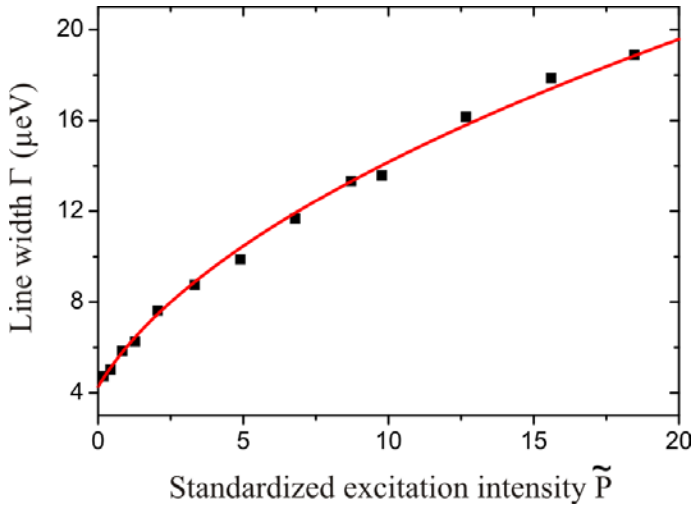

Figure 6.8: Broadening of the absorption linewidth with increasing excitation intensity. The only free parameter for the fit curve here is the y-axis segment. Due to the very good agreement from the measurement and the fit curve it is guaranteed that no other line broadening effects are relevant here. (published in [SEZB04, ESdV+06a, ZSE+06, KSS+05])

linewidth as a direct consequence from the saturation with: $\Gamma = \Gamma_0\sqrt{1+\widetilde{P}}$ (Formula 3.37). Figure 6.8 shows measurements of the absorption line of the same state for increasing excitation amplitudes. The data which is analyzed here, corresponds to the same set of data as used for the saturation analysis (see figure 6.7). The full line is the theoretical fitcurve. The very good agreement between the measurement and the theoretical fitcurve is obvious. The scaling of the x-axis is taken from the figure 6.7. The only free parameter for the fitcurve here is the y-axis-value (at $\widetilde{P} = 0$). This value corresponds to the linewidth for vanishing excitation power Γ_0. The increase of the fitcurve is determined by formula 3.37, because the conversion of the laser power into the normalized excitation power $\widetilde{P}$ is identical to the analysis of the saturation.

Due to the fact that the measured linewidth matches extremely well the fitcurve, it can be concluded that the line broadening is only determined by the saturation. Thereby all other possible line broadening mechanisms can be neglected. One can see in figure 6.8 that the power induced saturation broadening can cause a significant increase in the linewidth. Compared to the linewidth for vanishing excitation power Γ_0, a power of about 100 nW results in a doubling of the linewidth. Thus, it is possible that details of a resonance (e.g. a fine structure splitting) can be washed out by applying too high excitation intensity. The theory, which is described in chapter 3.5.2, only includes the line broadening effect of the saturation, a dephasing effect is not included. In order to determine the dephasing time T_2 from the linewidth, one has to take the saturation broadening into account. For the correct determination of this value, one has to extrapolate the linewidth to vanishing excitation power. This method is used in figure 6.16 for the determination of the T_2-times of the quantum system resulting from the linewidth.

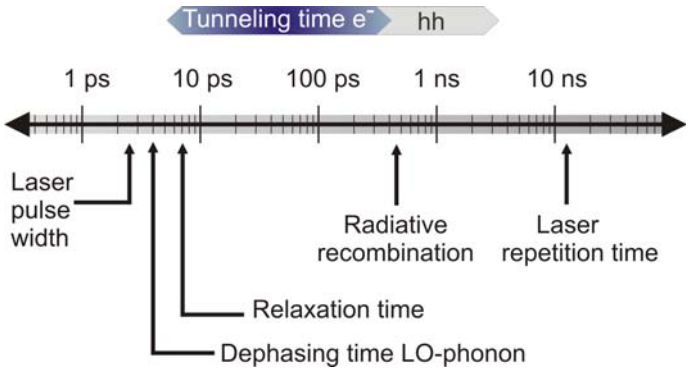

Figure 6.9: Relevant timescales for coherent control experiments in the photocurrent. The tunneling time of both charge carriers strongly depend on the applied voltage. The tunneling time of the electron is longer than the pulse length (adjusted by the voltage). The hole tunneling time is comparatively long, but shorter than the laser repetition time.

6.3 Coherent properties

In the case of continuous wave excitation, it is only possible to occupy the QD with a statistical probability of 0.5. The use of pulsed excitation allows for a defined state preparation of the two level system within a single interaction. The fundamental effect in the coherent regime is the RABI-oscillation. The occupation of the two-level system is thereby measured depending on the incident pulse area [1]. With increasing excitation intensity, an oscillation behavior of the occupancy can be observed. The physical content of this effect is fairly easy. At low excitation intensities, it is possible to excite the two level system. The excitation probability is proportional to the square of the pulse area in the low intensity regime. If the excitation intensity increases, it is possible that stimulated emission follows the excitation within one pulse. Therefore the measured signal will oscillate (with increasing excitation intensity) between the two extremes 0 (no exciton generated) and 1 (every pulse generates an exciton). In recent years, a lot of works have been published concerning coherent experiments on semiconductor QDs [SLS+01a, KGT+01, HTK+02a, ZBS+02, BLS+02, BBM03, MWB+04, WMB+05, UML+05, PLW05].

6.3.1 RABI-oscillations

The theoretical description of the RABI-oscillations is discussed in chapter 3, here the experimental results are presented. The pulse area (or the rotation angle on the BLOCH sphere) is adjusted by the attenuation of the laser field amplitude. The RABI-oscillations are affected by the amplitude of the exciting laser field, which corresponds to a quadratic dependence of the RABI-oscillations from the laser power.

For coherent control experiments, one has to take some important time scales into account. It must be guaranteed that each laser pulse interacts with the QD in its initial state.

[1] The pulse area is the result of the integration of the laser field amplitude during a single pulse.

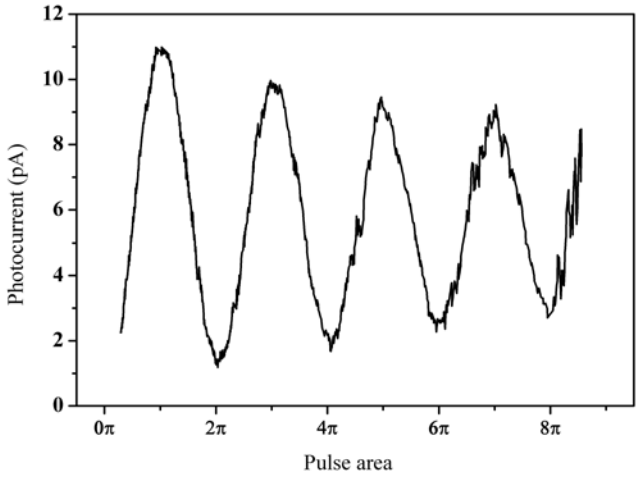

Figure 6.10: RABI-oscillations of a single exciton ground state. The photocurrent measured is directly proportional to the occupancy of the two level system. The signal shows a very periodical oscillation with a very slight damping of the signal (background corrected). (published in [SEZB05, ZSE+06, KSS+05])

That means the repetition time period of the laser must be longer than any fundamental process in the QD. In the case of coherent control of the single exciton ground state, the laser repetition time has to be longer than the radiative recombination time. On the other side, a low repetition frequency leads to a low current, see formula 6.1. Additionally, the performance of the coherent control is only good when the coherence of the QD is maintained during the interaction. The fastest dephasing process is, in the case of the coherent ground state control, the tunneling process of the electron. Both tunneling processes (electron and hole) are strongly dependent on the applied voltage and range from 10 ps to 300 ps (electron), which is longer than the used laser pulse width (2 to 4 ps). The slowest tunneling process is in any case faster than the repetition period of the laser. Therefore each laser pulse interacts with the QD in its initial state. In the case of pulsed excitation, any generated exciton is able to tunnel out of the QD (in the PC regime). Every tunnel process contributes to the PC with one elementary charge. The maximum current is thereby defined by the laser repetition frequency and the elementary charge [ZBS+02].

$$I = P_{1X} \cdot f_{Laser} \cdot e \tag{6.1}$$

f_{Laser} corresponds to the laser repetition frequency, and P_{1X} to the occupation probability. This maximum value (12.8 ps for f_{laser} = 80 MHz) can only be reached if no dephasing process takes place during the interaction, for example optical recombination in the transition regime of photocurrent and photoluminescence.

Figure 6.10 displays the RABI-oscillation of the single exciton ground state (photocurrent versus excitation pulse area). This measurement is performed at a voltage of about

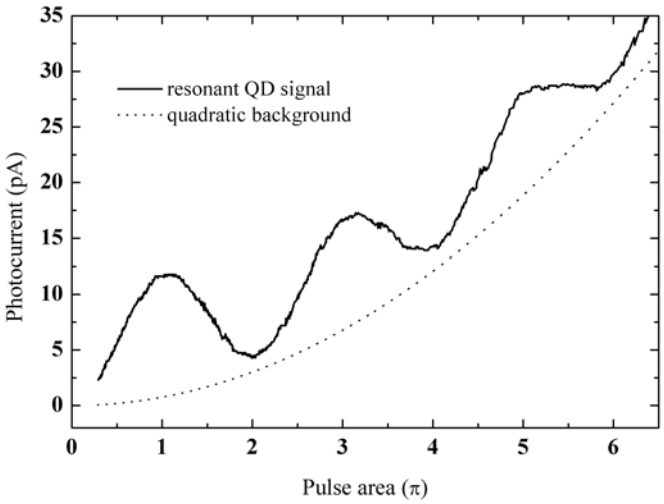

Figure 6.11: RABI-oscillation without background correction. Probably due to stray light absorptions close to the QD a background signal is generated, which is linear to the laser power.

0.6 V and circular polarized excitation. The peak width of the auto correlation signal amounts to 3,45 ps, which corresponds to spectral width of 0.6 meV. With the assumption of a sech^2 pulse-shape one gets a pulse length of 2.25 ps. The pulse area of one π corresponds to a time averaged power of 2 μW at the sample. With increasing excitation intensity, a background current increases continuously. This is displayed in figure 6.11. All further PC-measurements of RABI-oscillations shown in this work are corrected for this quadratic background signal. The background signal increases linear to the excitation power and is probably caused by incoherent absorption processes in a wider area around the nano aperture. At low excitation intensities, the incoherent signal is very low (6% at π-pulse excitation). But for higher excitation intensities, the incoherent signal strongly exceeds the coherent signal. In order to improve this, the sample design must be corrected. The active region of the SCHOTTKY-diode should be reduced as much as possible. Due to multiple laser reflections between back contact and shadow mask, a lot of unwanted off-resonance absorptions are possible. All absorptions in the mesa structure ($300 \cdot 400$ μm^2) contribute to the background. A reduced active region should improve the background signal notably.

The measured RABI-oscillations are slight damped. Comparing the results to other measured RABI-oscillations [ZBS$^+$02], the damping is very low. One can clearly see that coherent manipulations of up to 9 π are possible within one pulse. The improvements in comparison to previous results maybe caused by one of the following points:

- The self-organized grown InGaAs/GaAs QDs own a much higher confinement potential than, for example, GaAs/AlGaAs interface fluctuations [SLS$^+$01a]. The stronger damping of the RABI-oscillation is likely occurred due to the presence

of nearby states that are not well confined. QDs with stronger confinement are expected to be less sensitive to these effects. Thereby the dephasing of the InGaAs/GaAs QDs is much lower and this results in an enhanced coherent control.

- Single QD measurements are not affected by inhomogeneous broadening effects, as in ensemble measurements [BLS+02].
- The ground state exhibits a much longer dephasing time than any excited state, see chapter 7.4 (*p*-shell RABI-flopping). [KGT+01, HTK+02a, BBM03, MWB+04, WMB+05].
- Comparing these results to (former) measurements on similar structures, reported in [ZBS+02], one has to notice that the electrical and optical setup was strongly improved; especially the laser system for the excitation provides a much more stable signal.

6.3.2 Damping of the RABI-oscillations

The pulse area (needed for RABI-oscillations) is simply increased by a change of the attenuation of the excitation amplitude. Thereby the damping of the RABI-oscillation is only affected by the excitation amplitude. A constant low damping of the RABI-oscillations is observed in the range between 0.4 V and 0.75 V. This is remarkable, because the dephasing time in this region changes from 320 ps to 50 ps (see figure 6.16). With further increase of the applied voltage, and thereby reduced tunneling times, the increase of the photocurrent up to the first maximum is similar as compared to low voltages. But the decrease to the minimum is reduced, shown in figure 6.12. Similar to the measurements presented before, the real PC value (at high pulse areas) of the signal could be slightly different due to the subtraction of the incoherent background. However, the results shown here are the most probable, because the background is assumed to be monotonous. It is remarkable that the photocurrent does not approach the value 1/2 for occupation. This can be explained by the fact that the tunneling process is the main dephasing process in this voltage region. If a tunneling process takes place during the interaction, the QD is then again in the initial state. The residual pulse area for this interaction is then reduced. This statistically leads to an increased damping and to a higher incoherent signal. The average occupation for high pulse areas is then higher than 1/2 for a single interaction.

Therefore, there is a difference in the damping behavior of RABI-oscillations between short and long dephasing times, see figure 6.10 and 6.12. The strong damping, which arises from the dephasing, can only be observed if the dephasing time reaches the magnitude of the pulse length. Then the two effects of power induced damping and damping due to short dephasing times are overlaid. The influence of the fast dephasing processes during or shortly after the excitation is also subject of investigations of other groups, see for example [BLS+01, VAK03]. There are different theoretical approaches in order to identify the damping mechanisms. Due to the oscillation up to high pulse areas (9 π), these results are helpful for theoretical simulations.

One approach for the explanation is the electron-phonon interaction. J. FÖRSTNER *et. al.* calculated a density matrix theory of the electron-phonon interaction up to the second

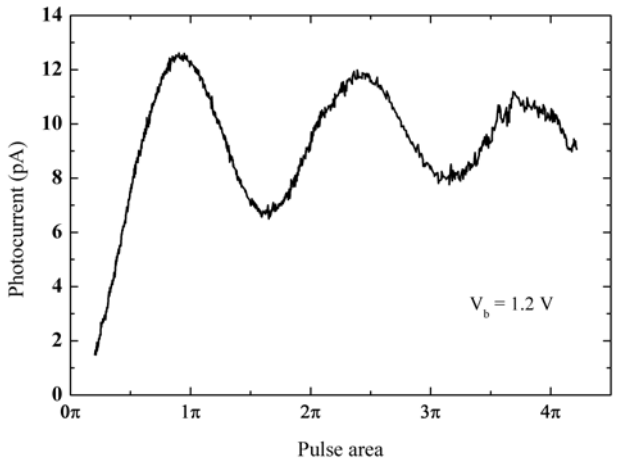

Figure 6.12: RABI-oscillations at 1,2 V applied voltage. The oscillation exhibits a stronger damping due to the short tunneling time of only 10 ps. The photocurrent does not approach the occupation value of 1/2 for high excitation intensity.

order of a correlation expansion [FWDK03]. The presented phonon-induced *pure dephasing* exhibits a reduced damping of RABI oscillations in QDs. For pulse durations on the time scale below the phonon-induced dephasing, a pure single exponential approximation can be applied. But for longer pulses, the full quantum kinetic dynamics must be included.

In reference [MJ04] P. MACHNIKOWSKI and L. JACAK studied the carrier-lattice dynamics for optically induced RABI oscillations of exciton occupation in a QD. They showed that the lattice response is resonantly driven by a combination of the linear pulse spectrum and the RABI-frequency. The RABI-oscillations are almost perfect for very short pulses (1 ps), then lose their quality for longer pulse durations (10 ps). It is surprising that in this theory the quality of oscillations is again nearly perfect for longer pulses (50 ps).

J. M. VILLAS-BOAS *et. al.* studied the influence of multiexciton and wetting layer states [VBUG05]. They described that for short pulses the two-level model fails and higher levels should be taken into account. Thus, the damping observed cannot be explained using constant rates with fixed pulse duration. The damping of the RABI-oscillations could be induced by an off-resonant excitation to or from the continuum of wetting layer states.

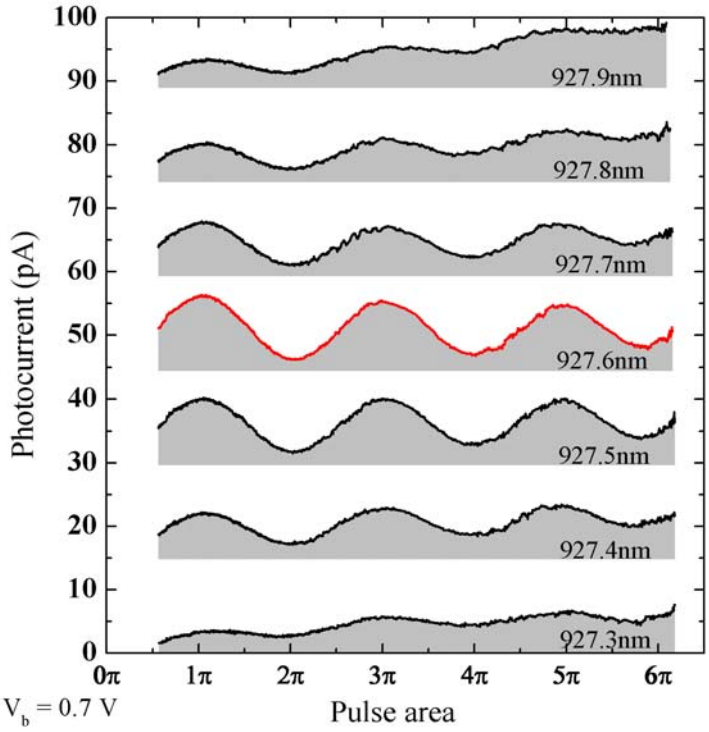

Figure 6.13: RABI-oscillations for different detuning (concerning laser - resonance at $V_B = 0,7\,\mathrm{V}$). The central curve at 927.6 nm corresponds to resonant excitation. With increasing detuning, the amplitude of the oscillation decreases.

6.3.3 Detuning

In chapter 3, the solution of the optical BLOCH equations with and without detuning is shown. For the case of a slight detuned excitation this leads to [MS91]:

$$P_{|1X\rangle} = \frac{\Omega_0}{\sqrt{{\Omega_0}^2 + \delta^2}} \sin^2\left(\frac{\sqrt{{\Omega_0}^2 + \delta^2}\, t}{2}\right). \tag{6.2}$$

If the detuning δ is higher than the RABI-frequency Ω_0 for resonant excitation, this results in a notably reduced occupation probability N_1 for the upper level. In addition, the RABI-frequency $\sqrt{{\Omega_0}^2 + \delta^2}$ is enhanced. Experimentally, the RABI-oscillations are measured as a function of the excitation amplitude, which is proportional to Ω_0. For a strong excitation (or $\Omega_0 > \delta$), the occupation of the upper level converges fast to the values known from resonant excitation. The maximum occupation probability almost reaches 100 %. This prediction cannot be verified in the experiment. While the simplified and analytically solvable theoretical model supplies a good description in almost all regions, the spectral broadening of the short pulses influences the measurements.

Figure 6.13 shows the RABI-oscillations for different detunings. The central curve cor-

responds to the case of resonant excitation. The detuning changes in steps of 0.1 nm of laser wavelength (0.144 meV). The peak width at FWHM was (in this experiment) 0.4 nm. Therefore the curves displayed cover the whole width of spectral pulse range. With increasing detuning, a continuous damping of the RABI-oscillations can be observed. Contrary to the expectation of the simple theoretical model, the amplitude only slightly approaches the resonant case. In the case of a small detuning, a significant change of the RABI-frequency is neither measured nor theoretically expected. Even in the strongest detuning ($\delta = 0,23\,\Omega_0$), one only expects a shift of maximum 3 %.

6.4 Quantum interference

6.4.1 Double π/2 pulse excitation

In this section, the coherent behavior of the single exciton ground state is used in two time delayed interactions. While a measurement of RABI-oscillations represents the occupancy of a two-level system, one has to perform quantum interference experiments to also gain access to the phase of coherent excitations. If the QD is excited in a coherent process, the generated exciton will oscillate with the excitation frequency. Then the phase of the excitation pulse is stored in the QD. The phase of the excitation will be lost after the dephasing time. The main dephasing mechanism is the tunneling process, which is strongly depending on the applied voltage. This leads to a loss of the phase relation between the exciton and the laser pulse. In order to determine the dephasing time it is necessary to test the interference ability of the exciton with a second laser pulse. For long time delays between the excitation pulse and the delayed test pulse, the detectable interference decreases.

The basis for measurements of the dephasing time is the coherent state preparation. The first manipulation excites the two level system with a $\pi/2$ pulse and thereby defines a phase. The excitation pulse of two times $\pi/2$ corresponds to a pulse area of 1π (single pulse) at complete overlapping pulses and constructive interference. The $\pi/2$-pulse corresponds to a rotation of the BLOCH-vector from the zero state to the equator. Thus, the first pulse creates a coherent superposition of the "0" and "1" states. For the test of the interference ability, the second pulse follows up with a variable delay in the range of 0 to 1000 ps. The relative phase of the second pulse can be controlled via an additional fine delay with sub femto-second resolution (25 nm delay of one interferometer arm). At time separated excitation pulses, the QDs superposition state is expected to be transferred into the pure "1" or "0" states, depending on whether the excitons phase and the laser phase interfere constructively or destructively. By varying the phase continuously (via the fine delay), an oscillation of the final state can be observed. After the interaction of the second pulse, the exciton is able to tunnel out of the QD and the final state is displayed in the PC. For long delay times, both interactions lead to independent tunneling processes (with a current of two times $\pi/2$) and no interference can be observed. The observed oscillation in the PC has the same period as the excitation wavelength.

Figure 6.14 shows a measurement of the quantum interference of the QDs exciton and the laser pulse. The time delay here is 133 ps at an applied voltage of $V_B = -0.59$ V. One can see a clear and symmetric (around the mean value) oscillation with varying fine delay. The oscillation frequency corresponds to the excitation wavelength. The optical path length is two times the coarse delay (back and forth). For the analysis of the dephasing time of the system, the decay of the oscillation amplitude must be investigated as a function of the time delay. The amplitude of these oscillations versus delay time is displayed in figure 6.15. At low time delays, the interference amplitude corresponds to a full π pulse, but for longer time delays, the amplitude decreases due to the dephasing process. Due to the strong voltage dependence of the tunneling time, this measurement must be performed at different voltages.

Figure 6.15 shows the result of the analysis of the oscillation amplitude depending on

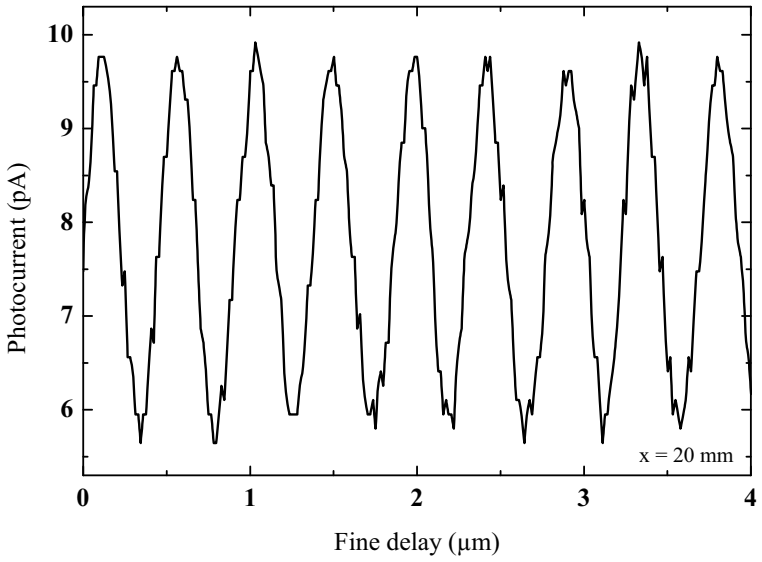

Figure 6.14: Interference pattern in the photocurrent at double pulse excitation (applied voltage:$V_B = -0.59$ V and time delay: 133 ps).

the time delay. The data (represented by squares) correspond to an excitation polarization where the excitation is limited to only one of the asymmetry split levels. A fit to these data points reveals a purely exponential decay, corresponding to a dephasing time of T_2= 322 $\pm$ 5 ps at an applied (reverse) bias voltage of 0.4 V. The analysis of the signal in the timescale at overlapping pulses is complicated and neglected here. It is still possible to determine the dephasing time without using the data by overlapping pulses. The circles correspond to an excitation polarization at which both states of the asymmetry split doublet are excited. Here an additional beating can be observed with a period of T = 133 ps. Due to the fact that the experimental setup is insensitive to a phase shift of 180°, the data has to be fitted to an exponential decay modulated by the absolute of a cosine function $\cos(\pi t/T)$. The period T can be converted into an energy difference by using $\Delta E = h/T = 31\mu$eV, which is in good agreement with the value observed in a direct measurement as displayed in figure 6.2.

Another feature of the double pulse technique is the possibility to compare the dephasing times measured by quantum interference experiments with those derived by linewidth analysis. Especially at low applied bias voltages (corresponding to long tunneling times), one has to consider that the linewidth is mainly determined by the power induced line broadening. One has to perform a full power broadening analysis with an extrapolation to zero excitation for all measurements up to 0.6 V. At higher bias voltages, the PC saturation value is high enough so that the linewidth of a low-power spectrum already exhibits the correct results. The linewidth can be converted into a dephasing time T_2 via $T_2 = 2\hbar/\Gamma$. The corresponding data are plotted versus bias voltage in figure 6.16 (full circles).

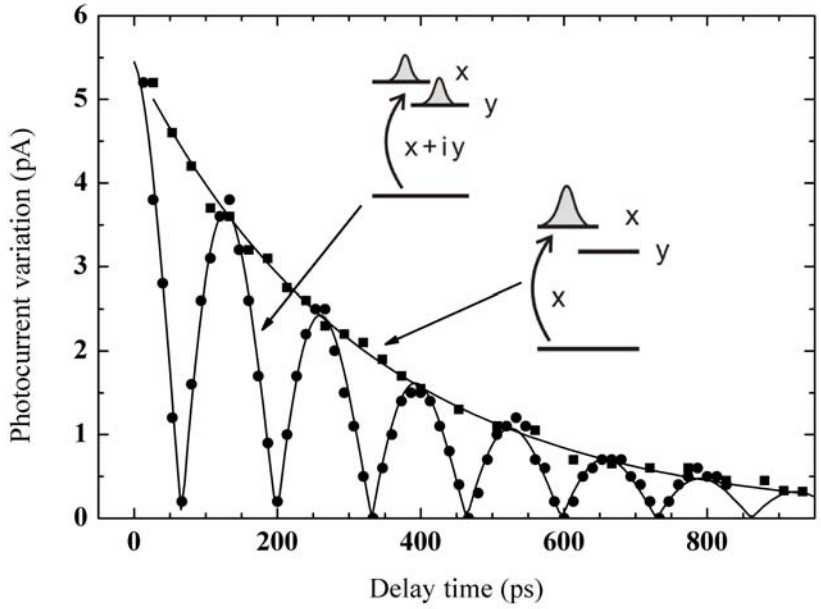

Figure 6.15: Dephasing of the QD ground state at 0.4 V. The interference amplitude decreases with increasing time delay due to the dephasing processes. The additional (quantum) beating can be observed if both fine structure states are excited. The beating frequency matches the fine structure energy splitting very well. (published in [SEZB05, ZSE+06])

The strong voltage dependence indicates that the dephasing time is mainly determined by the tunneling time. Optical recombination processes are only of significance at very low voltage levels, in the transition region from photocurrent to photoluminescence. In the investigated regime, it is therefore possible to control the main dephasing mechanism of the quantum system via the bias voltage. T_2 times derived from the quantum interference experiments are shown in the same figure, indicated by triangles. Both sets of data show excellent agreement up to a bias voltage of 0.7 V. This indicates that dephasing times for excitation with two $\pi/2$ pulses are exactly the same as for vanishing excitation power. Both sets of data agree in a range from 80 to 320 ps. At higher voltages, one observes quantum beats independent of the choice of polarization.

A possible explanation for this behavior is based on the strongly reduced tunneling times at high applied voltages. At a (reverse) bias voltage of 0.8 V, the dephasing time of linewidth analysis and quantum interference differ. Here the dephasing time amounts to approximately 60 ps, see figure 6.16. But this is also the first minimum of the quantum beating, see figure 6.15[2]. At (reverse) voltages higher than 0.8 V the linear polarization

[2]In this figure the beating is shown at a (reverse) bias voltage of 0.4 V. The beating frequency is not influenced by the applied voltage.

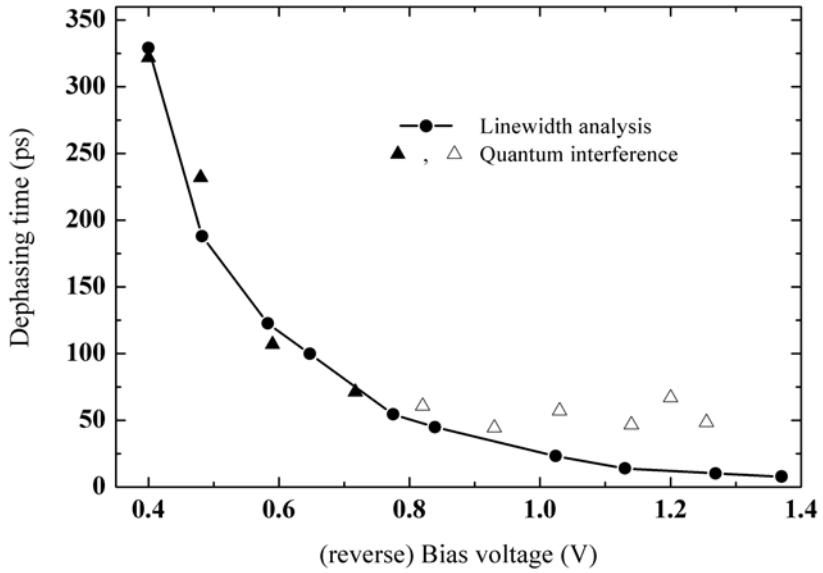

Figure 6.16: Comparison of the dephasing times derived from line width analysis and double pulse interference. Up to 0.8 V the dephasing time of the line width analysis matches the results of the double pulse experiments very well. (published in [SEZB05, ZSE+06])

of the fine structure levels may no longer be developed due to the short tunneling times. Even in cw-resonances, one can see that the fine structure splitting vanishes for voltages higher than 0.8 V, due to the tunneling induced line broadening. Here it is no longer possible to analyze the polarization dependence of both states. If the linear polarization of the fine structure states is no longer maintained, a single state is not addressable by the orientation of the linear excitation polarization. Thereby the pulsed excitation would always excite both fine structure states at high (reverse) bias voltages and a quantum beating could not be suppressed.

The linewidth of the ground-state resonance corresponds very well to the decay time of quantum interference. The asymmetry-induced splitting of energy levels is obtained in the period of quantum beats. The polarizations at which these effects can be suppressed are the same in both types of experiments at voltages lower then 0.8 V. From saturation and power broadening experiments, one derives a characteristic dimensionless power level $\tilde{P} = \Omega^2 T_1 T_2$. As T_1 and T_2 times are also obtained from these experiments, it is possible to compare the resulting RABI-frequency Ω to a direct measurement of RABI-oscillations. In cw measurements, one gets a typical value of $\Omega \approx 0.2$ GHz at a laser power of P = 100 nW. A comparison of different measurements delivers a more general ratio of $\Omega/\sqrt{P} = 0.19 \pm 0.4\mathrm{THz/mW}^{1/2}$. In a measurement of RABI-oscillations as shown in figure 6.10, the laser power for an inversion (π-pulse) corresponds to 2 μW. After a conversion into continuous excitation this value results in $\Omega/\sqrt{P} = 0.25 \pm 0.3\mathrm{THz/mW}^{1/2}$. Both values of the RABI-frequency agree remarkably well.

6.4.2 RAMSEY fringes

In this section, the coherent control of a QD two level system in a double-pulse RAMSEY experiment is presented. The experimental setup for the RAMSEY experiment is nearly the same as the double pulse experiments. The only difference here is the fixed time delay between the two laser pulses and the variation of the applied voltage. A change of the voltage directly affects the phase evolution of the exciton.

History

The original experiment, performed by NORMAN F. RAMSEY, consists of the interaction of two time delayed electromagnetic pulses with an incomplete inversion ($\pi/2$-pulses) of quantum systems. For the quantum systems, an atomic beam was used, which was excited by two microwave pulses. The time delay was reached due to spatially separated interaction zones where the atoms need time to pass through. The required detuning between the quantum systems and the excitation was achieved by the detuning of the microwave field compared to the transition energy. The first state manipulation takes place in the first interaction zone with a pulse area of $\pi/2$. The second manipulation takes place in the second interaction zone. Now it depends on the phase of the quantum system whether the interaction takes place constructively or destructively. The final state (respectively the phase before the second interaction) thereby depends on the quantum state detuning. The transition energy of the quantum system is fixed and is not influenced by an external parameter. Thereby it was possible to stabilize the microwave frequency with the optically measured final state. This concept is the basis for extremely accurate atomic clocks, where the time is triggered by the stabilized microwave frequency. This effect was first described by NORMAN F. RAMSEY [Ram90] and it was honored in 1989 with the NOBEL prize.

RAMSEY effect in an electric field tunable device

With double pulse excitation in an electric field tunable device, it is possible to control the occupancy and the phase of the quantum mechanical two level system entirely via the bias voltage. Comparing the original RAMSEY experiment with the setup used here, the laser frequency (quantum state excitation) is fixed, and the detuning is done via the QCSE, see chapter 5.2. The QD transition energy decreases with increasing (reverse) bias voltage. A detailed measurement of the STARK effect gives a conversion of voltage into energy scales. Therefore it is possible to tune the QD energy precisely with respect to a fixed laser wavelength. In the present case, the final quantum state is detected in the PC. Thus, the detuning is switched from the excitation to the quantum system.

Figure 6.17 (a) shows the difference in the PC response between pulsed and continuous excitation of the exciton ground state in the PC. In the case of continuous excitation, the observed spectral response corresponds to the homogeneous linewidth of the system. For pulsed excitation, the PC signal directly displays the power spectrum of the laser. The FWHM of 0.47 meV corresponds to the transform limit of a 2.6 ps laser pulse. The QD can therefore act as a spectrum analyzer in the PC regime.

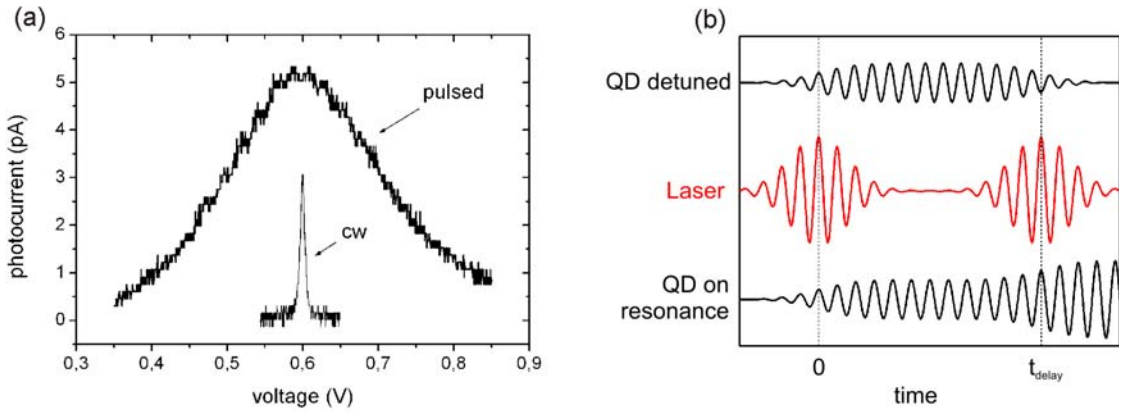

Figure 6.17: (a) Photocurrent spectra of the single exciton ground state comparing continuous and pulsed ($\pi/2$) excitation. (b) Schematic picture of the phase relation between the two laser pulses (central) and the two cases of detuned (upper curve) and resonant (lower curve) QD excitation. (published in [SEZ06, ESdV$^+$06b, ZSE$^+$06])

The exciton ground state of the QD represents a two level system. The lower state $|0\rangle$ is defined by an empty dot, and the upper state $|1\rangle$ by a single exciton ground state occupancy. A π pulse switches the occupation from $|0\rangle$ to $|1\rangle$ or vice versa. The time separation of the two $\pi/2$ pulses is achieved by the MICHELSON interferometer, described in section 4.1.5. Figure 6.17 (b) schematically displays the phase evolution of the quantum state for two laser pulses. The central curve corresponds to the two laser pulses with the frequency ω_{laser} separated by a delay time t_{delay}. In the lower case, the QD oscillates in exact resonance ($\omega_{QD} = \omega_{laser}$) with the laser. After the first laser pulse, the QD is therefore in a coherent superposition between $|0\rangle$ and $|1\rangle$. The second laser pulse is then in phase and the system will be transferred into the pure state $|1\rangle$. The upper curve corresponds to the same situation with a slightly detuned QD. The QD phase is defined again by the first laser pulse. But the phase evolution will evolve with a slightly different frequency ($\omega'_{QD} = \omega_{laser} - \Delta\omega$ with $\Delta\omega \ll \omega$). When the second interaction occurs, the QD can have a different phase when compared to the previous case (opposite phase in this example), resulting in the final state $|0\rangle$. Within the pulse duration, the phase relation between the QD and the laser can be regarded as fixed. The final state occupancy will oscillate as a function of the detuning $\Delta\omega$ with a period of $2\pi/t_{delay}$. The frequency of the spectral fringes increases directly proportional to the delay time between the two pulses.

Figure 6.18 displays RAMSEY fringes with different time delays in a range from 33 to 167 ps. The oscillation is caused by a voltage dependent detuning of the QD between the two interactions. Obviously the oscillation frequency increases directly proportionally to the delay time between the two pulses. There is also a slight increase in the frequency of the RAMSEY-fringes observable towards higher bias voltages. This is a result of the nonlinear (quadratic) STARK effect. The envelope of the PC spectra corresponds to the

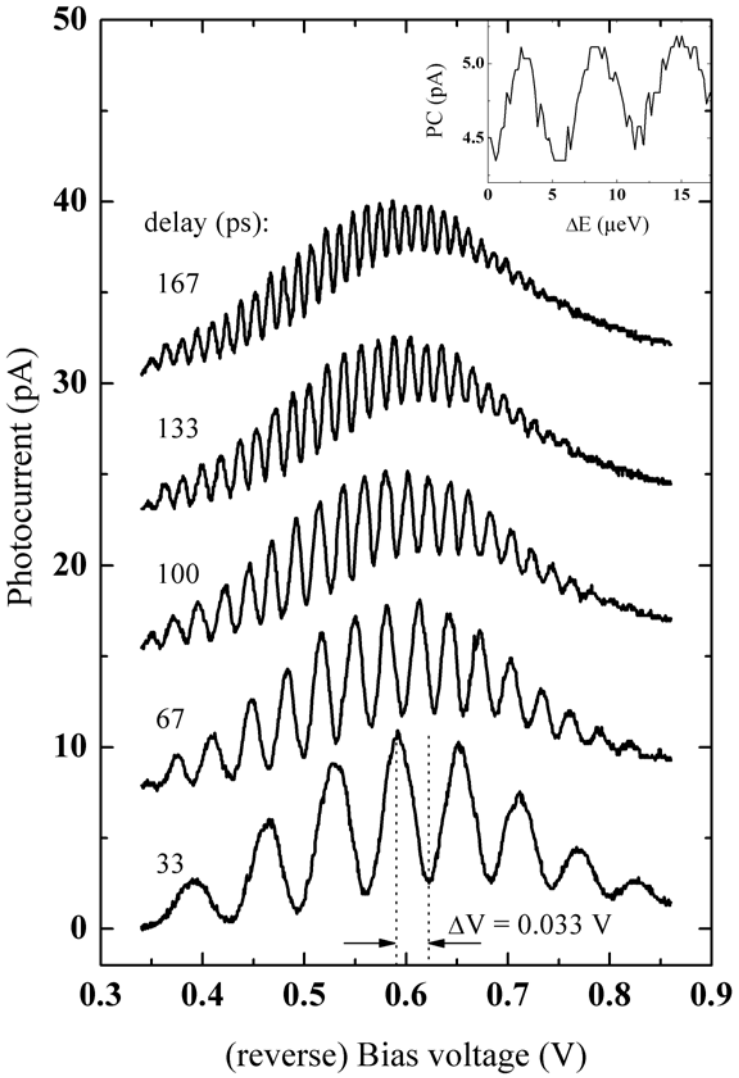

Figure 6.18: RAMSEY fringes measured in the photocurrent with double pulse excitations for different delay times. (published in [SEZ06, ESdV$^+$06b, ZSE$^+$06])

spectrum of a single pulse with a pulse area of two times $\pi/2$. At a fixed bias voltage, the interference contrast decreases due to the finite dephasing time of the system toward longer delay time. Also at a fixed time delay, the interference contrast decreases with increasing bias voltage. This is caused by the strong voltage dependence of the dephasing time. At long time delays and high (reverse) voltages, both pulses generate a PC signal of $\pi/2$ (as shown in figure 6.17 a). In this regime, the tunneling time is shorter than the delay time between the two laser pulses. The interference will be lost if the exciton tunnels out of the QD before an interaction with the second pulse becomes possible. RAMSEY fringes are visible at delay times even longer than the dephasing time of the QD system. This is shown in the inset of figure 6.18. The half period of the RAMSEY fringes at a voltage of 0.43 V and a delay time of 670 ps is only about 3 μeV, which is smaller than the homogeneous linewidth of the system (5 μeV). The spectral resolution of the double pulse experiment hence exceeds any possible single pulse experiment.

The RAMSEY method can also be applied to a quantum mechanical two qubit gate operation. As shown in figure 6.18, very small energy shifts are already sufficient for a full 1π variation of the final state rotation angle. This energy shift can be achieved by e.g. a dipole-dipole interaction between neighboring dots ([UML$^+$05]). Thus a relatively weak coupling of states could be used for a conditional qubit rotation. It is possible to fit the gate operation time to any coupling strength simply by varying the delay time. But any change in the environment of the QD, which has an effect on the exciton transition energy, will lead to a detuning of the system. This will result in an observable variation of the final state occupancy at a constant bias voltage. The QD can therefore act as a highly sensitive quantum sensor for interactions occurring in the time interval between the two laser pulses. The RAMSEY setup offers a unique switch between constructive and destructive interference simply by a small variation of the bias voltage. For delay times longer than the dephasing time, the spectral resolution of the RAMSEY setup is increased beyond the continuous excitation limit (i.e. the homogeneous linewidth). Due to the RAMSEY method, here a new link between voltage based control and the coherent control of single quantum system is demonstrated.

7 First excited state

7.1 Voltage dependent photoluminescence for *p*-shell excitation

In chapter 5.3, the spectral position of the excited states of the single QD was analyzed. Thus, it is possible to investigate the *p*-shell transition for different external parameters, e.g. voltage, polarization, excitation intensity, etc. Due to the integration of the QD into a *n*-*i*-SCHOTTKY diode, it is possible to perform the PLE measurements at different voltages. The results of this measurement series is shown in figure 7.1 for voltages from 0 V down to -0.5 V. The spectral position of the *p*-state shifts as expected from 0.0 V to -0.1 V due to the QSCE. From -0.1 V to -0.2 V, however, the *p*-state signal shows a strong shift of about 2 meV into the red. Going further to higher negative voltages, the *p*-state peak position again shifts continuously with the applied bias voltage. The jump of the *p*-shell peak position from -0.1 V to -0.2 V is an effect of a change of charge carrier in a QD. Figure 5.1 shows that the X^--state vanishes between -0.1 V to -0.2 V. Here the electron ground state is shifted above the quasi-FERMI-energy of the back contact, and electrons from the doped back contact are no longer able to tunnel into the QD. An extra electron leads to energy renormalization also for the excited state. The PLE peak intensity decreases as expected towards higher applied voltages. The probability of a tunneling process for the excited exciton dominates the optical recombination process at higher applied voltages.

The LO-phonon absorption peak (1.376 eV) decreases and shifts with the applied voltage, as expected. The PL signal of the peak at 1.38 eV (probably the *d*-shell) decreases very quickly. This can be explained by the higher tunneling probability (much lower tunneling barrier) for the charge carriers at higher excited QD states. Other measurements performed on this sample (by MARC. C. HÜBNER), concerning the photocurrent signal of excited QD states, verify the fact that the tunneling probability is much higher for excited states. Two further resonances appear between -0.2 V and -0.3 V, which couldn't be assigned up to now.

Another interesting feature of the *p*-shell excitation is shown in figure 7.2, which shows the voltage dependent ground state luminescence at *p*-shell excitation. For normal voltage dependent PL (at non-resonant interband excitation, figure 5.1), the luminescence of the exciton vanishes at -0.35 V. In the case of resonant *p*-shell excitation, one can observe luminescence of the ground state (and the positive charged exciton) up to a voltage of -0.8 V. At a voltage of -0.35 V, the intensity of exciton is strongly reduced. Here the tunneling time decreases to values shorter than the radiative lifetime. It is clear that the generated charge carriers are able to tunnel out of the QD direct from the *p*-shell (strongly reduced barrier) or from the ground state. Comparing the non-resonant interband and the *p*-shell excitation, the non-resonantly generated interband excitons are able to tunnel out from even higher levels. Therefore the ground state PL at *p*-shell excitation can be

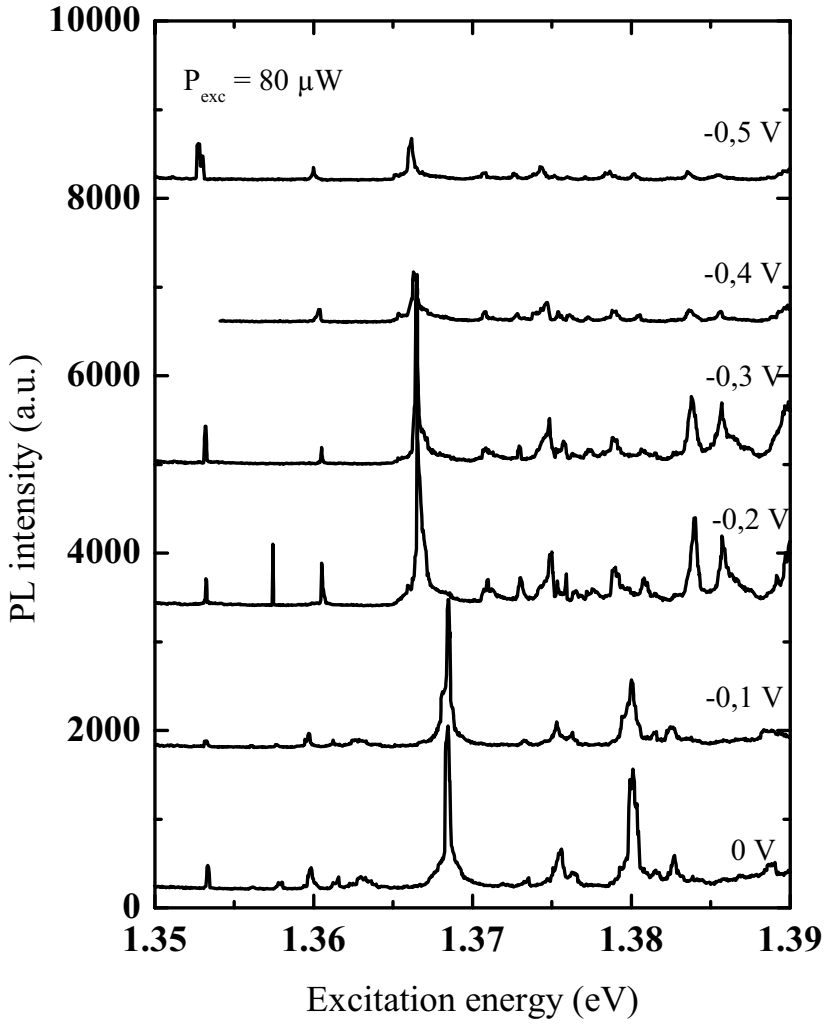

Figure 7.1: Voltage dependence of the PLE signal at ground state detection (neutral exciton) and resonant *p*-shell excitation. Up to higher voltages the normal luminescence vanishes due to change to tunneling processes. In the step from -0.1 V to -0.2 V the *p*-shell transition shifts 2 meV into the blue. In this region the QD cannot be charged from electrons from the back contact.

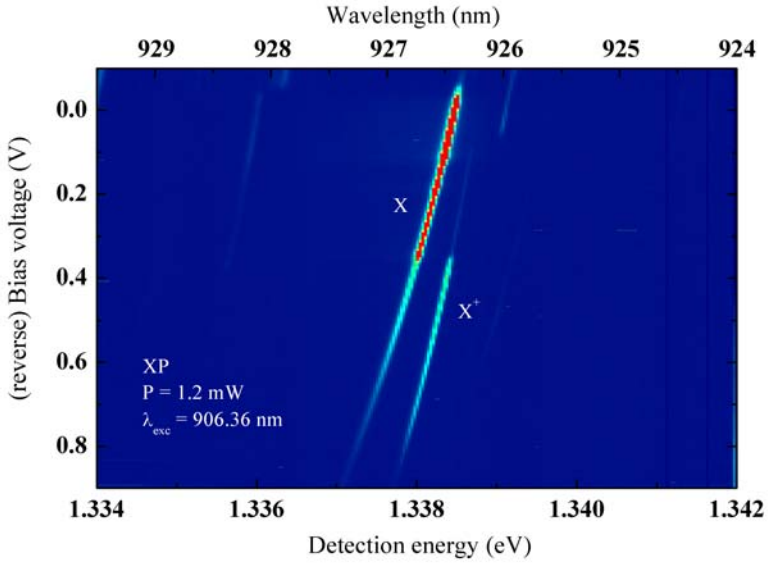

Figure 7.2: Voltage dependence of the ground state by resonant excitation of the p-shell. The luminescence of th X^+ can be observed probably due to a biexciton generation and a tunneled exciton.

seen even at higher applied (reverse) voltages as compared to non-resonant interband excitation.

In figure 7.2 one can also see the luminescence from the recombination of the positive charged exciton. This is not possible if only a single exciton is generated. In the voltage region of the positive charged exciton, only electrons are able to tunnel out of the QD. It is not possible that a hole tunnels into the QD in order to create a positively charged exciton. Therefore it is probable that the $X+$ is generated by a biexciton excitation and an electron tunneling process. The measurements of the photocurrent saturation and power broadening (chapter 6.2.3 and 6.2.4) have shown that the tunneling times are not equal for electrons and holes, which intensities this excitation scheme. The PL-intensity of the X and X^+ PL is nearly equal and decreases slowly up to higher negative voltages. One can see that the STARK effect is not equally strong for X and X^+. The excitation intensity here is rather high (1.2 mW before pellicle, which corresponds to an intensity at the QD of approximately 50 μW). The generation scheme for the biexciton is discussed in chapter 9. In order to analyze the excitation of the biexciton, a PLE measurement is performed with the detection on the biexciton luminescence which is presented later (see figure 9.1).

7.2 Excitation polarization dependence of the p-shell

In the photocurrent regime, the possibility of fine tuning of the QD state (via QCSE) allows for high resolution spectroscopy of the QD states. Thereby it is possible to re-

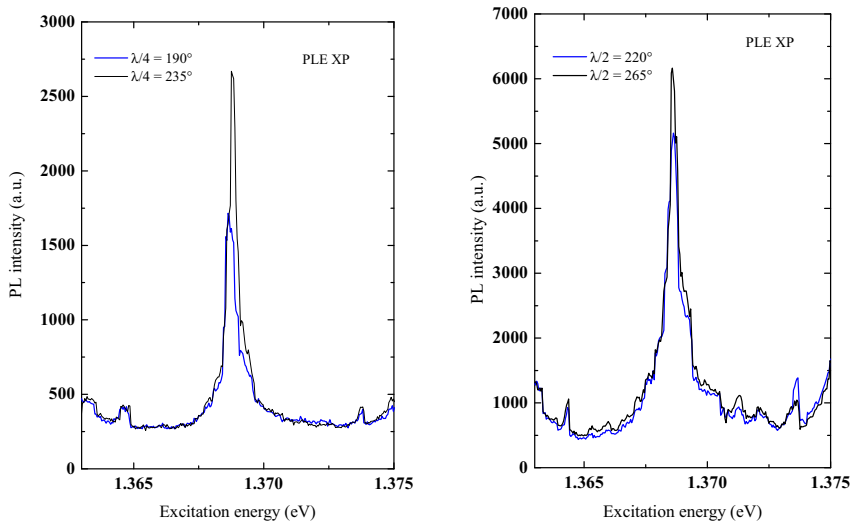

(a) Dependence of circular polarization (b) Dependence of linear polarization

Figure 7.3: Properties of the ground state luminescence at different excitation polarization.

solve the fine structure splitting of the QD ground state. In the PLE measurement, the resolution of the excitation is limited by the used laser system (step width for spectral tuning). Furthermore, the short lifetime of the excited state leads to a spectral broadened linewidth. In the ground state, one state of the fine structure could be suppressed by a linear polarized excitation, see figure 6.2. In order to analyze a possible fine structure splitting of the *p*-shell, a polarization dependent PLE measurement (linear and circular) was performed. One tuning step of the laser energy corresponds to an energy of 50 μeV.

The results of the polarization dependent PLE analysis are shown in figure 7.3. In case a), the excitation of the linear polarized laser is turned into circular polarization by using a $\lambda/4$ plate in the excitation path. By tilting the fast axis 22.5° from the laser axis, one generates circular left (and respectively circular right). One can see that the PL intensity shows a slight shift of the peak position between circular left and right polarization. The PL intensity can be reduced to nearly half intensity. Figure 7.3 b) compares the two linear polarizations (vertical and horizontal). The change of the linear polarization only slightly affects the peak height.

A clear fine structure splitting is not observed here, as it is possible in the ground state. A possible *p*-shell fine structure splitting is here washed out due to the line broadening (fast relaxation into the ground state). The *p*-shell linewidth here is 0.5 meV, which is also the upper limit for an *p*-shell fine structure splitting. The ground state shows a strong dependence on linear polarized excitation, whereby the *p*-state is affected more by circular polarized excitation.

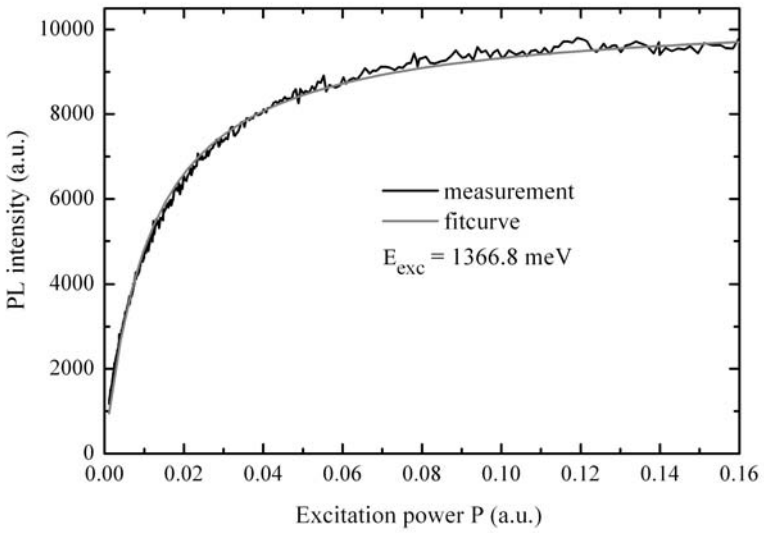

Figure 7.4: Power dependence of the PL intensity from the QD ground state for cw p-shell excitation. The PL signal shows a clear saturation behavior, as expected for a two level system. (published in [ELdV$^+$07b])

7.3 p-shell saturation

The saturation behavior of the s-shell emission with increasing p-shell excitation intensity is an important indicator for the quantum mechanical two level character of the p-shell transition. Figure 7.4 shows an analysis of the PL peak intensity versus excitation power. The p-shell transition is resonantly excited by the TiSa laser in the continuous wave mode. A clearly nonlinear power dependence can be observed, which is well described by the fitcurve

$$I = I_{sat}\frac{P}{P+1}.$$

The formula is a result of the saturation of a two-level system, which is discussed in the theoretical chapter 3.5.1. Here I refers to the PL peak amplitude (PL intensity), I_{sat} to its saturation value, and P corresponds to a normalized excitation power. At low excitation intensities, the s-shell luminescence increases linear to the excitation power. But for higher excitation intensities, the s-shell luminescence approaches a saturation value (see chapter 6.2.3 for photocurrent saturation of the ground state). The physical reason for PL saturation can be derived fairly easily: If the QD is already excited by one exciton, no further absorption can take place due to a renormalization of the energy levels caused by few particle interactions. This also holds true if the exciton relaxes to the ground state. Further absorption in the p-shell can only take place after a relaxation *and* recombination process. With the detection efficiency of the experimental setup (discussed later) and the saturation value of $I_{Sat} = 10400$ (a.u.), one can conclude that the total time for

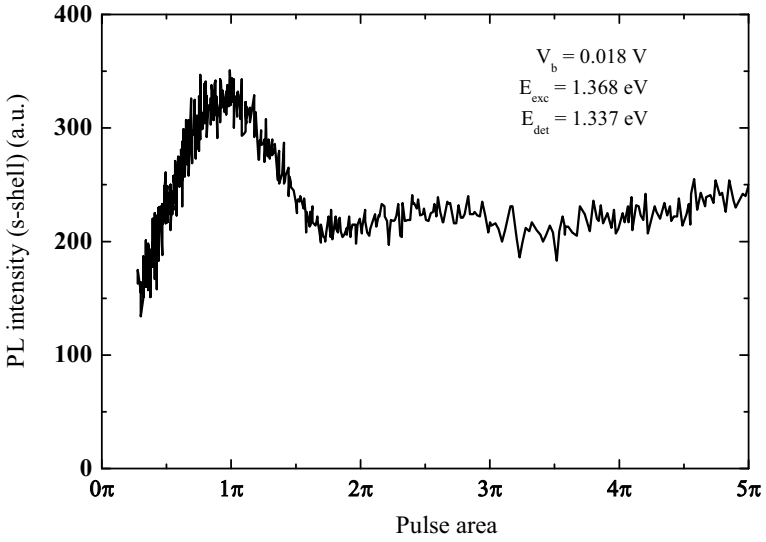

Figure 7.5: p-shell RABI-oscillations detected in the ground state PL. The RABI-oscillations have a clear developed π-pulse maximum, followed by a substantial damping at higher pulse areas. (published in [ELdV$^+$07b])

relaxation and recombination takes around 500 ps. This value matches the upper limit of the recombination time of 700 ps very well, which is inferred from the analysis of antibunching data using cw excitation, see chapter 10.5. Therefore the relaxation process is, as expected, much faster than the recombination process. The observed cw-saturation behavior underlines the two level character of the p-shell transition; a second requirement is the ability of the coherent control of the two level system.

7.4 p-shell RABI-flopping

The fundamental experiment in the coherent regime is aiming for the observation of RABI-oscillations, analogous to the ground state. RABI-oscillations from excitons confined to single QDs with optical detection have been reported by STIEVATER et. al. [SLS$^+$01b]. Here ps-laser pulses ($\tau_p \approx 2\,\mathrm{ps}$) have been used for excitation, where the spectral pulse width is sufficiently low to avoid possible off resonance excitations. The main problem for the coherent control of the excited state is a dephasing process faster than the excitation. If the QD is resonantly excited in the p-shell, the dephasing is mainly caused by relaxation to the s-shell. The projected occupancy of a two level system under coherent resonant excitation corresponds to the measured PL intensity and is given by $I = \sin^2(\Omega t/2)$. The RABI-frequency Ω is again proportional to the square root of the laser intensity (pulse area) and t corresponds to the pulse length. The pulse area (the rotation angle $\Theta = \Omega t$) is defined here by adjusting the excitation amplitude.

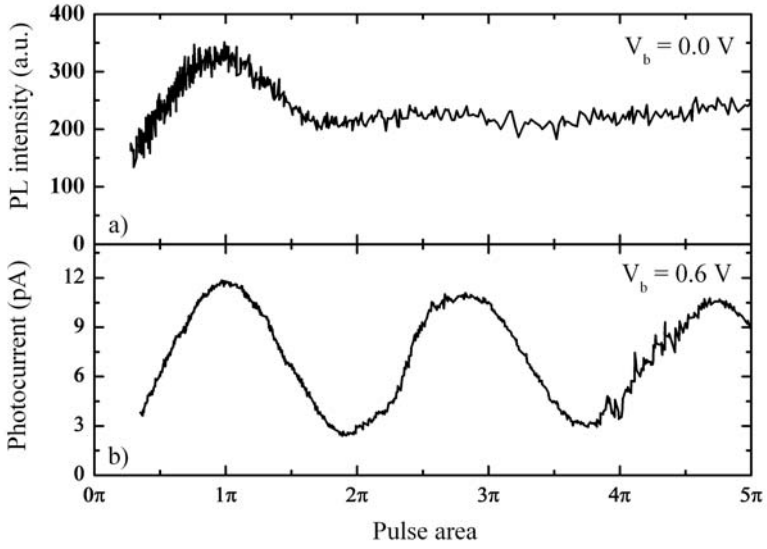

Figure 7.6: Comparison between *p*-(a) and *s*-(b) shell RABI-oscillations. The *p*-shell RABI oscillation is detected in the ground state PL, and the *s*-shell RABI-oscillation in the PC. Due to a fast dephasing (relaxation), the RABI oscillation of the *p*-shell is substantially damped when compared to the *s*-shell. (published in [ELdV$^+$07b])

Figure 7.5 shows the RABI-oscillations of the *p*-state measured in the *s*-shell PL. The PL intensity shows a clear nonlinear behavior, whereby the oscillations imply that the excitation of the QD can be controlled by the strength of the incident laser field. The measurements exhibit a strong damping of the oscillation, but the first maximum is clearly visible. The data obtained here is comparable to the results reported in [SLS$^+$01b], which have been achieved by pump-probe techniques. The damping indicates enhanced dephasing rates compared to ground state RABI-oscillations 6.10.

The kind of damping is similar to the damping of the ground state RABI-oscillations at high applied bias voltages, see figure 6.12. The high voltage leads to a fast tunneling process and thus a short dephasing time. In this case, the RABI-oscillations does not approach the value $1/2$ for occupation. The similar kind of damping of the *p*-shell implies also a very short dephasing of the *p*-shell transition, which is verified by double pulse experiments, see chapter 7.5. Thus, it cannot be guaranteed that the occupation approaches the value $1/2$ for high excitation amplitudes. In the PL, it is not possible to determine an absolute value due to the detection efficiency. This is only possible in the PC.

A π-pulse typically corresponds to an average laser power on the sample of about 2 μW at a pulse length of 2.3 ps and a laser repetition frequency of f_{Laser}= 80 MHz. For this condition, nearly every excitation pulse should lead to the emission of one photon from the *s*-shell. Therefore the maximum PL intensity can be used for an estimation of the

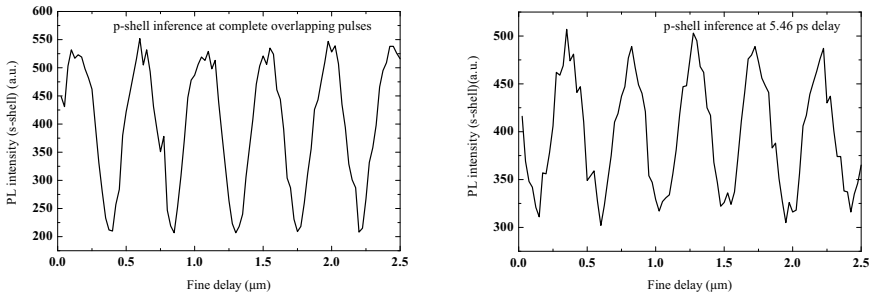

(a) Ground state PL at overlapping p-shell-excitation

(b) Ground state PL with 5.46 ps time delay between the pulses

Figure 7.7: Interference of the p-shell detected in the ground state PL

collection efficiency of the experimental setup. Assuming that every π-pulse generates one photon, the collection efficiency of this system approaches 10^{-5} (collection through shadow mask, semitransparent gate and a NA = 0.75 objective). The measurements reported in this section demonstrate coherent control of the first excited state.

In this section the coherent behavior of the s- and p-shell of the single QD is compared. Due to the use of a tunable sample, it is possible to choose the dominant dephasing process simply by the applied voltage and excitation conditions (p- or s- shell). In the first case, the QD is resonantly excited in the p-shell (low voltage). The main dephasing process here is relaxation into the ground state. After the recombination process, the projected state can be observed in the ground state PL, which is shown in figure 7.6 a). In the second case, a (reverse) bias voltage of about 0.6 V is applied, which switches the main dephasing process to tunneling. Thereby one can perform the coherent manipulation in the ground state and detect the projected state in the PC (see figure 7.6 b)). The PC signal shows more than eight full inversions (only five inversions are plotted here) at high excitation intensities within each laser pulse. The PL intensity (p-shell excitation) shows an enhanced damping compared to the PC signal (s-shell excitation). Comparing the p-shell π-pulse to the ground state π-pulse, it turns out that the RABI-flop needs about the same excitation intensity (about 2 μW at the sample). This means that the associated s- and p-matrix elements are approximately equal in this special QD.

7.5 Dephasing of the p-state polarization

With double pulse excitation, it is possible to get access to the phase of the QDs exciton. Similar to the measurement of the dephasing time of the ground state (see chapter 6.4.1), it is possible to determine the dephasing time of the p-state of the QD, which is probably much faster. A first laser pulse excites the QD in the p-shell and defines the phase of the exciton. With the second laser pulse, the ability of interference between the QD and the laser pulse is tested by changing the phase in relation to the first pulse. Depending on the time delay between the two pulses, the inference will decrease due to the dephasing.

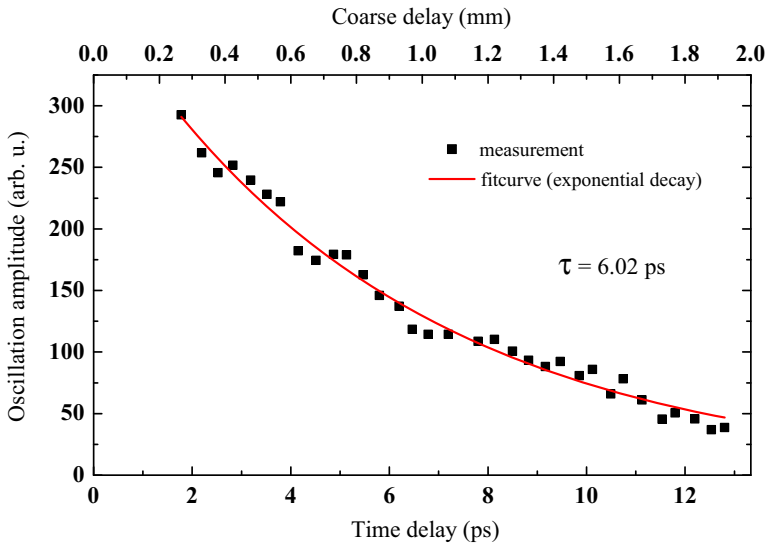

Figure 7.8: Dephasing analysis of the *p*-state. The interference amplitude at double pulse excitation is displayed versus the time delay. The PL signal at overlapping pulses is not considered.

Thus it is possible to infer a dephasing time. The main dephasing process here is the relaxation into the ground state. The relaxation process will probably not depend on the applied voltage. Thereby it is not possible to influence the dephasing time by an external parameter, like it is possible in the ground state. In this case, the optical delay time will be much shorter compared to ground state analysis.

The double pulses are generated by the MICHELSON interferometer, shown in chapter 4.1.5. The excitation amplitude used here corresponds to a single π-pulse at complete overlap of the two pulses and constructive interference (two $\pi/2$-pulses). Figure 7.7 shows the interference of the *p*-shell by varying the fine delay between the two pulses. The final state of this variation is detected in the ground state PL after the relaxation (and recombination processes). At zero time delay (Figure 7.7 a)), one can observe a very clear oscillation in the ground state PL which has a range from zero (200 a.u. correspond to zero (Si:CCD-offset)) to the full π-pulse intensity. The oscillation pattern is sinus shaped. This pattern-shape of the interference is not surprising, but the same analysis of the dephasing time of the LO-phonon assisted absorption leads to a different behavior, which will be discussed in chapter 8.5. At a delay time of 5.46 ps, the interference oscillation amplitude is lower than before, but the oscillation stays sinus shaped.

Figure 7.8 shows the decrease of the oscillation amplitude (the dephasing) of the system. One can clearly see a decrease of the PL oscillation amplitude within a range of a few mm delay of the second pulse. A mirror shift of about 1.4 mm corresponds to a time delay of ten ps. The fit of an exponential decay results in a dephasing time of the *p*-state of 6.02 ps, which is about 3 times as large as the applied pulse width (1.7 ps). One can

see that the data follow a simple exponential decay law with a decay time of 6.02 ps. This dephasing time is much too short to resolve quantum beating effects in the *p*-shell. The dephasing of the *p*-shell is much faster than the ground state dephasing and cannot be affect by external parameters. The possibility of the coherent control allows for a defined excitation of an excited state, which is used for a novel excitation scheme of single photon emission in chapter 10.

8 LO-phonon assisted absorption

In the previous chapter, it was shown that the *p*-shell transition could also be treated as a quantum mechanical two level system, like the exciton ground state. The main difference between the *s*- and the *p*-shell is the strongly reduced dephasing time due to the different dephasing processes. The *p*-shell dephasing is, however, determined by the relaxation process, which is much faster than the dephasing due to tunneling processes. The LO-phonon absorption resonance is different to both, *s*- and *p*-shell, dephasing processes. Here LO-phonons are generated during the excitation process of the exciton. The excitation scheme is shown in figure 8.1. The excitation energy fits to the ground state energy plus the energy of a GaAs-LO phonon. The ground state is thereby generated with the help of an emitted GaAs-LO phonon. The ground state is then able to decay by optical recombination. It is possible that the GaAs-LO phonon propagates in the bulk GaAs crystal. There are some interesting questions about the properties of the LO-phonon state.

- How long does the phonon assisted transition maintain coherent?
- Is it possible to perform a coherent manipulation with the LO-phonon assisted absorption?
- Can the LO-phonon assisted transition be treated as a two-level system?
- Is the phonon assisted absorption polarization sensitive?

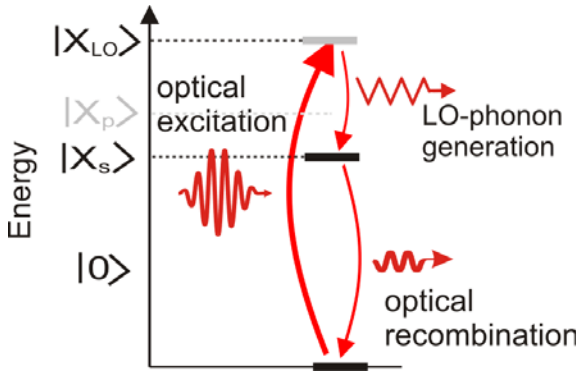

Figure 8.1: Scheme of LO-phonon assisted excitation of the ground state.

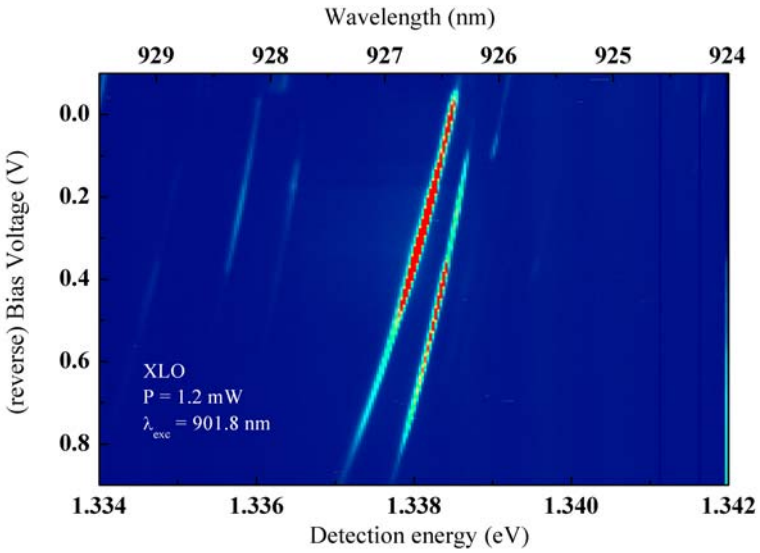

Figure 8.2: Voltage depending photoluminescence by LO-pumping. The luminescence of the X^+-state is again visible due to the biexciton generation and a tunneled electron.

8.1 Voltage depending photoluminescence

In order to compare the *p*-shell transition with the LO-phonon assisted transition, a voltage dependent photoluminescence measurement is performed. The region investigated here is again between -0.9 V and 0.1 V. The excitation power is 1.2 mW (before pellicle) at an energy of 1.375 eV. Figure 8.2 shows that the luminescence of the ground state is visible in the same region (from 0.05 V to -0.8 V) as for the *p*-shell transition (see figure 7.2). With this experimental setup, the positively charged exciton X^+ (which is close to the luminescence of the neutral exciton) is also detected. The luminescence of the X^+ vanishes when electrons from the doped back contact are able to tunnel into the QD (similar to the voltage dependence at non-resonant interband excitation). Both lines show a (different) red shift, arising from the QCSE (see chapter 5.2). The luminescence of both lines can be observed at even higher electrical fields than at non-resonant interband excitation. The exciton ground state is, in this case, directly generated with the help of LO-phonon assisted absorption. At *p*-shell excitation, the exciton is able to tunnel out of the QD from the *p*-shell and the *s*-shell. In the case of LO-phonon assisted absorption, the excitons are only able to tunnel out of the QD from the ground state. Therefore the luminescence of the ground state can be observed up to high electrical fields (-0.8 V). The PL intensity of the positive charged exciton X^+ is higher in the case of LO assisted absorption than at *p*-shell excitation. This could be explained by a higher probability of biexciton generation, which is discussed in chapter 9.

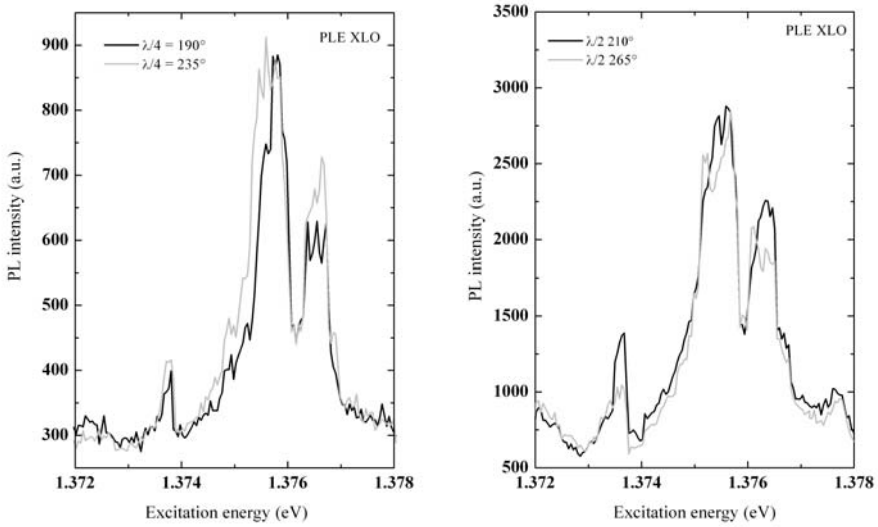

(a) Dependence of circular polarization (b) Dependence of linear polarization

Figure 8.3: Properties of the ground state PL and polarized excitation of the LO assisted absorption.

8.2 Polarization analysis of the LO-phonon absorption

The LO-phonon resonance is quite broad (0.8 meV) compared to the *p*-shell resonance. Using formula 3.33, this cw linewidth results in a very short dephasing time of only 1.7 ps. If the LO-phonon resonance could be affected by a specific polarization of the excitation, one should be able to observe a change in the PLE spectrum (e.g. a shift, or partly suppression). Due to the combined exciton-phonon excitation and a the very short dephasing time a polarization dependence of the LO assisted excitation is not expected. Figure 8.3 shows the results of the polarization dependent excitation. A change of the linear polarized excitation has no effect on the PLE intensity of the ground state figure 8.3 b). But in figure 8.3 a) one can see a slight energy shift of the resonance by changing the circular polarization. The origin of this effect is unknown so far. However, the combined generation of exciton and phonon is possible with any excitation polarization. Apart from the identification of the GaAs LO-phonon resonance by the energy match, this absorption resonance is different as compared to a normal shell transition. This confirms the identification of the LO-phonon assisted transition.

8.3 Saturation of the LO-phonon assisted transition

Since the *p*- and *s*-shell occupation show a saturation behavior with increasing (cw-) excitation intensity, one would like to know if the LO-phonon assisted transition also shows saturation behavior. This is an important indicator for the two level character of the LO-phonon assisted absorption. For the case that the LO-phonon resonance behaves as a

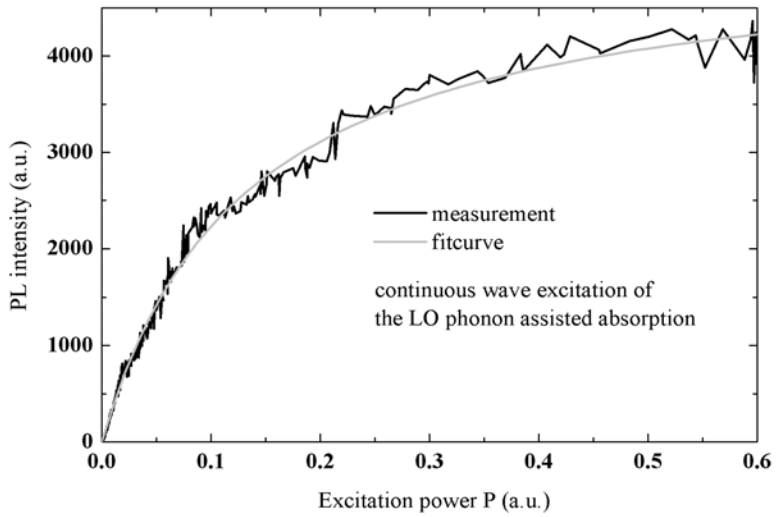

Figure 8.4: Saturation of the LO-absorption at continuous excitation. The signal shows a normal saturation behavior, but a reduced saturation intensity of only the half of the *p*-saturation value.

quantum mechanical two level system, its power saturation should follow the formula $I = I_{sat}\frac{P}{(P+1)}$.

Figure 8.4 shows an analysis of the PL peak intensity versus excitation power. Here I refers to the PL peak amplitude (PL intensity), I_{sat} to its saturation value, and P corresponds to a normalized excitation power. At low excitation intensities, the *s*-shell luminescence increases linear to the excitation power. But for higher excitation intensities, a clearly nonlinear power dependence can be observed. Up to an excitation power of 0.1 a.u., the PL intensity of the ground state increases with the excitation intensity. In this regime, the behavior could be well described by the fit-formula. For excitation intensities larger than 0.1 a.u. (see figure 8.4), the PL intensity shows slight variations from the fit curve. Comparing the LO-phonon PL signal to the *p*-shell transition, one can see that the data here exhibit more noise than the *p*-shell transition (especially at higher excitation amplitudes). Nevertheless, the PL-signal shows saturation behavior. The saturation value I_{sat} here is about 5066 a.u., which is only half of the saturation value of the *p*-shell (same adjustment). The excitation intensity for the saturation is much larger for the LO-phonon assisted transition than for the *p*-shell. At an excitation power of 0.07 a.u., the *p*-shell pumped PL is close to the saturation value (90%), whereas the LO-phonon pumped luminescence is still in the linear regime (40% of the saturation value).

In the case of the *p*-shell excitation, it was shown that the maximum intensity of the PL is determined by the total time of recombination and relaxation. In the high excitation power limit, the re-excitation takes place immediately after the recombination. For the case of LO-phonon assisted absorption, the maximum PL intensity is only half of the intensity of the *p*-shell pumped excitation (same experimental setup). This indicates

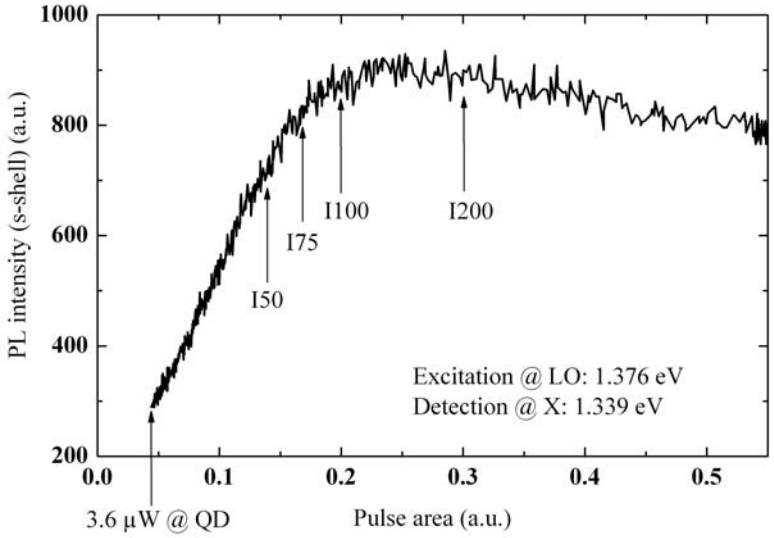

Figure 8.5: Pulsed excitation of the LO assisted absorption. No RABI-oscillations could be observed like in the *p*-shell. The signal seems to be over damped. The intensities values of I50, I75, I100, and I200 are shown, which are relevant in the following.

that the average time between two ground state emissions is twice as long in the LO-phonon case. But it is unlikely that the optical recombination time depends on the kind of excitation. More probable is the excitation of the biexciton in this case. If the QD is occupied with a single exciton, further excitation can take place in the case of LO assisted absorption. If the biexciton is generated too, the average time between two ground state recombinations is extended due to the (not detected) life time of the biexciton state. The biexciton excitation can be proven with a PLE measurement where the detection applies to the biexciton state, see chapter 9.

8.4 Pulsed excitation

The possibility of a coherent manipulation of a phonon assisted transition is a very interesting question, especially for a theoretical description. Is it possible to perform a stimulation of the combined exciton-phonon state after the excitation? In this section, a coherent manipulation of the LO-phonon assisted absorption is analyzed (similar to the *p*-shell, see figure 7.5).

Figure 8.5 shows the PL intensity of the ground state with increasing pulse area ($\sqrt{I}$), where I corresponds to the excitation intensity. For low excitation intensities, the PL intensity increases (quadratic, from 0 to 0.05 a.u.) and then switches to a linear increase with incident pulse area (up to 0.15 a.u.). At an intensity of more than 0.15 a.u., the PL intensity increases to a maximum followed by a slight decrease. The origin of this satu-

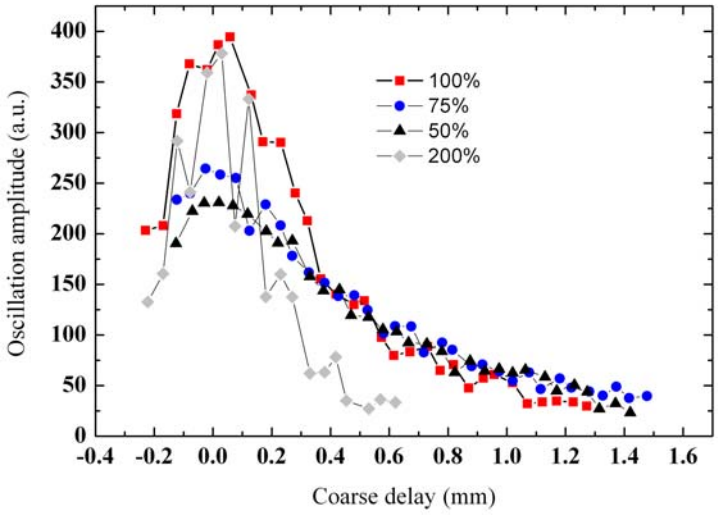

Figure 8.6: Power dependent dephasing analysis. The decrease of the interference amplitude with varying delay times is shown for different excitation intensities. The dephasing at an intensity of I200 shows a stronger decrease than the other excitation intensities.

ration behavior is not known up to now. A possible explanation of the missing coherence is for example the biexciton generation. Furthermore, the generated GaAs LO-phonons are able to propagate in the bulk GaAs crystal. Thus, the phase relation of the excitation and the combined exciton-phonon state is lost very fast. However, the PL signal shows only a strong damping and no coherent properties. But this is no sufficient evidence that a coherent manipulation is generally not possible with a LO-phonon assisted transition. The pulse length for excitation used here is about 1.7 ps. Shorter excitation pulses may be useful for a possible coherent control, but also unfavorable for this quantum system. The probability for the generation of the biexciton is strong enhanced for high excitation powers. But maybe much shorter excitation pulses could be helpful to observe a coherent behavior before the excitation intensity is high enough for the generation of the biexciton.

8.5 Dephasing of the LO-phonon assisted transition

In the previous sections, the dephasing of different QD states (*s*- and *p*-shell) was discussed which originates from tunneling, relaxation, and recombination processes. In the case of the LO-phonon assisted absorption, the dephasing mechanism is different. GaAs LO-phonons with an energy of 36 meV are generated in order to excite the exciton ground state. Since it is not possible to perform a coherent manipulation with ps laser pulses, one expects a very fast loss of the phase relation between the laser pulse and the LO-phonon assisted transition. In order to analyze this dephasing behavior, double pulse experi-

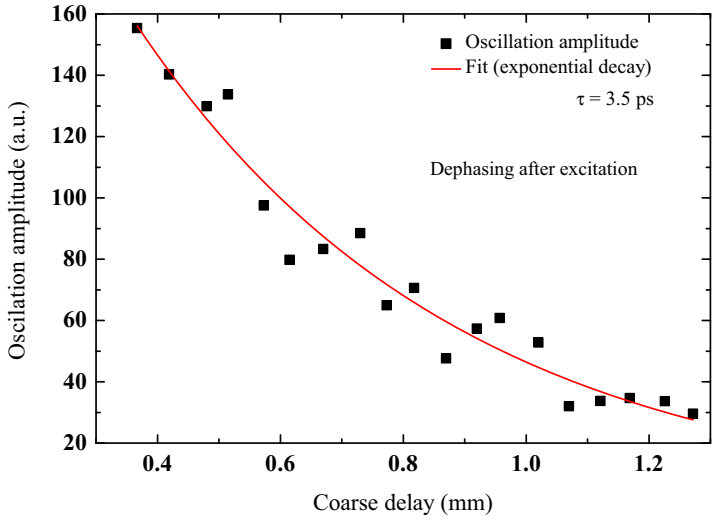

Figure 8.7: Dephasing analysis of the LO assisted absorption at an intensity of I100. The decrease of the interference amplitude is fitted by a normal exponential function. The PL signal at overlapping pulses is not considered.

ments have been performed. Due to the fact that no RABI-oscillations could be observed on this transition, it is not possible to define a π-pulse. Therefore the double pulse experiment is performed with a couple of selected excitation intensities. Here the excitation power for maximum PL intensity (0.2 a.u.)(see figure 8.5) is defined as intensity = 100 % (I100). The double pulse experiments are performed at excitation intensities of 50 %, 75 %, 100 %, and 200 %.

Figure 8.6 shows the oscillation amplitudes of the interference depending on the pulse delay for different excitation powers. One can see a fast decrease of the interference amplitude for all excitation intensities. The maximum intensity (zero time delay) increases with increasing excitation intensity as expected (up to 100% intensity). The decay of the oscillation amplitude is nearly the same for all excitation intensities $\leq$ 100 %. The excitation pulse length of 1.7 ps corresponds here to 0.25 mm pulse delay. For the case of an excitation amplitude of 200 %, one can observe a very fast dephasing of the system. In this case, the system is saturated already and therefore a faster dephasing for high excitation intensities is not surprising.

In order to determine the dephasing time of the system, the decay of the oscillation amplitude at an intensity of 100 % is analyzed in figure 8.7. The experimental data are fitted with a simple exponential decay function. For complete overlapping pulses, the two laser pulses will interfere with each other. For a correct analysis of the dephasing time, here only the data for delay times longer than the pulse length are considered. One can see a very fast dephasing of the system which is only 3.5 ps. This is only half of the dephasing time of the *p*-shell (6.02 ps).

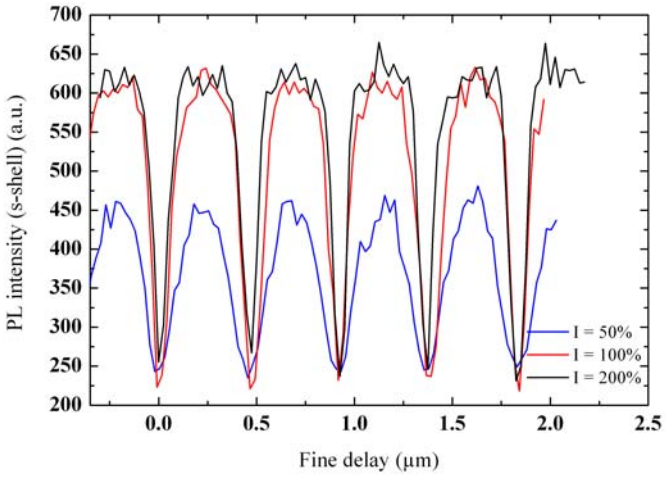

Figure 8.8: Interference pattern at double pulse excitation on resonance to the LO-assisted absorption at different excitation intensity. For higher excitation intensities, the interference pattern shows a variation from a symmetric oscillation. A plateau at high PL intensity with very small dips origins.

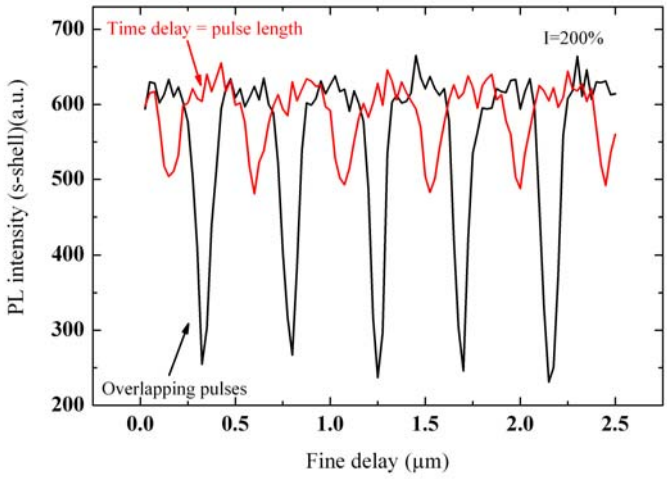

Figure 8.9: Comparison of the oscillation pattern of the PL at overlapping and time separated laser pulses. The oscillation amplitude is reduced, but the plateau is still visible. This effect is probable a result of excitation intensity which is also visible at time separated pulses.

If one takes a closer look at the shape of the oscillation pattern of the interference, one can observe some changes compared to the *p*-shell excitation. Figure 8.8 shows the oscillation of the ground state PL for different excitation amplitudes, 50 %, 100 %, and 200 %. In the case of 50 % excitation amplitude, the QD is still in the linear regime (see figure 8.5). Here, the PL intensity increases directly with the excitation intensity. The interference pattern is very symmetrical around its mean value (350 a.u.) (figure 8.8 blue line). For increasing excitation amplitudes (100 %), the oscillation amplitude increases as expected (Figure 8.8 red line). But here, the form of the interference oscillation has changed and is no longer symmetric around the mean value. At constructive interference, the PL builds up some kind of plateau. The PL shows "destructive interference" only in a smaller region of the fine delay. This effect develops even more at higher excitation amplitudes (see figure 8.8 black line for 200 % excitation amplitude). The plateau of the "high PL state" has developed even more, and the "dip" to the "low state" is even smaller. Thus, this change in the oscillation pattern becomes significant if the excitation intensity reaches saturation (see figure 8.5). The origin for this is effect is unknown up to now. The explanation of this effect may be possible with theoretical description and simulation. The group of J. FÖRSTNER has started to simulate the interaction of the LO-phonon and the exciton for this kind of systems. These results have to show whether pure LO-phonon interaction is responsible for this effect or if one has to take the biexciton state into account.

Figure 8.9 compares the oscillation pattern of the PL for overlapping and time separated (time delay = pulse length) pulses. Here the excitation amplitude is 200 %. One can see that the oscillation amplitude decreases due to the dephasing. But the oscillation pattern remains unsymmetric around the mean value with a plateau in the high state. Thus the change in the oscillation pattern is not an effect of overlapping pulses.

In summary, the LO-phonon assisted absorption has different properties compared to the *p*-shell:

- It is possible to saturate the LO-phonon assisted transition.
  - The excitation power needed for the saturation is much higher than the *p*-shell saturation intensity.
  - The saturation value is approximately half of the *p*-shell saturation. This indicates the excitation of the biexciton state.
- A coherent manipulation of the LO-phonon assisted absorption state is not possible with the used excitation conditions.
- The dephasing time of the LO-phonon state (3.5 ps) is faster than the dephasing due to relaxation (6.02 ps). High excitation intensities lead to enhanced dephasing rates.
- The interference pattern for double pulse excitation is different in the LO-phonon resonance as compared to the *p*-shell resonance.

9 Biexciton generation

In chapters 7 and 8, the coherent excitation of the p-shell and the LO-assisted absorption was discussed. The p-shell shows a clearly developed maximum of the RABI-oscillations, whereby a coherent manipulation of the LO-assisted absorption was not possible with the avaiable excitation condition. An additionally generated biexciton could lead to enhanced dephasing rates. Thus, it is possible that the LO phonon assisted absorption cannot be coherently manipulated due to the generation of the biexciton. This chapter discusses the possibilities of the biexciton generation with resonant excitation of higher QD-states.

9.1 Photoluminescence excitation of the biexciton

Figure 9.1 shows the PLE spectra for the biexciton state. The diagram shows the PL intensity of the biexciton state ($2X$) depending on the excitation energy. In order to compare this data with the PLE spectra from the ground state (see figure 5.5), the energy is directly plotted as energy difference with respect to the ground ($1X$). One can see that there are various possibilities to excite the biexciton. It has to be noticed that this experiment is not sensitive to the kind of excitation (resonant, half resonant, non-resonant/background). Every excitation which leads to the biexciton ground state is detected. Here one kind of excitation is a resonant two photon process in a higher state followed by a relaxation process into the biexciton ground state. It is also possible that the QD is only occupied with one exciton (e.g. after the biexciton decay process), and the second exciton is generated considering the renormalization energy. Please note that the excitation power is much higher as compared to figure 5.5 (700 μW before pellicle/30 μW at the sample). An identification of all these states is not easy.

The large peak 32 meV above the ground state could be the biexciton p-shell. Here it may be possible that both excitons are created in the p-shell by a two photon absorption process. Due to the renormalized energy, the resonance is shifted to a higher energy ($E_{2X_p} - E_{X_p} = 2.4$ meV). In this case the renormalization energy is positive. The phonon absorption peak here is again 36 meV above the ground state. One can clearly see that the biexciton can be generated by pumping the GaAs LO-phonon state. At the same excitation power, the biexciton PL intensity (at ground state X_p-state) is much lower (only 1/6). Therefore it is sure that the biexciton can be generated by pumping the LO phonon state (which is also demonstrated in [FZBA00]). If the QD is already excited by one exciton, further absorption can take place. This could explain the fact that the PL saturation value of the LO phonon state is much lower than the p-shell.

A model for sequential phonon assisted generation of a biexciton in the QD and the sequential decay is discussed in the following: At the resonant laser energy ($E_{X_{LO}}$), an

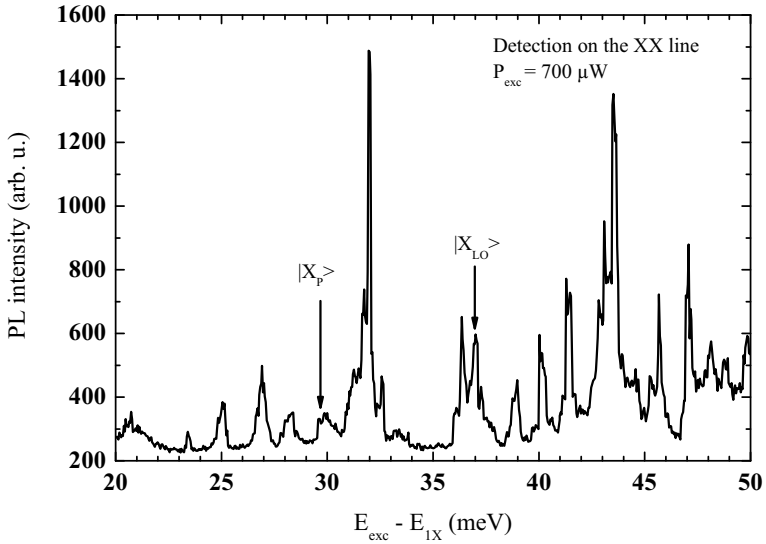

Figure 9.1: Photoluminescence intensity of the biexciton transition with varying excitation energy. One can see that the biexciton can be created with many different laser energies. The highest peak here is probably the biexcition p-shell, which is excited by two-photon absorption process. The biexciton generation is more probable at LO-phonon excitation than at p-shell excitation.

exciton in the QD and a phonon with energy E_{LO} are generated. As long as the dot is occupied with one exciton, this transition is renormalized by the amount of the biexciton binding energy and hence blocked for further absorption at the excitation energy of $E_{X_{LO}}$. However, for unchanged excitation energy, a second exciton can be generated by absorption under participation of a different phonon with energy $E_{X_{LO}+\Delta E_{2X}}$. This second absorption process is made possible by the weak background absorption. Each absorption process leading from the single to the two exciton state can contribute here and does not have to be generally phonon assisted. Otherwise it is also possible that the second absorption takes place assisted by two phonons (optical and acoustical), even if the probability is low.

9.2 s-shell luminescence for biexciton excitation in the p-shell

Figure 9.2 shows the s-shell luminescence of the single QD for biexciton p-shell excitation. Please note that the detection setup is similar to the PLE-measurements. This means that the luminescence intensities for all detected states are not comparable due to the additionally installed grating before the spectrometer. The energy detection window is limited by the spectrometer entrance slit and the intensity function of the blazed grating. Thus, it is not ensured that all s-shell states can be detected. Only the states near the the ground state ± 3 meV are detected at the same time. A luminescence of more s-shell states

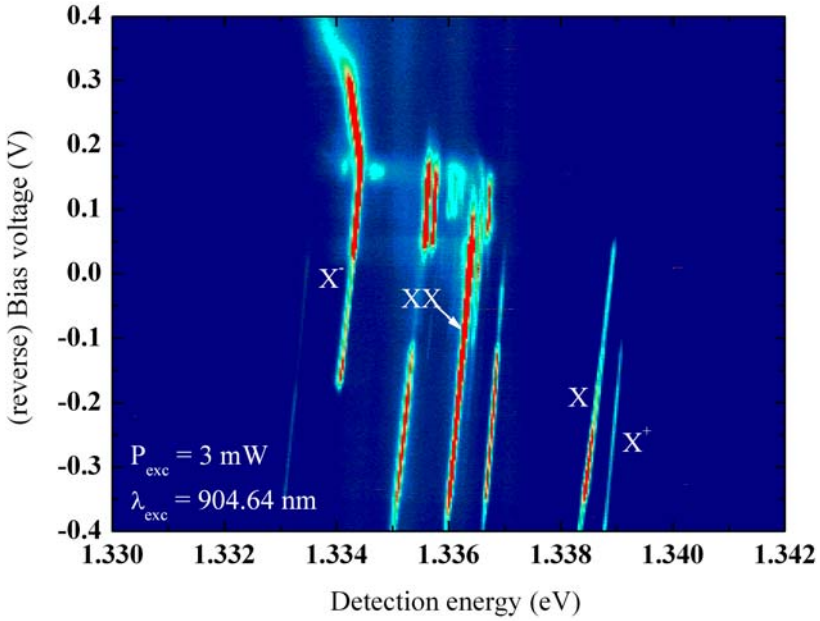

Figure 9.2: *s*-shell luminescence at a strong excitation of biexciton *p*-shell. At least two charge carriers (one electron and one hole) must relax into the *s*-shell for the recombination. There are different possibilities for the other two charge carriers. All configurations lead to different renormalization energies. Each state shows a different STARK shift.

outside this window is excluded by random measurements with different adjustments of the blazed grating. One can observe some additional states, if the PL is compared to the normal non-resonant interband excitation PL, see figure 5.1. The excitation of the biexciton state always needs a higher excitation intensity, therefore the excitation power here is about 3 mW (120 μW at the sample).

There are different recombination schemes which are all separated by different renormalization energies. The excitation probably takes place by a two photon absorption process in the *p*-shell. Thus, the generation scheme starts with two excitons in the *p*-state. The detection takes place in the *s*-shell luminescence. The recombination luminescence is detected from the electrons and holes which have already relaxed into the *s*-shell. All direct *p*-shell transitions are separated in energy and cannot be detected here. There are multiple possibilities for recombination configurations, e.g. only three (of four) charge carriers have relaxed into the ground state. An assignment of all these transitions in figure 9.2 is hardly possible.

10 Single photon emission

Since the experimental setup allows for electrical and optical detection, it is possible to operate the single QD as a single photon emitter. Single quantum systems are often the basis for good single photon emitters. In this dissertation, the advantage of coherent state preparation as compared to the commonly used non-resonant interband excitation is presented. The main advantage of using a coherent manipulation of a higher QD state for excitation is the defined occupation of the QD with a single exciton.

In the present work, two possibilities for the occupation of the QD with a single exciton in the ground state are presented: The first option uses an excited state excitation, followed by a relaxation process into the ground state. The second option uses phonon assisted absorption to create the desired ground state occupation. In both cases, excitation and recombination are separated in energy. Finally, the recombination process from the ground state will generate the desired single photon.

10.1 First and second order correlation function

The correlation of light is usually described by means of coherence. This corresponds to the amplitude and the phase characteristics of an electromagnetic field. An example for this is the well known experiment of the YOUNG double-slit. The interference and the contrast results from the first order correlation function which is defined on the basis of the *E*-field. The first order correlation function is represented as *spatial* or as *temporal* correlation. The spatial correlation function in the first oder $g^{(1)}(\vec{r_1}, \vec{r_2})$ is defined as:

$$g^{(1)}(\vec{r_1}, \vec{r_2}) = \frac{\langle U_1(\vec{r_1}, t) U_2^*(\vec{r_2}, t) \rangle}{(I(\vec{r_1}) I(\vec{r_2}))^{1/2}}.$$

The temporal first order correlation function $g^{(1)}(\tau)$ is defined as:

$$g^{(1)}(\tau) = \frac{\langle U(t) U^*(t+\tau) \rangle}{\langle U(t) \rangle \langle U^*(t+\tau) \rangle}$$

where U and U^* are correlated to the *E*-field of the electromagnetic field. For example, a light beam is split into two parts, and one part has to go a longer path length. Then the coherence time can be analyzed in the loss of interference.

The photon statistics reveals whether a given light field originates from a classical or a quantum source, such as a single quantum system. These sources can be distinguished by their intensity correlation function, $g^{(2)}$. The second order correlation function gives the probability that a photon is detected at a time t and another photon at the time $(t + \tau)$.

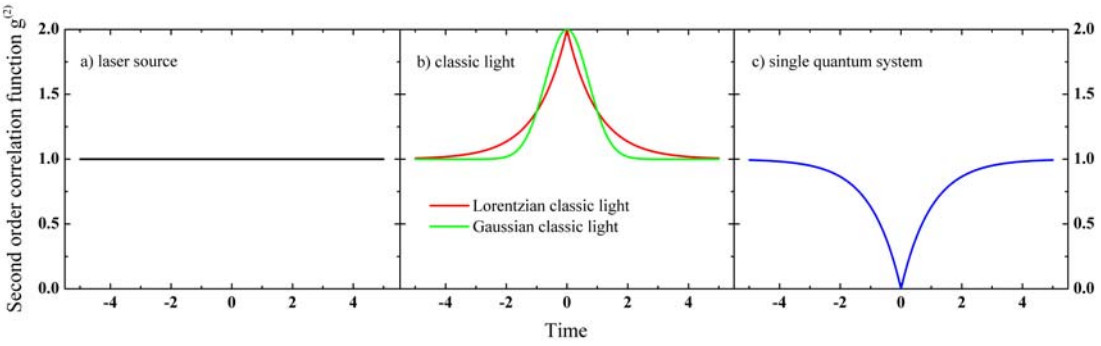

Figure 10.1: Second order correlation function of a) laser light, b) classic light, and c) a single quantum system

The second order correlation function $g^{(2)}(\tau)$ is given by the normalized convolution

$$g^{(2)}(\tau) = \frac{\langle I(t)I(t+\tau)\rangle}{\langle I(t)\rangle \langle I(t+\tau)\rangle} \tag{10.1}$$

where $I(t)$ corresponds to the emission intensity [ZBJ+01]. The second order correlation function is measured in the HANBURY-BROWN and TWISS setup (presented in chapter 4.3.4) in a photon counting experiment. The luminescence, which has to be tested for correlation, is split up into two parts. Each part is detected by a single photon counter device (avalanche photo diode (APD)). A single photon counting event of the first device starts a time measurement (done by time to amplitude converter), a single photon detection at the second device stops the time measurement. The time between the two photon counting events is the time interval τ. The measurement of many of these correlation events results in a histogram which corresponds to the second order correlation function. A single photon can only be detected at one counter. For the case of a single photon emitter, the two APDs cannot count photon events at the same time.

10.2 Correlation functions of laser, classic light, and quantum-mechanical light

Each given light source has its own characteristic second order correlation function. For example, laser radiation exhibits constant $g^{(2)}$ over time. The probability for photon detection is constant in time. Thus, the correlation event rate depends not on the time delay τ. The normalized second order correlation function is equal to one, see figure 10.1 a). The second example, a light bulb, has a different correlation function. The photon emission of such a thermal light source shows strong fluctuations of the photon emission rate (classic light). The probability for two detection events is not constant in time, it is higher for short time intervals. For this case, the equation $g^{(2)}(0) \geq g^{(2)}(\tau)$ is valid. Figure 10.1 b) shows the two cases of LORENTZIAN (red) and GAUSSIAN (green) classic light. The classic light is said to be *bunched*. Classical light fulfills the CAUCHY-SCHWARZ

inequality, $g^{(2)}(0) \geq g^{(2)}(\tau)$. On the other hand, light that violates this inequality is characteristic for a single quantum emitter. If a local minimum is found at $t = 0$, i.e. $g^{(2)}(0) < g^{(2)}(\tau)$, this light is said to be *antibunched*, which results in a dip in the correlation function, see figure 10.1 c). In this case, the probability for two photon detection events close in the time domain is low. For a single photon emission device, $g^{(2)}(0)$ is ideally zero.

10.3 Correlation function of a single photon emitter

If the luminescence consists only of single photons, the histogram must show a clear reduction at zero time delay. The dip (cw-case) in the histogram is an effect of the *antibunching*. This indicates a luminescent source as a single photon emitter. In order to reach a symmetrical histogram, one electrical connection from the APD to the time to amplitude converter contains is subjected to a time delay. This only shifts the detection window to negative times.

Under continuous excitation, a single quantum emitter would generate a dip in the histogram at zero delay time ($\tau = 0$). This means that the quantum system, that generates the luminescence, must be re-excited after emission before a second photon can be emitted. For long time delays, the histogram is constant, just as in the case of a constant photon emission rate (see figure 10.1 c)). This is illustrated in figure 10.2 a). Ideally, the exponential decay constant τ corresponds to the systems life time of the quantum system.

$$g^{(2)}(t) = 1 - \left(1 - g^{(2)}(0)\right) \cdot \exp\left(\frac{-|t|}{\tau}\right) \tag{10.2}$$

Contrary to the *antibunching* effect, there can be also *bunching* effects ($g^{(2)}(0) \geq g^{(2)}(\tau)$). For example, a single laser pulse consists of many photons within one pulse. It is therefore possible to count photon events on both APDs within one pulse. Furthermore, correlations can be measured between two different pulses. This results in a periodic structure of the measured histogram with a time constant of the delay time between two pulses. This is illustrated in figure 10.2 b). The correlation function of pulsed laser consists of a series of peaks, separated by the repetition time between two laser pulses (T_{rep}). Without any time jitter of the APDs, the width of these peaks are correlated to the pulse width of the laser (2-3 ps). The theoretical correlation function of the pulsed laser is a convolution (see 10.1) of the auto correlation function

$$I_{pulsed} = \sum_n \frac{I_0}{\tau_{pulse}\sqrt{2\pi}} \exp\left(\frac{-(t - nT_{rep})^2}{2\tau_{pulse}^2}\right). \tag{10.3}$$

This again results in a repetitive structure of the correlation function.

If the single quantum system is excited by a pulsed laser, the luminescence only consists of single photons separated in time by T_{rep} and the variation due to the statistical recombination time. The histogram will again show different peaks with a time delay of the inverse repetition frequency (12.5 ns). The peak at zero delay time will vanish due to the single photon emission. This is shown in figure 10.2 c). It is very complex to derive

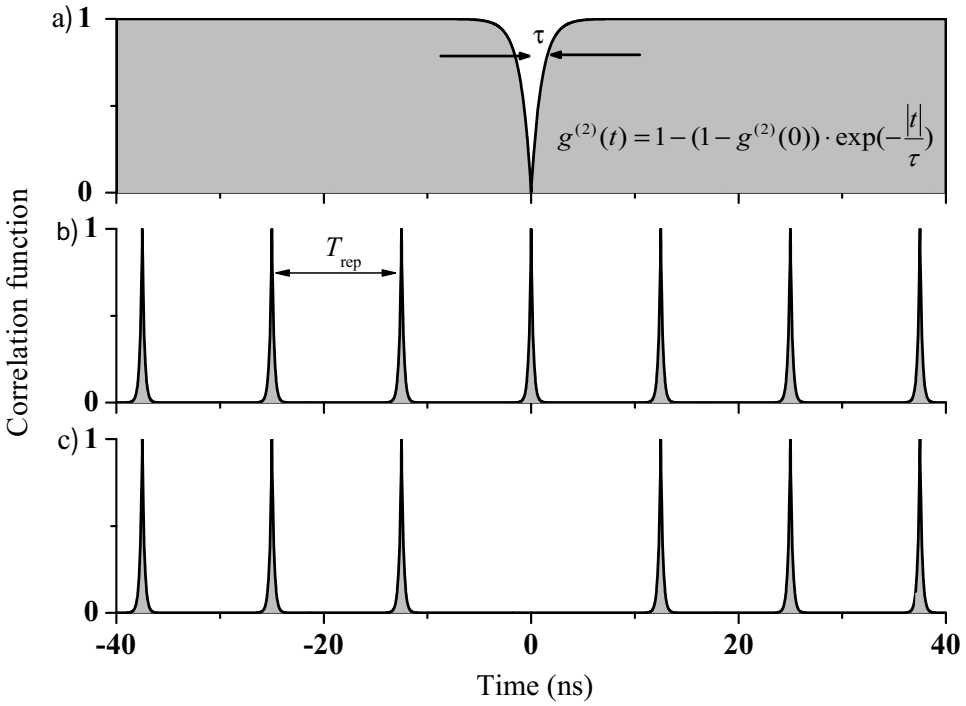

Figure 10.2: Theoretic histogram of the time to amplitude converter (corresponds to the second order correlation function). a) Antibunching at continuous excitation of the single photon emitter. The dip in the histogram is an exponential function in time and is correlated to the life time of the quantum system. b) Correlation of a pulsed laser. The peaks are separated in time due to the repetition frequency of the excitation laser. c) Perfect clean single photon emission. The central peak of the repetitive structure is missing completely.

an analytical function of $g^{(2)}$ of the single photon emission for pulsed excitation. Ideally, there is only a single photon in each pulse. Therefore the time dependent function for the single photon intensity can only give a probability of the emission. In principle, this function depends on the excitation pulse function, the generation probability and on the exponential decay. In the HBT setup, the luminescence is split into two parts. But a single photon cannot be split up. That's why a convolution of the time dependent single photon emission probability would not lead to the correct results. Therefore it is not possible to give an analytical function for the convolution like it is possible in the case b) (correlation of pulsed laser light).

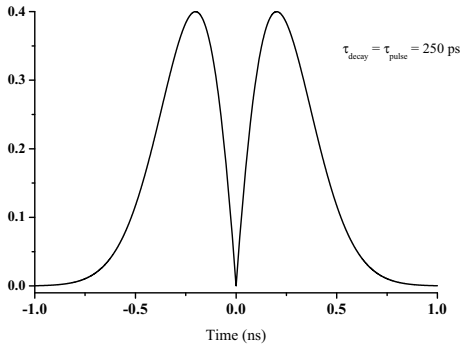

Figure 10.3: Illustration for the histogram for single photon emission for same time constants for excitation and decay. See text for a detailed description.

10.4 Sequential absorption-emission events within one excitation pulse

Up to now, only the ideal case of the single photon emission is discussed, where the decay time of the quantum state is much longer than the pulse duration for excitation and much shorter than the repetition time of the excitation laser. A problem can arise here if the pulse width of the excitation laser has the same order of magnitude as the decay time of the quantum system. Then it is possible that more than one absorption and decay processes take place within one excitation pulse. Thus, the resulting correlation function should show two symmetrical peaks as illustrated in figure 10.3. Here, the case of equal time constants for decay and excitation is assumed. At zero time delay, there is a still a dip in the correlation due to the single photon emission. But after the decay process, a following (second) single photon emission can take place.

In the case of non-resonant interband excitation, one needs strong excitation intensity in order to avoid the case missing excitation. Due to the POISSON-distribution, there is a non-negligible probability for the excitation of more than one exciton. An excitation of two excitons, before the first recombination takes place, leads to the sequential decay of the biexciton and exciton. The luminescence of the biexciton is separated in energy. It is also possible that a second exciton is generated after the first recombination process (within a single excitation pulse). This would lead to a second single photon within one pulse.

An analytical derivation of this content is very complex. The time dependent probabilities of of the first single photon emission and the sequential (second) single photon emission have be convoluted. But the time dependent single photon emission probability is furthermore a convolution of the laser excitation and the decay function. In principle, one has to calculate the time dependent probability of the first and the second photon after the laser pulse.

In order to illustrate the effect of equal time constants for excitation and decay, the correlation function of the single photon emission 10.2 (which is seen as the response of

the system) is multiplied with the central pulse ($n = 0$) of the excitation function 10.3. The multiplication of excitation and system response formula only gives an illustration for behavior of equal time constants for excitation and emission. In this case, the central peak is strongly reduced but is not completely vanished. The height and the width of the central peak is then only determined by the two parameters τ_{decay} and τ_{pulse}. This effect exceeds for short decay times. The second order correlation function will show two peaks which are symmetric around zero time delay. If one regards the time jitter of the APDs, the dip in the middle of the structure in figure 10.3 could be washed out. Thus, the single photon emission appears to be unclean.

This problem can generally be avoided by a coherent excitation of an excited state of the single quantum system. By using a coherent manipulation of the first excited state of the single quantum system, one can avoid a second excitation-emission process. Thus, the effect of an unclean histogram of the single photon emission at short decay times should be of no significance here. The excitation scheme for the single photon emission is discussed in chapter 10.

10.5 Continuous non-resonant interband excitation

Single photon emission from semiconductor QDs was first reported by MICHLER et al. [MKB$^+$00], followed by many other groups. These groups employed optical as well as electrical pumping. The general concept of the so far employed excitation scheme is based on strong incoherent, non-resonant excitation and a sequential decay cascade with final single photon emission. Using this excitation scheme, an interaction between an exciton and other charge carriers cannot be excluded. The different renormalization energies of the various multi-exciton states allow for spectral isolation of the last photon emitted from the previous decay process of the multiexcitonic state. The last exciton is located in the ground state of the QD. It cannot be guaranteed that the luminescence of the last exciton is clearly separated in energy from a multiexcitonic state. It is possible that higher multiexciton states have an spectral overlap with the ground state luminescence. Therefore, the requirements for the energy separation are quite big. A strong excitation is necessary to avoid the case of missing population (within the statistical fluctuation of the created exciton number for this incoherent process).

For the analysis of the single photon emission of the ground state, a photon correlation measurement is performed under the condition of continuous non-resonant interband excitation. The time correlation measurement is performed by a time to amplitude converter with a resolution of 300 ps. For a clean single photon emission, one would only expect a dip in the histogram. A perfect clean single photon emission would lead to vanishing correlation counts at zero delay time. The result of this measurement is shown in figure 10.4. For low excitation intensity, the counting rate and the correlation event rate are very low. Here, even an integration time of 10 h would not lead to usable results. For extremely high excitation intensities (non-resonant and interband), the linewidth of the luminescence is broadened due to the interaction of the QDs exciton with other excited charge carriers. With increasing excitation intensity, one gets a saturation of the single ground state exciton and an increase of the biexciton luminescence. The excitation inten-

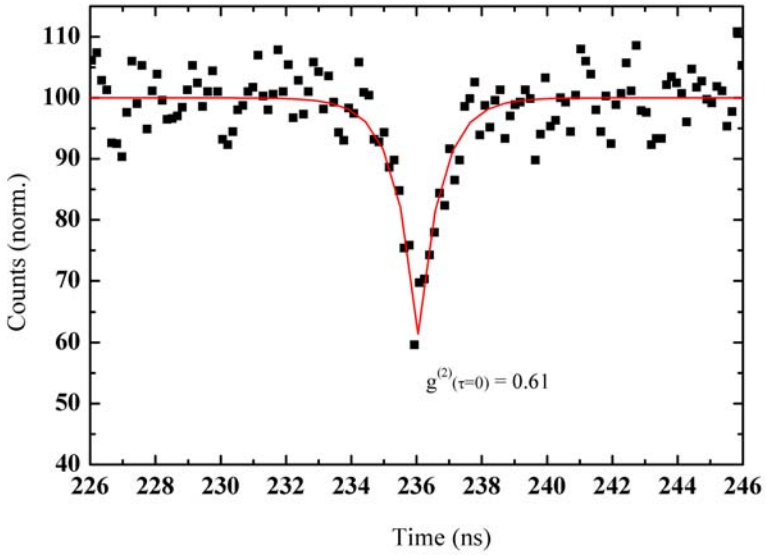

Figure 10.4: Photon correlation measurement after interband excitation at ground state detection. The correlations are fitted with the formula for an exponential ground state decay, see text.

sity in this case is adjusted near to the saturation level of the ground state luminescence. The correlation counts are normalized to the value 100. The second order correlation function $g^{(2)}$ in the middle of the histogram has a value of $g^{(2)}(t_0) = 0.61$.

The dip in the middle of the histogram is fitted by the formula 10.2 $g^{(2)}(t) = 100 - \left(1 - g^{(2)}(t_0)\right) \cdot exp(\frac{-|t-t_0|}{t_c})$ where $g^{(2)}(t_0)$ corresponds to the minimum correlation value and t_c to the decay time of the dip. The formula is the result of the exponential decay of the QD state in time. Unfortunately, it is very difficult to determine a possible background. An background could arise from the avalanche breakdown flash (discussed in chapter 4.3.4) or from the time jitter of the APDs. The exponential decay is not influenced by a constant background. But the effect of the time jitter of the APD is different. For example, a correlation measurement of the pulsed laser leads to repetitive peak structure in the histogram (without antibunching). Ideally, the peak width would be correlated to the laser pulse length (2-3 ps). But the resulting peaks are broadened due to the time jitter of the APD (approximately 300 ps). The measurements of a single photon emission (cw) are similarly affected by the APD time jitter. The resulting dip of the correlation measurement is then less pronounced. Therefore, the results of the fitcurve of the histogram are only an upper limit for the ground state decay time.

Furthermore, the decay time of this exponential function is the time between two recombination processes. The time for a re-occupation of the ground state after the recombination process is assumed to be negligibly short. As a result of the fitcurve, the upper limit for the ground state decay time τ is approximately 700 ps. Here the second

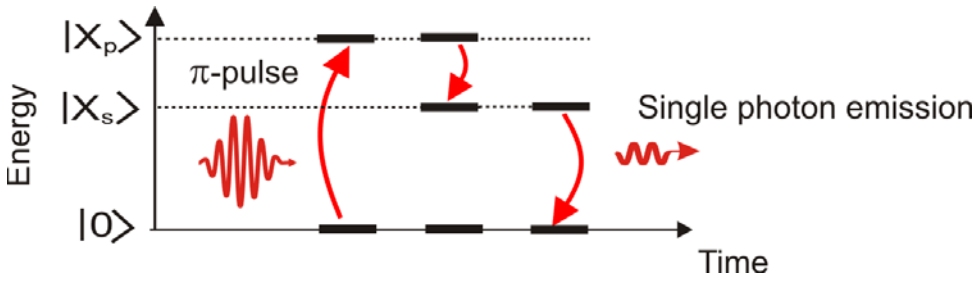

Figure 10.5: Scheme for single photon emission. The excitation takes place in the p-shell with a π-pulse. After the relaxation process into the ground state a single photon can be emitted. (published in [ELdV+07b, ELdV+07a])

order correlation function for continuous excitation is $g^{(2)}(0) = 0.61$. Even if the two background effects are considered, this doesn't accord to a clean single photon emission.

10.6 Single photon emission after coherent (p-)state preparation

In contrast to the commonly used non-resonant interband excitation, the coherent state preparation allows for the generation of a defined optical polarization, which, in case of π-pulse excitation, results, after the projection, in a single exciton occupancy. The coherent manipulation of the single exciton ground state works very well, see chapter 6.3.1, but cannot be applied here due to the spectral overlap of ps-excitation and single photon emission. In order to spectrally separate the emission from the ps-excitation, RABI-flopping is performed in the p-shell with subsequent relaxation to the ground state, followed by single photon emission. The possibility of a coherent state preparation of the first excited state is shown in chapter 7.4.

The basic sequence of the concept for a defined single photon emission is sketched in figure 10.5. After the coherent excitation of the p-shell ($|X_p\rangle$) via a π-pulse, the generated exciton relaxes into the ground state ($|X_s\rangle$) and subsequently decays by spontaneous emission. The main advantage of this concept is the defined excitation of a single exciton in a coherent process. There is no interaction with other excited charge carriers. The luminescence must only be filtered from the excitation laser and not from the luminescence of any multiexcitonic state. The pulsed excitation, combined with the coherent state manipulation, minimizes the possibility of two following excitation and recombination processes, which is discussed in before 10.1.

The coherent state preparation uses laser pulses which lead to a recurring pattern of peaks in the histogram. Each photon detected can be correlated with a photon generated from one of the next laser pulses. Due to the coherent excitation, there is at most one photon for each laser pulse. Therefore, there cannot be a correlation at zero delay time. Single photon emission will lead to a missing peak at zero delay time; $g^{(2)}(\tau = 0)$ should vanish. Figure 10.6 shows the result of the correlation measurements with an integration time of 10 h and a time resolution of 300 ps. The correlation peaks have a time interval of 12.5 ns (80 MHz laser repetition frequency). The numbers printed above the peaks cor-

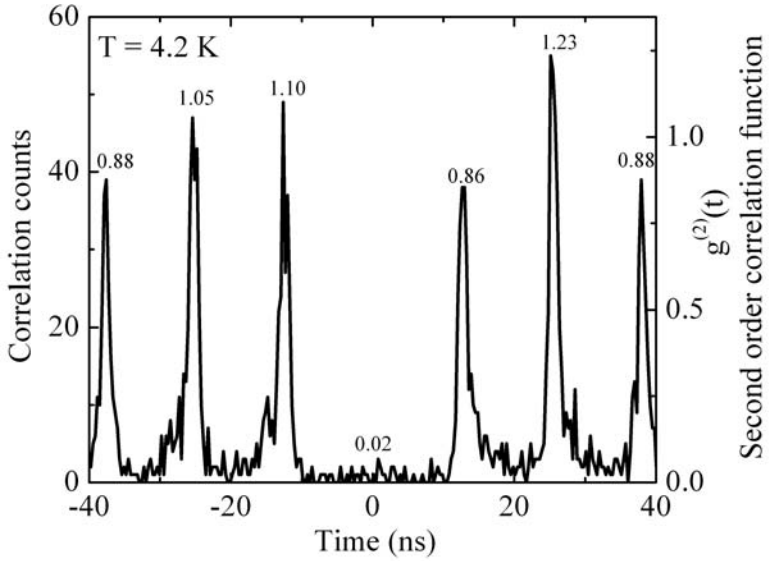

Figure 10.6: Photon correlation measurement under the condition of π-pulse excitation in the p-shell (10 h integration time). The numbers printed above the peaks give the value of the normalized correlation function. The central peak of the periodic pattern ($\tau = 0$) is strongly suppressed, which proves clean single photon emission. (published in [ELdV$^+$07b, ELdV$^+$07a])

respond to the normalized second order correlation function $g^{(2)}(\tau)$, whereby $g^{(2)} = 1$ corresponds to the average peak height. The peak at zero delay time is basically missing, which proves that this excitation scheme results in fact a very defined single photon emission. Also quantitatively, the single photon emission of a QD under coherent p-shell excitation appears remarkably clean ($g^{(2)}(0) \leq 0.02$).

10.7 Single photon emission after GaAs LO-phonon assisted absorption

Another possibility for a defined single photon emission is sketched in figure 10.7. Here the excitation is performed using the GaAs LO-phonon assisted absorption. The LO-phonon assisted resonance is separated by 7 meV from the p-shell absorption, see figure 5.5. Due to the non-coherent properties of the LO-phonon absorption (see figure 8.5), it is not possible to define a π-pulse in this excitation scheme. Thus it is not possible to declare the occupation probability for the excited exciton. The excitation amplitude for the photon correlation measurement used here is I100, see figure 8.5. It has to be noticed that the generation of a second exciton is possible with the LO-phonon state (see chapter 9). But the luminescence of the biexciton state is spectrally filtered. The result of the

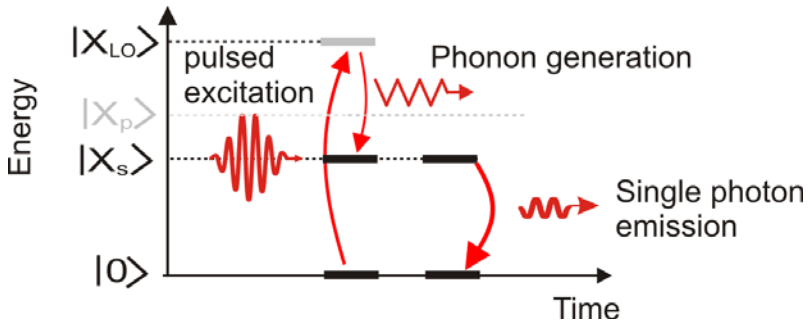

Figure 10.7: Scheme for single photon emission after photon assisted absorption. The excitation energy fits to the ground state energy plus the energy of a GaAs LO-phonon. The ground state is thereby generated with the help of an emitted GaAs-LO phonon. The ground state is again able to decay by optical recombination and thus the desired single photon is generated.

photon correlation measurement using LO-phonon absorption is shown in figure 10.8.

The pulsed excitation leads again to a recurring pattern of peaks. The correlation peaks also have a time interval of 12.5 ns (80 MHz laser repetition frequency). The peak at zero delay time is basically missing again, which proves that this kind of excitation leads also to a clean single photon emission. The single photon emission of a QD ground state appears surprisingly clean ($g^{(2)}(0) \leq 0.04$). Comparing the two excitation schemes of p-shell and LO-assisted absorption, one can say that both kinds lead to a very clean single photon emission.

In conclusion, the coherent p-state excitation scheme has the following advantages (compared to LO-phonon and non-resonant interband excitation):

- Defined excitation of a single exciton in a coherent process; optimum probability for the excitation of a single exciton.
- No multiple absorption/emission events within a single pulse; clean single photon emission in the time domain.
- In principle, no spectral overlap of the single photon emission with a multiexciton decay; clean single photon emission in the energy domain.
- No interaction with other excited charge carriers.

10.8 Single photon emission devices

There are different possibilities for improvements of the single photon emission, when one wants to build a single photon emitter device. In this work, the proof of the systematic excitation scheme for a very clean single photon emission is demonstrated. The single photon emission is very clean in the time and energy domains.

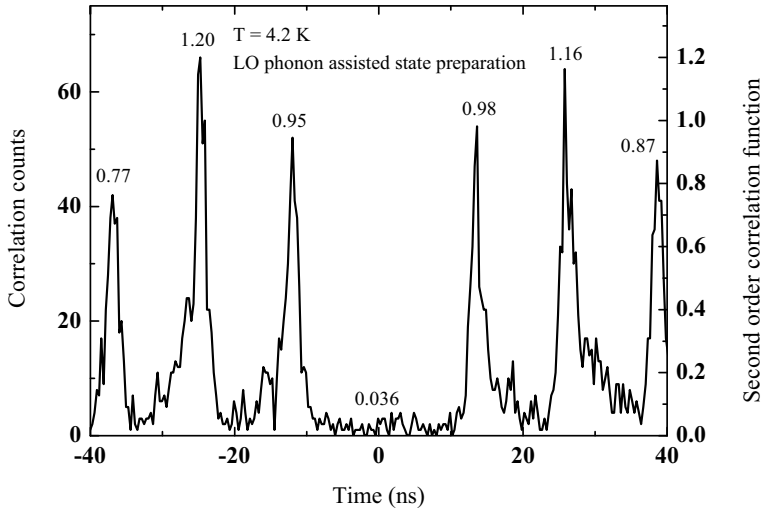

Figure 10.8: Photon correlation measurement under the condition of excitation in LO-phonon assisted absorption resonance (10 h integration time). The central peak of the periodic pattern ($\tau = 0$) is strongly suppressed, which proves clean single photon emission.

The next step for the development of a single photon emitter device is the integration of a single QD into an optical resonator structure, where this excitation scheme can be applied. This is possible, for example, with a distributed BRAGG reflector (DBR) in a pillar microcavity. If the QDs are integrated in a planar dielectric microcavity, the emission properties are modified. Spontaneous emission in the normal direction is enhanced if the cavity is resonant to the emission. The QDs must be located at an antinode position of the cavity field. The cavity thickness must correspond to the wavelength at the cavity resonance. If there is no coupling to other modes, the spontaneous emission is inhibited (the cavity is off-resonant). Due to the enhanced emission coupling into a single cavity mode, the spontaneous emission will have a good directionality, which makes an out-coupling more easily. The isolation of a single QD can be done by electron-beam lithography and reactive ion etching. The so produced mircoposts exhibit sinlge QDs. The fabrication of InAs quantum dots in AlAs/GaAs DBR pillar microcavities is shown by B. ZHANG in the group of Y. YAMAMOTO in [ZSP+05].

Without using a microcavity structure the output count rate can be enhanced by using an objective with a higher numerical aperture and/or with an additional lens on the surface. The semitransparent top (SCHOTTKY-) gate can be omitted as well as the near field shadow mask (if the QD density is low enough). The relaxation and recombination process requires a time of less than 1 ns. Thus, the excitation frequency could be enhanced by a factor of ten (now 80 MHz).

11 Conclusion and outlook

Single quantum dots are very interesting systems for experimental as well as theoretical research. The field of single quantum dot spectroscopy is a very fast growing and dynamic field, where fundamental and applied research are combined with material science.

In this work, the dephasing properties of different transitions of a single quantum dot have been analyzed. The isolation of a single quantum dot allowed for an analysis of various dephasing mechanisms of a confined electron hole pair. The dephasing of the p-shell transition is mainly determined by a relaxation process into the ground state, followed by an optical recombination process. The excitation of a quantum dot using GaAs LO-phonon assisted absorption also results in a ground state exciton. The dephasing of this transition is much faster than the p-shell transition. Due to the integration of a quantum dot-layer into a diode structure it became possible to apply an internal electric field perpendicular to the quantum dot. The resonantly excited ground state exciton is then also able to decay by a tunneling process. In this case, the dephasing of the ground state transition could be controlled via the applied bias voltage. These dephasing mechanisms exhibit specific time scales which are important for different applications quantum dots.

The possibility of coherent manipulations of single quantum dot-states is thereby the basis for versatile applications. Coherent investigations of semiconductor quantum dots (as well as implementations in the field of quantum information processing) are still at the very beginning of their development. In view of quantum computing, the challenges are extremely high, so the question of an actual future feasibility can still not be answered. The great interest in this new type of material system is certainly motivated by the fact that any research here is based on fundamental quantum effects and the progress in this field leads to a completely new technology.

One application based on a coherent property of a single quantum system is single photon emission. The possibility of a coherent manipulation of the p-shell is thereby the basis for a novel excitation scheme for single photon emission. It has been shown that the first excited state can be coherently manipulated analogous to the ground state. Due to the defined excitation of a single exciton in the p-shell, the resulting single photon emission (after the relaxation and recombination process) appears remarkably clean, which was demonstrated in a very clean way in this work. The generation of exactly one exciton in a quantum dot using a single laser pulse is well controllable.

The main challenges for future applications are now an adapted sample design and the manufacturing of appropriate samples and components. For example, the integration of quantum dots into a micro-resonator allows for an efficient and highly directive emission. Furthermore it is possible to influence properties like the optical recombination time with a micro-resonator.

Other material systems are also very interesting for single photon emission. CdSe/ZnSe quantum dots exhibit a higher band gap and deeper confinement potential which results in a higher shell energy separation. With suitable excitation, the CdSe/ZnSe quantum dots can be used for single photon emission in the visible. Further research on single photon emitters will concentrate on material systems which allow for an operation at room temperature.

For an application in the field of quantum computing (as well as for fundamental research), the coupling of two or more quantum dots is necessary but also challenging. For reasons of scalability, a coupling of several quantum dots in a defined lateral arrangement is very promising. For this proposes, a defined and localized quantum dot growth is necessary. First results have been reported by the groups of REUTER and SCHMIDT (reference [MRM+07] and [KRS05]). They recently processed areas on a substrate where the quantum dot position is controlled. Possible coupling-mechanisms are, for example, COULOMB interactions or interactions through an optically induced dynamic dipole moment (FÖRSTER coupling).

The approach of an electrically tunable quantum system, as shown in this thesis, is in this context a very promising opportunity. Independent from the experimental realization, there is always the problem that in particular systems with very weak coupling to the environment show long coherence times. Conversely, due to the small interaction strength, these systems can only be very slowly initialized, manipulated, and read out (for example nuclear spins). Electrically contacted quantum dots offer the interesting property that the tunneling time can be varied simply by a voltage change. By using a time dependent bias voltage, the initialization and the read-out process can be decoupled from normal dephasing.

In summary, there are many theoretical concepts for quantum dot applications today. Their experimental implementation is scientifically very interesting, but from a technological perspective also often extremely challenging. The combination of a single quantum system with electric access, as presented in this work, opens up many new concepts and applications for semiconductor based quantum optics and coherent opto-electronics.

Symbols and abbreviations

δ	detuning between laser energy and QD-resonance ($\delta = \omega_{Laser} - \omega_{QD}$)
φ	phase angle (angle in the u-v-plane of the BLOCH-sphere)
Γ	linewidth
Γ_0	natural linewidth
λ	wavelength
$\vec{\mu}$	dipole moment
θ	pulse area
$\sigma^{\pm}$	circular polarization
τ	time scale, e.g. tunnel time, pulse length, decay time, etc.
ω	angular frequency of the laser radiation or the optical transition
Ω, Ω_0	RABI-frequency (on resonance)
ψ	wave function
$1X$	single exciton
$1X^-$	negative charged exciton
$1X^+$	positive charged exciton
$2X$	biexciton
A_{10}	EINSTEIN-coefficient for spontaneous emission
AFM	atomic force microscope
B_{01}	EINSTEIN-coefficient resonant absorption

B_{10}	EINSTEIN-coefficient stimulated emission
cw	continuous excitation (continuous wave)
e	elementary charge ($1,6022 \cdot 10^{-19}$ C)
e^-	electron
E, ΔE	energy (difference)
$\vec{F}$	electric field
f_{Laser}	repetition frequency of the laser (80 MHz)
FWHM	full width half maximum
GVD	group velocity dispersion
h	PLANCK's constant ($4,1357 \cdot 10^{-15}$ eVs)
$\hbar$	$h/2\pi$ ($6,5821 \cdot 10^{-16}$ eVs)
hh	heavy hole
I	current
I_{sat}	saturation current
J, J_z	total angular momentum (z-component)
MBE	molecular beam epitaxy
l	angular momentum (orbit)
N_1	occupation probability of the $1X$-state
NA	numerical aperture
P	(optical) excitation intensity
$\widetilde{P}$	standardized excitation intensity
PL	photoluminescence (spectroscopy)
PLE	photoluminescence-excitation (spectroscopy)
QCSE	quantum confined STARK effect

QD	quantum dot
S, S_z	spin (z-component)
t	time
T	time period
T_1	life time
T_2	dephasing time
T_2^*	time scale of pure dephasing (no life time induced dephasing)
TEM	transmission electron microscope
u	dispersive component of the BLOCH-vector
v	absorptive component of the BLOCH-vector
V_B	bias voltage of the photo diode
w	occupation component of the BLOCH-vector
WL	wetting layer
X	neutral uncharged ground state exciton
$2X$	biexciton (neutral, uncharged, ground state)
X^-	single charged exciton
X_p	neutral exciton in the first excited state (p-shell)
X_{LO}	ground state exciton, generated by means of an GaAs-LO-phonon

Bibliography

[ABH+01] G. Alber, T. Beth, M. Horodecki, P. Horodecki, R. Horodecki, M. Rötteler, H. Weinfurter, R. Werner, and A. Zeilinger. *Quantum Information*. Springer-Verlag, Berlin, 2001.

[AE75] L. Allen and J. H. Eberly. *Optical Resonance and Two Level Atoms*. Wiley, New York, 1975.

[BBM03] L. Besombes, J. J. Baumberg, and J. Motohisa. Coherent spectroscopy of optically gated charged single InGaAs quantum dots. *Phys. Rev. Lett.*, 90(25):257402, 2003.

[Beh03] E. Beham. *Photostromspektroskopie an einzelnen Quantenpunkten*. Dissertation, TU München, 2003.

[BEZ00] D. Bouwmeester, A. Ekert, and A. Zeilinger. *The Physics of Quantum Information*. Springer-Verlag, Berlin, 2000.

[BKF+99] M. Bayer, A. Kuther, A. Forchel, A. Gorbunov, V. B. Timofeev, F. Schafer, J. P. Reithmaier, T. L. Reinecke, and S. N. Walck. Electron and hole g factors and exchange interaction from studies of the exciton fine structure in $In_{0.60}Ga_{0.40}As$ quantum dots. *Phys. Rev. Lett.*, 82(8):1748–1751, 1999.

[BLH01] D. Birkedal, K. Leosson, and J. M. Hvam. Long lived coherence in self-assembled quantum dots. *Phys. Rev. Lett.*, 87(22):227401, 2001.

[BLS+01] P. Borri, W. Langbein, S. Schneider, U. Woggon, R. L. Sellin, D. Ouyang, and D. Bimberg. Ultralong dephasing time in InGaAs quantum dots. *Phys. Rev. Lett.*, 87(15):157401, 2001.

[BLS+02] P. Borri, W. Langbein, S. Schneider, U. Woggon, R. L. Sellin, D. Ouyang, and D. Bimberg. Rabi oscillations in the excitonic ground-state transition of InGaAs quantum dots. *Phys. Rev. B*, 66(8):081306, 2002.

[BOS+02] M. Bayer, G. Ortner, O. Stern, A. Kuther, A. A. Gorbunov, A. Forchel, P. Hawrylak, S. Fafard, K. Hinzer, T. L. Reinecke, S. N. Walck, J. P. Reithmaier, F. Klopf, and F. Schäfer. Fine structure of neutral and charged excitons in self-assembled in(ga)as/(al)gaas quantum dots. *Phys. Rev. B*, 65(19):195315, May 2002.

[BZF+01] E. Beham, A. Zrenner, F. Findeis, M. Bichler, and G. Abstreiter. Nonlinear ground-state absorption observed in a single quantum dot. *Appl. Phys. Lett.*, 79(17):2808–2810, 2001.

[DGE+98] E. Dekel, D. Gershoni, E. Ehrenfreund, D. Spektor, J. M. Garcia, and P. M. Petroff. Multiexciton spectroscopy of a single self-assembled quantum dot. *Phys. Rev. Lett.*, 80(22):4991–4994, Jun 1998.

[EC90] D. J. Eaglesham and M. Cerullo. Dislocation-free Stranski-Krastanow growth of Ge on Si(100). *Phys. Rev. Lett.*, 64(16):1943–1946, Apr 1990.

[ELdV+07a] P. Ester, L. Lackmann, S. Michaelis de Vasconcellos, M. C. Hubner, A. Zrenner, and M. Bichler. p-shell rabi-flopping and single photon emission in an InGaAs/GaAs quantum dot. *Physica E: Low-dimensional Systems and Nanostructures*, In Press, Corrected Proof, 2007.

[ELdV+07b] P. Ester, L. Lackmann, S. Michaelis de Vasconcellos, M. C. Hubner, A. Zrenner, and M. Bichler. Single photon emission based on coherent state preparation. *Applied Physics Letters*, 91(11):111110, 2007.

[ESdV+06a] Patrick Ester, Stefan Stufler, Steffen Michaelis de Vasconcellos, Max Bichler, and Artur Zrenner. High resolution photocurrent-spectroscopy of a single quantum dot. *physica status solidi (c)*, 3:3722–3725, 2006.

[ESdV+06b] Patrick Ester, Stefan Stufler, Steffen Michaelis de Vasconcellos, Max Bichler, and Artur Zrenner. Ramsey fringes in a single InGaAs/GaAs quantum dot. *physica status solidi (b)*, 243 (10):2229, 2006.

[Fin01] F. Findeis. *Optical Spectroscopy on Single Self-assembled Quantum Dots*. Dissertation, TU München, 2001.

[FWDK03] J. Forstner, C. Weber, J. Danckwerts, and A. Knorr. Phonon-assisted damping of Rabi oscillations in semiconductor quantum dots. *Phys. Rev. Lett.*, 91(12):127401, 2003.

[FZBA00] F. Findeis, A. Zrenner, G. Bohm, and G. Abstreiter. Phonon-assisted biexciton generation in a single quantum dot. *Physical Review B*, 61(16):R10579–R10582, 2000.

[HSK+04] A. Hogele, S. Seidl, M. Kroner, K. Karrai, R. J. Warburton, B. D. Gerardot, and P. M. Petroff. Voltage-controlled optics of a quantum dot. *Phys. Rev. Lett.*, 93(21):217401, 2004.

[HTK+02a] H. Htoon, T. Takagahara, D. Kulik, O. Baklenov, A. L. Holmes, Jr., and C. K. Shih. Interplay of Rabi oscillations and quantum interference in semiconductor quantum dots. *Phys. Rev. Lett.*, 88(8):087401, 2002.

[HTK+02b] H. Htoon, T. Takagahara, D. Kulik, O. Baklenov, A. L. Holmes, and C. K. Shih. Interplay of rabi oscillations and quantum interference in semiconductor quantum dots. *Phys. Rev. Lett.*, 88(8):087401, Feb 2002.

[HvBV+05] R. Hanson, L. H. Willems van Beveren, I. T. Vink, J. M. Elzerman, W. J. M. Naber, F. H. L. Koppens, L. P. Kouwenhoven, and L. M. K. Vandersypen.

Single-shot readout of electron spin states in a quantum dot using spin-dependent tunnel rates. *Phys. Rev. Lett.*, 94(19):196802, 2005.

[HVL+97] R. Heitz, M. Veit, N. N. Ledentsov, A. Hoffmann, D. Bimberg, V. M. Ustinov, P. S. Kop'ev, and Zh. I. Alferov. Energy relaxation by multiphonon processes in inas/gaas quantum dots. *Phys. Rev. B*, 56(16):10435–10445, Oct 1997.

[JHW98] L. Jacak, P. Hawrylak, and A. Wojs. *Quantum Dots*. Springer Verlag, 1998.

[KGT+01] H. Kamada, H. Gotoh, J. Temmyo, T. Takagahara, and H. Ando. Exciton Rabi oscillation in a single quantum dot. *Phys. Rev. Lett.*, 87(24):246401, 2001.

[KLG+94] N. Kirstaedter, N.N. Ledentsov, M. Grundmann, D. Bimberg, V.M. Ustinov, S.S. Ruvimov, M.V. Maximov, P.S. Kop'ev, Zh.I. Alferov, U. Richter, P. Werner, U. Gösele, and J. Heydenreich. Low threshold, large T_0 injection laser emission from (InGa)As quantum dots. *Electronics Letters*, 30(17):1416–1417, 1994.

[KRS05] S. Kiravittaya, A. Rastelli, and O. G. Schmidt. Self-assembled InAs quantum dots on patterned GaAs(001) substrates: Formation and shape evolution. *Applied Physics Letters*, 87(24):243112, 2005.

[KSS+05] Hubert J Krenner, Stefan Stufler, Matthias Sabathil, Emily C Clark, Patrick Ester, Max Bichler, Gerhard Abstreiter, Jonathan J Finley, and Artur Zrenner. Recent advances in exciton-based quantum information processing in quantum dot nanostructures. *New Journal of Physics*, 7:184, 2005.

[KZMW01] C. Kurtsiefer, P. Zarda, S. Mayer, and H. Weinfurter. The breakdown flash of silicon avalanche photodiodes–back door for eavesdropper attacks? *Journal of Modern Optics*, 48:2039–2047(9), 2001.

[LLU+00] J.A. Lott, N.N. Ledentsov, V.M. Ustinov, N.A. Maleev, A.E. Zhukov, A.R. Kovsh, M.V. Maximov, B.V. Volovik, Zh.I. Alferov, and D. Bimberg. InAs-InGaAs quantum dot VCSELs on GaAs substrates emitting at 1.3 μm. *Electronics Letters*, 36(16):1384–1385, 2000.

[Lun03] Mark Lundstrom. APPLIED PHYSICS: Enhanced: Moore's Law Forever? *Science*, 299(5604):210–211, 2003.

[MJ04] P. Machnikowski and L. Jacak. Resonant nature of phonon-induced damping of Rabi oscillations in quantum dots. *Phys. Rev. B*, 69(19):193302, 2004.

[MKB+00] P. Michler, A. Kiraz, C. Becher, W. V. Schoenfeld, P. M. Petroff, Lidong Zhang, E. Hu, and A. Imamoglu. A Quantum Dot Single-Photon Turnstile Device. *Science*, 290(5500):2282–2285, 2000.

[MRM+07] M. Mehta, D. Reuter, A. Melnikov, A. D. Wieck, and A. Remhof. Focused ion beam implantation induced site-selective growth of InAs quantum dots. *Applied Physics Letters*, 91(12):123108, 2007.

[MS91] P. Meystre and M. Sargent. *Elements of Quantum Optics*. Springer-Verlag, Berlin, 2 edition, 1991.

[MWB+04] A. Muller, Q. Q. Wang, P. Bianucci, C. K. Shih, and Q. K. Xue. Determination of anisotropic dipole moments in self-assembled quantum dots using Rabi oscillations. *Appl. Phys. Lett.*, 84(6):981–983, 2004.

[OAM99] Kazunori Oshiro, Koji Akai, and Mitsuru Matsuura. Size dependence of polaronic effects on an exciton in a spherical quantum dot. *Phys. Rev. B*, 59(16):10850–10855, Apr 1999.

[OAO+96] B. Ohnesorge, M. Albrecht, J. Oshinowo, A. Forchel, and Y. Arakawa. Rapid carrier relaxation in self-assembled $In_xGa_{1-x}As/GaAs$ quantum dots. *Phys. Rev. B*, 54(16):11532–11538, Oct 1996.

[PLW05] B. Patton, W. Langbein, and U. Woggon. Transient four-wave mixing of single exciton states: Exciton-exciton interaction and Rabi oscillations. *AIP Conference Proceedings*, 772(1):1232–1233, 2005.

[PY99] M. Pelton and Y. Yamamoto. Ultralow threshold laser using a single quantum dot and a microsphere cavity. *Phys. Rev. A*, 59(3):2418–2421, 1999.

[Ram90] Norman F. Ramsey. Experiments with separated oscillatory fields and hydrogen masers. *Rev. Mod. Phys.*, 62(3):541–552, 1990.

[SEZ06] Stefan Stufler, Patrick Ester, and Artur Zrenner. Ramsey fringes in an electric-field-tunable quantum dot system. *Phys. Rev. Lett.*, 96:037402, 2006.

[SEZB04] S. Stufler, P. Ester, A. Zrenner, and M. Bichler. Power broadening of the exciton linewidth in a single InGaAs/GaAs quantum dot. *Appl. Phys. Lett.*, 85(18):4202–4204, 2004.

[SEZB05] S. Stufler, P. Ester, A. Zrenner, and M. Bichler. Quantum optical properties of a single $In_xGa_{1-x}As$-GaAs quantum dot two-level system. *Physical Review B*, 72(12):121301, 2005.

[SGB99] O. Stier, M. Grundmann, and D. Bimberg. Electronic and optical properties of strained quantum dots modeled by 8-band k·p theory. *Phys. Rev. B*, 59(8):5688–5701, Feb 1999.

[SK] I. N. Stranski and L. Krastanow. Zur Theorie der orientierten Ausscheidung von Ionenkristallen aufeinander. Sitzungsberichte der Akademie der Wissenschaften in Wien, Mathematisch-naturwissenschaftliche Klasse Abteilung IIb 146 (1-10), 797 (1937).

[SLG+02] T. H. Stievater, Xiaoqin Li, J. R. Guest, D. G. Steel, D. Gammon, D. S. Katzer, and D. Park. Wavelength modulation spectroscopy of single quantum dots. *Appl. Phys. Lett.*, 80(11):1876–1878, 2002.

[SLS+01a] T. H. Stievater, Xiaoqin Li, D. G. Steel, D. Gammon, D. S. Katzer, D. Park, C. Piermarocchi, and L. J. Sham. Rabi oscillations of excitons in single quantum dots. *Phys. Rev. Lett.*, 87(13):133603, 2001.

[SLS+01b] T. H. Stievater, Xiaoqin Li, D. G. Steel, D. Gammon, D. S. Katzer, D. Park, C. Piermarocchi, and L. J. Sham. Rabi oscillations of excitons in single quantum dots. *Phys. Rev. Lett.*, 87(13):133603, Sep 2001.

[SME+06] S. Stufler, P. Machnikowski, P. Ester, M. Bichler, V. M. Axt, T. Kuhn, and A. Zrenner. Two-photon Rabi oscillations in a single $In_xGa_{1-x}As/GaAs$ quantum dot. *Physical Review B*, 73(12):125304, 2006.

[TMT+85] K. Takeda, N. Matsumoto, A. Taguchi, H. Taki, E. Ohta, and M. Sakata. *Phys. Rev. B*, 32:1101, 1985.

[TWM+97] E.V. Tsiper, P.D. Wang, J.L. Merz, A.L. Efros, S. Fafard, D. Leonard, and P.M. Petroff. Anomalous magnetophotoluminescence as a result of level repulsion in arrays of quantum dots. *Solid State Communication*, 104:391–395, 1997.

[UML+05] T. Unold, K. Mueller, C. Lienau, T. Elsaesser, and A. D. Wieck. Optical control of excitons in a pair of quantum dots coupled by the dipole-dipole interaction. *Phys. Rev. Lett.*, 94(13):137404, 2005.

[VAK03] A. Vagov, V. M. Axt, and T. Kuhn. Impact of pure dephasing on the nonlinear optical response of single quantum dots and dot ensembles. *Phys. Rev. B*, 67(11):115338, 2003.

[VBUG05] J. M. Villas-Boas, Sergio E. Ulloa, and A. O. Govorov. Decoherence of Rabi oscillations in a single quantum dot. *Phys. Rev. Lett.*, 94(5):057404, 2005.

[VFSB01] A. Vasanelli, R. Ferreira, H. Sakaki, and G. Bastard. *Solid State Commun*, 118:459, 2001.

[VSB+01] L. M. K. Vandersypen, M. Steffen, G. Breyta, C. S. Yannoni, M. H. Sherwood, and I. L. Chuang. Experimental realization of Shor's quantum factoring algorithm using nuclear magnetic resonance. *Nature*, 414:883, 2001.

[WHFJ96] Arkadiusz Wojs, Pawel Hawrylak, Simon Fafard, and Lucjan Jacak. Electronic structure and magneto-optics of self-assembled quantum dots. *Phys. Rev. B*, 54(8):5604–5608, Aug 1996.

[WMB+05] Q. Q. Wang, A. Muller, P. Bianucci, E. Rossi, Q. K. Xue, T. Takagahara, C. Piermarocchi, A. H. MacDonald, and C. K. Shih. Decoherence processes during optical manipulation of excitonic qubits in semiconductor quantum dots. *Phys. Rev. B*, 72(3):035306, 2005.

[Wog97] U. Woggon. *Optical properties of semiconductor quantum dots*. Springer-Verlag, Berlin, 1997.

[ZBJ+01] Valery Zwiller, Hans Blom, Per Jonsson, Nikolay Panev, Soren Jeppesen, Tedros Tsegaye, Edgard Goobar, Mats-Erik Pistol, Lars Samuelson, and Gunnar Bjork. Single quantum dots emit single photons at a time: Antibunching experiments. *Applied Physics Letters*, 78(17):2476–2478, 2001.

[ZBS+02] A. Zrenner, E. Beham, S. Stufler, F. Findeis, M. Bichler, and G. Abstreiter. Coherent properties of a two-level system based on a quantum-dot photodiode. *Nature*, 418:612, 2002.

[ZSE+06] Artur Zrenner, Stefan Stufler, Patrick Ester, Steffen Michaelis de Vasconcellos, Marc C. Hübner, and Max Bichler. Recent developments in single dot coherent devices. *physica status solidi (b)*, 243 (14):3696 – 3708, 2006.

[ZSP+05] Bingyang Zhang, Glenn S. Solomon, Matthew Pelton, Jocelyn Plant, Charles Santori, Jelena Vučković, and Yoshihisa Yamamoto. Fabrication of InAs quantum dots in AlAs/GaAs DBR pillar microcavities for single photon sources. *Journal of Applied Physics*, 97(7):073507, 2005.

List of publications

- S. Stufler, P. Ester, A. Zrenner, and M. Bichler
Power broadening of the exciton linewidth in a single InGaAs/GaAs quantum dot
Appl. Phys. Lett. **85**, 4202-4204 (2004)

- S. Stufler, P. Ester, A. Zrenner, and M. Bichler
Quantum optical properties of a single $In_xGa_{1-x}As - GaAs$ quantum dot two-level system
Phys. Rev. B **72**, 121301(R) (2005)

- A. Zrenner, S. Stufler, P. Ester, and M. Bichler
Manipulations of a qubit in a semiconductor quantum dot
Advances in Solid State Physics **45**, 73-184 (2005)

- H. J. Krenner, S. Stufler, M. Sabathil, E. C. Clark, P. Ester, M. Bichler, G. Abstreiter, J. J. Finley, and A. Zrenner
Recent advances in exciton-based quantum information processing in quantum dot nanostructures
New Journal of Physics **7**, 184 (2005)

- S. Stufler, P. Ester, A. Zrenner, and M. Bichler
Ramsey fringes in an electric-field-tunable quantum dot system
Phys. Rev. Lett. **96**, 037402 (2006)

- S. Stufler, P. Machnikowski, P. Ester, M. Bichler, V. M. Axt, T. Kuhn, and A. Zrenner
Two-photon Rabi oscillations in a single InGaAs/GaAs quantum dot
Phys. Rev. B **73**, 125304 (2006)

- P. Ester, S. Stufler, S. M. de Vasconcellos, M. Bichler, and A. Zrenner
Ramsey fringes in a single InGaAs/GaAs quantum dot
physica status solidi (b) Vol. **243**, Issue 10, p. 2229

- A. Zrenner, S. Stufler, P. Ester, S. Michaelis de Vasconcellos, M. Hübner, and M.Bichler
Recent developments in single dot coherent devices
physica status solidi (b) Vol. **243**, Issue 14, p. 3696

- S. Michaelis de Vasconcellos, S. Stufler, S.-A. Wegner, P. Ester, A. Zrenner, and M. Bichler
  Quantum interferences of a single quantum dot in the case of detuning
  Phys. Rev. B **74**, 081304 (2006)

- A. Zrenner, S. Stufler, P. Ester, and M. Bichler
  Coherent properties of quantum dot two-level systems
  ISRAEL JOURNAL OF CHEMISTRY, Volume **46**, Issue: 4, p. 349-356 (2006)

- P. Ester, S. Stufler, S. Michaelis de Vasconcellos, M. Bichler, and A. Zrenner
  High resolution photocurrent-spectroscopy of a single quantum dot
  physica status solidi (c) Vol **3**, Issue 11, p. 3722 (2006)

- S. Michaelis de Vasconcellos, S. Stufler, S.-A. Wegner, P. Ester, M. Bichler and A. Zrenner
  Quantum interferences of a single quantum dot in the case of detuning
  physica status solidi (c) Vol. **3**, Issue 11, p. 3730 (2006)

- P. Ester, L. Lackmann, S. Michaelis de Vasconcellos, M. C. Hübner, A. Zrenner, and M. Bichler
  Single photon emission based on coherent state preparation
  Appl. Phys. Lett. **91**, 111110 (2007)

- P. Ester, L. Lackmann, M.C. Hübner, S. Michaelis de Vasconcellos, A. Zrenner and M. Bichler
  p-shell Rabi-flopping and single photon emission in an InGaAs/GaAs quantum dot
  Physica E: Low-dimensional Systems and Nanostructures, Volume **40**, Issue 6, April 2008, Pages 2004-2006

Danksagung

Abschließend möchte ich mich bei allen bedanken, die zum Gelingen dieser Doktorarbeit beigetragen haben. Mein besonderer Dank gilt:

- ARTUR ZRENNER, der mir die Möglichkeit gegeben hat, an diesem interessanten und innovativem Thema meine Dissertation durchzuführen. Ohne diese fachliche und technologische Hilfestellung wäre diese Arbeit nicht möglich gewesen.
- Der gesamten Arbeitsgruppe *nanostructure optoelectronics*. Allen voran den beiden Quanten-Punkt-Doktoranden MARC C. HÜBNER und STEFFEN J. MICHAELIS DE VASCONCELLOS für die super Zusammenarbeit, CHRISTIAN PASSLICK, GERHARD BERTH, HEIKE DEGLER, LYDIA LACKMAN, REINER SCHNEIDER, WOLF-RÜDIGER SCHULTE, THOMAS HANGLEITER und allen ehemaligen Mitgliedern der Arbeitsgruppe für eine wirklich angenehme Atmosphäre.
- Der Prüfungskommission: Prof. Dr. TORSTEN MEIER für die Übernahme des Komissionsvorsitz, Prof. Dr. KLAUS LISCHKA und Prof. Dr. ARTUR ZRENNER für die Übernahme der Gutachtertätigkeiten, und Dr. CHRISTOF HOENTZSCH als Vertreter des Mittelbaus.
- Dem gesamten Department Physik, insbesondere den Arbeitsgruppen LISCHKA, MEIER und FÖRSTNER für den wissenschaftlichen Austausch, sowie der mechanischen Werkstatt für die schnelle Umsetzung meiner Projekte.
- JOHANNES PAULI, unserem schnellen Tieftemperatur-Dealer der immer Zeit hatte für ein kaltes Kännchen.
- Ganz besonderer Dank gilt meiner Freundin JOHANNA, die mich und meine Arbeit fantastisch unterstützt hat. Du bist super!
- Meinen Eltern, die mich in meinen Entscheidungen immer gefördert haben.
- Meinen Freunden: ANDI, ANSGAR, BASTIAN, BERND, BURKHARD, CAROLINE, CHRISTIAN, DAVID, DORITH, FRAUKE, GUNNAR, JENS, JÖRG, JULIA, MARC, NICKI, SARAH, SABINE, SEBASTIAN, STEFAN, THOMAS, ...
- und allen die in dieser Liste ausversehen vergessen wurden. Danke!